Title
High-throughput molecular binding analysis on open-microfluidic platform

Author
Pan, Yuchen

Publication Date
2016

Peer reviewed|Thesis/dissertation

High-throughput molecular binding analysis on open-microfluidic platform

By

Yuchen Pan

A dissertation submitted in partial satisfaction of the

requirements for the degree of

Joint Doctor of Philosophy

with University of California, San Francisco

in

Bioengineering

in the

Graduate Division

of the

University of California, Berkeley

Committee in charge:

Professor Amy Herr, Chair
Professor Bo Huang
Professor Ming Wu

Spring 2016

High-throughput molecular binding analysis on open-microfluidic platform

Abstract

High-throughput molecular binding analysis on open-microfluidic platform

by

Yuchen Pan

Joint Doctor of Philosophy
with University of California, San Francisco, in Bioengineering

University of California, Berkeley

Professor Amy Herr, Chair

Biomolecular binding interactions underpin life sciences tools that are essential to fields as diverse as molecular biology and clinical chemistry. Merging needs in life science research entail fast, robust and quantitative binding reaction characterization, such as antibody selection, gene regulation screening and drug screening. Identification, characterization, and optimization of these diverse molecular binding reactions demands the availability of powerful, quantitative analytical tools.

Among modern analysis tools well-suited to such characterizations are the techniques of electrophoresis. Electrophoretic separations physically separate molecules based on electrophoretic mobility differences among species, with mobility differences functions of molecular size, charge, and conformation. All three characteristics can depend on binding state.

Electrophoretic mobility shift assays (EMSAs) are one type of electrophoretic separations that detect binding-induced mobility changes of target analytes. In EMSAs, a probing molecule reacts with a target analyte and the binding interaction induces a change in the physicochemical properties of the target that then results in a detectable mobility shift.

EMSAs benefit from microfluidic adaption. The use of high separating electric field and miniaturized formats greatly enhance assay throughput and reduce sample consumption. Further, the precision of microfluidic control of transport and reaction confers a level of quantitation and reproducibility that are difficult (if not impossible) to achieve with conventional tools.

Our group has previously introduced a microfluidic EMSA (μMSA) assay that reduces reagent consumption ten-fold and processing time a hundred-fold. While a notable advance,

microchip based EMSAs suffer from equipment-heavy infrastructure needs and serial electrophoresis implementations, limiting throughput and scale-up potential.

To surmount these limitations of microfluidic EMSAs, our group has pioneered "open-microfluidic" electrophoresis arrays that support >384 concurrent polyacrylamide gel electrophoresis (PAGE) separations. The PAGE molecular sieving gels are photo-patterned directly on a planar substrate – not inside of enclosed microfluidic channels. The adaption of EMSAs to such a PAGE gel array format reduces infrastructure demands and affords parallel operation, thereby overcoming the shortcomings of in-channel glass devices.

Here we report on the design, development, characterization, optimization, and application of free-standing polyacrylamide gel (*fs*PAG) EMSAs to answer questions about molecular binding fundamental to molecular biology research and the biotechnology industry. We harness the open, multiplexed nature of the *fs*PAG format, the quantitative precision of fine fluidic control and the small sample volume requirements to yield two sets of analytical contributions.

The first set of contributions centers on discerning both form and function during RNA riboswitch binding to metabolites. Not only does the RNA riboswitch bind to certain metabolites, the molecule takes on a compact conformation if that binding event is functional. This compact conformation results in an electrophoretic mobility shift versus the non-function RNA riboswitch. We first developed a microchip based rapid *in-vitro* cyclic-di-GMP biosensor. This assay builds on the previously reported riboswitch μMSA technology and enables fast (30 min) cyclic-di-GMP concentration determination in cell extracts with high detection sensitivity. Our work is the only "minimalist cyclic-di-GMP biosensor" reported so far, which performs direct concentration measurements with no need for complex riboswitch derivative construction.

We then characterized *fs*PAG EMSAs for riboswitch binding analysis. We detailed the fundamental physical properties of the open microfluidic gel array and utilized the analytical tool for HTP riboswitch binding analysis. *fs*PAG EMSAs offer a throughput (10 data/min) that is 30 times higher than our own previously reported μMSA and 1000 higher than the canonical slab-gel EMSAs.

In a second set of contributions, we applied the precision quantitation capability of fsPAG EMSAs to report binding kinetics of fragment antigen-binding antibody reagents. We integrated the open-microfluidic fsPAG with an acoustic sample delivery system and developed a novel automated binding affinity measurement tool for fragment antigen-binding fragment (Fab) molecules. To date, the assay offers the highest reported throughput. Important to such throughput and to reproducibility, the assay eliminates the cumbersome manual sample loading previously involved in performing fsPAGE and greatly improves the electrophoretic uniformity of the assay. The equilibrium constants of 6 Fab were simultaneously measured on a 384-plex *fs*PAG device.

In a more speculative and forward-looking contribution, we designed and prototyped an *fs*PAG western blot assay; a departure from in-channel design strategies our laboratory has pursued in the past. A critical contribution of the protype assay is sample stacking during transfer from the PAGE separation to the blotting step; with the stacking enhancing the detection sensitivity and reduceing the assay time. The *fs*PAG western blot benefits from using the molecular binding interactions we have characterized earlier, but now in open-microfluidic format.

Taken together, we have designed, developed, and applied high-throughput molecular binding analysis platforms with open-microfluidic polyacrylamide gel electrophoresis tools to both detection of functional riboswitch binding events and quantitative characterization of antibody fragment binding kinetics. Fundamental and design findings offer new understanding and capabilities in parallelized binding reaction analyses and affinity based molecular screening, fulfilling two sets of unmet needs in bioanalytical technology.

To my family

Table of Contents

List of Figures and Tables

Acknowledgements

As a survivor of the competitive Chinese education system, I had long established a different view of science than many of my American peers. To me, science seemed more like a pass to the next level of education. I had gone through many insanely difficult math/physics/chemistry tests just to get into the top schools and gradually science simply became round after round of problem set. I came to Berkeley with this view of science. Five years later, I am leaving with more. I learnt the creation of science, not just using it. I tried to solve problems I discovered on my own, rather than predefined by someone else. I deeply enjoyed the process of taking all these wonderful and exciting technologies of medicine and biology into a new level. I greatly benefited from discussion with a collection of the best brains in the world. I felt honored for my contribution to the lab and the science community. Now, I am moving into the business world, but I believe these precious knowledge and experience I gained on Cal campus will be identically influential. Thank you to everyone who has helped to make that possible.

First, I would like to thank my Ph.D. advisor, Amy Herr, for the great mentorship during my study here. Thank you for taking me to the Herr lab and it is an unforgettable and impressing experience of my life. Amy spent huge amount of time and personalize the mentorship for every one of us to ensure we achieved the maximum growth and accomplished the most. The "tiring" weekly notes kept track of our progression and the detailed comments pointed out the right direction. Amy is also a great listener and she would make sure everyone is pursuing their own interests and all the work I did in lab came out of our discussion. Besides research work, her personal commitment to excellence and tireless efforts for improvements set the role model for all of us. Thank you, Amy, for your time, your support, your mentorship and all those that have made my working here exciting!

Second, I would like to give my thanks to the helpful and cheerful Herr lab members. I can't remember how many times your inspiration lit up my thoughts after weeks' of torturing failure. Without these detailed help and meaningful discussion, I wouldn't get any closer to graduation. Special thanks to Todd Duncombe, who has been kindly giving help on my projects from the first day I joined the lab till the last day you worked for group. We worked closely on projects and published together. Without your pioneering work in free-standing gel, my Ph.D. projects would never ever exist. Joint ventures were also taken with Kelly Karns and Monica Kapil. I would also like to thank our collaborators outside the Herr lab for providing materials and teaching expertise: Jade Sales-Lee, Colleen Kellenberger, Yu-Fang Angela Hsieh, Scott Hickey, Michael Hornsby and Karolina Wypisniak.

During the summer of my 4th year I was fortunate to have the opportunity to intern with Labcyte Inc. I would like to thank Amy for putting me in contact and special thanks to Eric Sackmann for providing the great mentorship and support for research collaboration. An industrial practice along with the academic training in biotechnology has made my doctoral study more than solid and comprehensive.

Thank you to my thesis committee, Prof. Ming Wu and Prof. Bo Huang, for taking an active interest in my success. Thank you to Kristin Olson and Rebecca Pauling and all the staff members in Bioengineering department for helping me solve my problems along the way towards getting my Ph.D. Thank you to my graduate research fellowship, the Kang Family Graduate Fellowship for Biotechnology.

Lastly, I would like to thank my parents for your consistent support through my life, both spiritually and financially. No matter where I am, you stand with me. No matter what direction I take, you kept encouraging me. The Pan family has always been a bottomless source of happiness and strength to my life.

Chapter 1: Introduction

1.1 Motivation for high-throughput molecular binding assays

Molecular binding interactions are ubiquitous in virtually all biological processes. Binding between molecules mediates the metabolism in every living organism and is, in short, the force that holds the world together. In a molecular binding event, two proximal molecules become stably associated owing to attractive interaction between the species. Molecular binding can be categorized into three types[1]: non-covalent, reversible-covalent and irreversible-covalent. Non-covalent binding is the most common type of reaction and the bound molecules are called a "molecular complex".[2]

Proteins are a class of biomolecules widely involved in intramolecular binding interactions. Proteins are composed of combinations of any of the 20 amino acids and most proteins fold into unique 3-dimensional structures that encode a vast array of functions in living organism. Proteins bind to a variety of molecular targets, including other proteins, small molecule ligands and nucleic acids (DNA, RNA).[3] Although proteins are composed of the same basic set of amino acids, the myriad array of different amino acid sequences and structures exhibit and serve a diversity of functions, such as enzymes, collagen, hormones, antibodies, lectin and transporters.

In particular, an antibody molecule is a type of defensive protein used by the immune system to identify and neutralize an invading pathogen or virus. Antibodies interact with a cognate antigen through the spatial complementarity of the antibody and antigen, in which the paratope on each tip of the antibody "Y" 3D structure specifically pairs with one epitope on the cognate antigen, thus allowing the two biomolecules to bind selectively. In contemporary life sciences and clinical medicine, antibodies are widely used in research laboratories, clinical diagnostics and pharmaceutical industries. However, due to the differences in the production process, we observe great variation in performance and quality of binding for commercially available antibodies. Consequently, a unified standard for antibody selection and subsequent validation assay would be a tremendous resource.[4] Generally, the binding affinity between antibody and antigen is quantified by three parameters:

1. The association kinetic rate, k_{on},
2. The disassociation kinetic rate, k_{off}, and
3. The dissociation constant K_D.

The K_D of an interaction quantitatively describes the relationship of each component concentration at equilibrium state. The K_D value equals the ratio of dissociation (unbinding) rate and association (binding) rate constants ($K_D = k_{off}/k_{on}$) for a specific antibody-antigen pair.

Current approaches for antibody screening/selection include enzyme-linked immunosorbent assays (ELISAs) and western blotting (WB). These decades' old technologies have been widely used in research and clinical settings. However, these approaches generally involve slow processing time and large sample consumption. ELISA, in particular, utilizes a surface-based heterogeneous format which requires sample immobilization on substrate prior to measurement, making the ELISA prone to artefactual binding affinity measurements, as the physical immobilization of one binding partner likely alters the reactivity of the interaction. In addition, both canonical ELISAs and WBs are not amenable to scale-up, making these assays unsuitable for high-throughput antibody selection and validation tests.

Beyond proteins, DNA and RNA molecules also participate in a wide variety of binding interactions.[5] Intramolecular interactions in nucleic acids are typically defined by Waston-Crick base pairing which imparts unique 3-dimenstional structures and function to the molecules. DNA and RNA also bind to proteins. Certain proteins bear DNA-binding domains, an independently folded protein domain that recognizes a specific sequence of single- or double-stranded DNA. Such DNA-protein bindings exhibit a variety of biological rules. For example, transcription factor binds to DNA regulates gene expression. Restriction enzymes bind to specific parts of the protein and modify the structure. Beyond DNA, RNA also binds to a range of molecules, including proteins, DNA and other small molecule metabolites in cells.

Of direct relevance to this dissertation research is a regulatory segment located on the messenger RNA that is called a "riboswitch". The riboswitch binds to small molecules in the cytosol and changes the expression of protein. Riboswitches are mostly found in bacterial cells and many evidence suggested that some riboswitches might represent ancient regulatory systems.[6] Because of direct impact on genetic regulation, riboswitches have found potential biotechnological applications and numerous research involving the species has emerged over the past 10 years. Current research on riboswitches centers round the following topics:

1. Computationally and experimentally identify new riboswitch candidates and ligand binders.[6]
2. Quantitative characterization of the riboswitch binding reactions.[7]
3. Practical biotech applications such as antibiotic drug screening[8] and gene therapy. [9]

Standard approaches that are currently in use for study of riboswitch binding reaction include in-line probing[10], Förster resonance energy transfer (FRET)[11], fluorescence polarization (FP)[12] and isothermal calorimetry[13]. These technologies are similar to antibody binding assays and, though effective, are generally low-throughput (see Chapter 2 for details)

Therefore, high-throughput tools for protein/nucleic acids binding assays are in need. Polyacrylamide gel electrophoresis (PAGE), traditionally used for protein fractionation[14], is based on a nano-porous sieving hydrogel that impedes proteins on the basis of their size and structure. The good separation power of PAGE could rapidly fractionate the bound and

unbound affinity reagents to reveal the concentrations of each components and therefore accelerate the quantitative characterization of the binding reaction, for example the fast fragment antigen-binding fragment (Fab) K_D measurements through the fully automated PAGE arrays (Chapter 5). Additionally, PAGE also enables structure/size differentiation for nucleic acids oligomers, such as riboswitches and aptamers, so that the binding reactions can also be analyzed on gel (Chapter 2). Overall, with adaption onto microfluidic array formats, conventional binding assays may benefit from a modernized PAGE for high-throughput analysis, enabling new types of measurements for molecular binding reactions there were not previously possible.

1.2 Electrophoretic assay for molecular binding study

So far, molecular binding studies have been done on various types of electrophoretic assays, including the standard slab-gel PAGE[15], capillary electrophoresis (CE)[16], isoelectric focusing (IEF)[17] and microchip platform[18]. Generally, upon interacting with their ligands, the binding molecules would typically experience change in size, charge, conformation and isoelectric point, making them physically distinguishable from their original form. With electrophoretic force, the bound and unbound population can be fractionated and quantified to reveal information of the binding reactions. Therefore, careful choosing the appropriate electrophoretic format and optimizing the experimental parameters would facilitate components separation and therefore the binding analysis. This section provides a brief introduction to the fundamental knowledge of electrophoresis[19,20], important aspects for consideration in optimization of separation performance and the benefits for microfluidic electrophoretic assay. This section also surveys existing microfluidic binding assay, with a particular focus on electrophoretic mobility shift assays (EMSAs). More details can be found in the cited resources.

1.2.1 Electrophoretic transport

A charged particle moving in electrophoresis typically experiences two main forces, the electrostatic force, or more precise here as electrophoretic force, and diffusion. Particularly, we use the term convection to describe particle moving along electrophoresis. In electrophoresis, the migrant's velocity is determined from the balance between the electrophoretic force and fluid drag force. For a small particle, we can assume the electrophoretic force $F_{EP}=qE$, where q and E are the charge of the particle and the strength of the applied electric field. Concurrently, the particle is subject to stokes drag force $F_{DRAG}=6\pi a\eta U$. Here, a is the hydrodynamic radius of the biomolecule, η is the viscosity of the medium and U is the velocity of the molecule. Balancing F_{EP} and F_{DRAG}, we will get the following equation:

$$U = \frac{qE}{6\pi a\eta} \tag{1}$$

Using the definition of electrophoretic mobility $\mu = U/E$, equation 1 can be further derived to reveal the relationship between electrophoretic mobility and the physical property of the particle.

$$\mu_{EP} = \frac{q}{6\pi a\eta} \tag{2}$$

Equation 2 reveals the dependence of electrophoretic mobility of a particle on its charge and size. Equation 2 serves the basis for all electrophoretic analysis, stating particles can be separated based on radius, size, charge or the combination of these.

In fact, the real electrophoretic mobility of a particle in solution is dictated by the interaction between the surface charge density and ion concentration in the surrounding solution, or more specifically, the formation of electric double layer (EDL) around the particle.[21] Particularly, for small particle whose radius a is much greater than thickness of EDL λ_D, $\mu_{EP} = \varepsilon\varphi/\eta$, where ε and φ are the permittivity of the medium and interfacial potential. However, these parameters are generally hard to determine in practical case and thus an oversimplification in equation 2 is used.

Another driving force for particle motion is diffusion that moves particle down the gradient and is dictated by Fick's law. The diffusivity of particle in the solution is determined by the balance of thermal fluctuation and stokes drag.

$$D = \frac{k_B T}{6\pi a\eta} \tag{3}$$

In equation 3, k_B and T are the Boltzmann's constant and temperature. In separation science, dispersion is a commonly used term to describe the mass distribution of the particle, and is closely related to its diffusivity. A detailed discussion of dispersion will be presented in the following section.

All together, convection and dispersion together determine the electrophoretic transport of particle in the solution. Therefore, using the generalized mass transport theory, we can describe the local concentration of particle (c) in the solution by the convection-diffusion equation:

$$\frac{\partial c}{\partial t} = D\nabla^2 c - v \cdot \nabla c \tag{4}$$

1.2.2 Separation metrics

The most important metric in electrophoretic assay is the separation resolution (SR), which depicts the degree of separation of two analytes. Assays that render high SR performance are always preferable. This section details the discussion of a couple of assay parameters and the experimental design that would affect the SR performance.

Basically, all electrophoretic assays at basic level are composed of three steps: 1) Sample loading/injection, 2) Separation and 3) Data readout and analysis. Figure 1 shows the three steps for a typical slab gel PAGE assay.

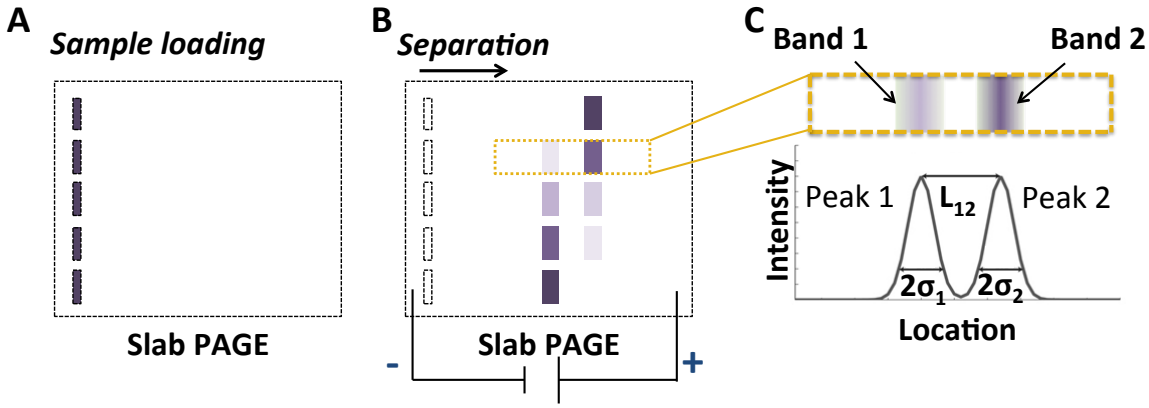

Figure 1.1 Schematic of typical PAGE operation. (A) Samples are loaded into sample well on the slab PAGE gel. (B) Slab PAGE is initiated and analytes migrate in gel according to their mobilities. (C) Analytes 1 and 2 are separated and the separation profiles were captured. Subsequent quantification of band intensity yields electropherogram from which peak distance L12 and bandwidth ($\boldsymbol{\sigma_1}$ and $\boldsymbol{\sigma_2}$) are calculated.

The sample is firstly loaded into the wells on the slab gel. At this point, the spatial distribution of sample analytes prior to electrophoresis is exclusively determined by the horizontal width of the sample well (Figure 1.1A) Mathematically, we use the term injection dispersion to quantify the variance of the horizontal distribution of particles in the well and standard deviation (σ_0) to represent the bandwith. An electric field applied across the length of the slab gel is initiated to start the separation (Figure 1.1B). Analytes move along the separation lane according to their intrinsic electrophoretic mobilities in the buffer solution and separate from each other. At time t, the peak distance L_{12} (depicted in Figure 1.1C) is calculated by $L_{12} = (\mu_2 - \mu_1)Et$. Here E is the applied electric field in slab gel PAGE. At t, the bandwidths of the analytes have grown to σ_1 and σ_2. Further σ_1 and σ_2 are given by: $\sigma_1 = \sqrt{{\sigma_0}^2 + 2D_1 t}$ and $\sigma_2 = \sqrt{{\sigma_0}^2 + 2D_2 t}$.

It bears mentioning that such treatment of σ_1 and σ_2 is an oversimplification as the equation is derived from a static diffusion model, that is, no impact from convection on the bandwidth is considered. In fact, true solution for σ_1 and σ_2 from equation 4 appears much more complicated and is usually solved with numerical simulation. However, when the contribution of convection is small relative to diffusion, such treatment gives approximately good estimation.

Therefore, the separation resolution of the two analytes is given by:

$$SR = \frac{(\mu_2 - \mu_1)Et}{2(\sigma_1 + \sigma_2)} \quad (5)$$

If we assume injection dispersion and the diffusivity are the same for both species, we can further expand equation 5 into:

$$SR = \frac{(\mu_2 - \mu_1)Et}{4\sqrt{{\sigma_0}^2 + 2Dt}} \quad (6)$$

Equation 6 indicates that SR grows with t, however, longer separation not only reduces the throughput of the assay but also decreases the peak intensity as a result of diffusion. Therefore, increasing the electrophoresis time is not an ideal approach to achieve good separation performance. Equation 6 presents three ways to improve SR with shorter time: 1) increase the electric field, 2) reduce the injection dispersion and 3) enhance the mobility difference between analytes. However, convention slab gel PAGE has limitation on the use of electric field as high field strength would increase the Joule heating that elevates the gel temperature, potentially increasing the analyte diffusivity and even melting the gel.

Over the past decade, microfluidic adaption of PAGE significant improved the assay performance. Firstly, the miniaturization of PAGE device greatly increased the surface area-to-volume ratio, consequently enhancing the heat dissipation of the PAGE, allowing higher electric field being used in the assay. Secondly, the relatively small dimension of microfluidics successfully reduced the injection dispersion and improved the separation resolution.

In separation science, two peaks are considered fully separated from each other when SR reaches 1.5, meaning only 0.3% overlaps between the two bands. Practically, we consider two bands are resolved when SR=1, at which less than 5% of the bands overlap with each other. In some cases where the differential mobilities are small, even lower SR standard can be used. However, for accuracy of quantification, SR>0.5 is recommended. [20]

1.2.3 Electrophoretic mobility shift assay

Electrophoretic mobility shift assay (EMSA) is a well-accepted technique used to study molecular interaction. It is one class of affinity-based electrophoresis assay which utilizes a molecular probe to impart size and/or charge change to the analytes. Inserting equation 2 to equation 6 we would get:

$$SR = \frac{\left(\frac{q_2}{a_2} - \frac{q_1}{a_1}\right)\frac{Et}{6\pi\eta}}{4\sqrt{{\sigma_0}^2 + 2Dt}} \quad (7)$$

Electrophoretic mobility is an intrinsic physical property of a biomolecule and it is closely related to the bio-molecular size, charge, and the viscosity of the separation medium. In

EMSAs, the molecular interaction alters the charge-to-radius ratio (q/a) of molecules and therefore induces a mobility shift detectable during electrophoretic separation. Additionally, the use of polyacrylamide gel further expands the differential mobility, improving the SR between the two populations. Figure 1.2 schematically illustrates the primary sources of affinity-based electrophoretic mobility shifts.

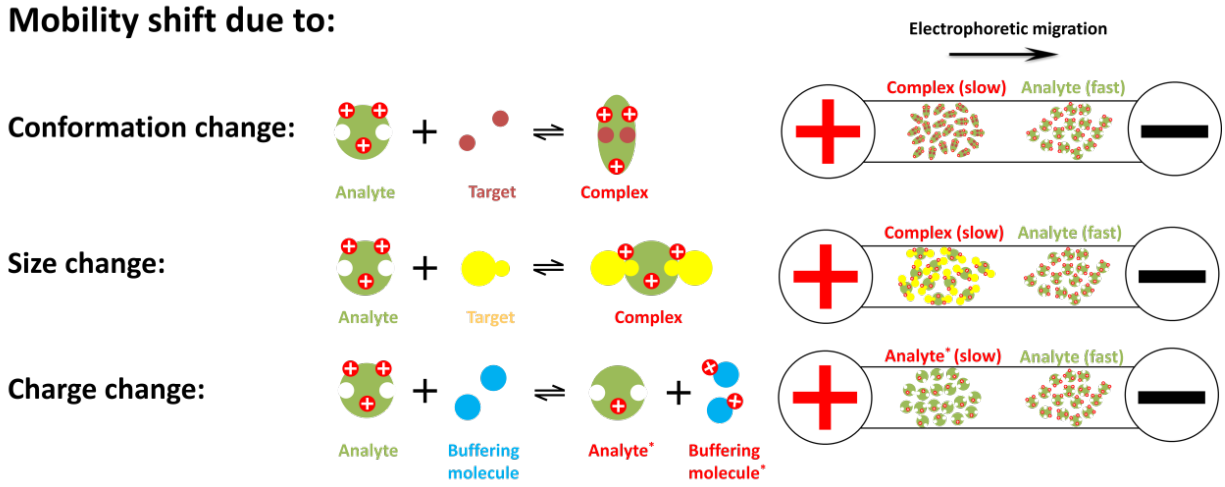

Figure 1.2 Conceptual schematic of EMSAs principle. EMSAs can arise from conformation change: Conformation of target analyte molecule changes upon complexing with probe. The resulting molecule has a different shape than the original one, yielding a shift in mobility. EMSA due to size change: Analyte interacts with the target molecule to form a complex. The complex has a distinct mobility than the free form owing to a larger molecular mass. EMSA due to charge change: A buffering molecule alters the charge on an analyte, inducing a change in its electrophoretic mobility. The increase of differential size/charge/conformation enhances the separation resolution, according to equation 7. ([27]Reprinted with permission from Electrophoresis, 35, 15, Microfluidic electrophoretic mobility shift assays for quantitative biochemical analysis)

Historically speaking, EMSAs are affinity electrophoresis technique used to study protein–DNA or protein–RNA interactions; however, gel shift assays need not be limited to the study of protein-nucleic acid interactions. Protein-peptides[22] and protein-protein[23] interactions have also been studied with the same electrokinetic principle. Herein we intend the term EMSAs to refer to all analytical assays that rely on induced mobility shifts to render different populations of species detectable by electrophoretic separations.

1.3 Microfluidic electrophoretic mobility shift assay

There are several benefits gained by moving EMSAs onto the microfluidic format. (1) The favorable scaling with miniaturization enhances heat dissipation and allows the use of much higher electric fields than conventional macro-scale formats, bringing faster separations and greater resolving power. (2) The use of polyacrylamide gel as the sieving matrix increases the

differential mobility between analytes and increases the separation resolution. Consequently, microfluidic EMSAs are ideal platforms for analyzing very small differences in bio-molecular mobility, opening the door to a myriad of biomedical applications including drug screening[24], RNA conformational analysis[7], proximal fluid diagnostics[25], and enantiomer selection[26].

Two main classes of microfluidic EMSAs are reported in literature. (1) EMSAs that utilize a small molecular probe (target) to induce a detectable change in molecular conformation. These assays shed light on the thermodynamic process of structural transformation. (2) EMSAs that utilize an affinity probe (e.g., antibody) to induce a detectable change in the size and/or charge of a target analyte. These assays provide quantitative information on the target concentration, the binding affinity (K_D), and the kinetic rate constants (k_{on} and k_{off}) of the interactions. We will briefly review existing work in each category here. A more detailed introduction of microfluidic EMSAs as well as theory can be found elsewhere[27].

Biomolecular conformation encodes important biochemical information and plays a significant role in determining biological function. Owing to the small molecular radius differences between conformational-distinct molecular populations, electrophoretic mobility differences are often difficult to detect using conventional free-solution or macro-scale electrophoretic separations. The high electric field attainable in microfluidic channels and miniaturized dimension offers better resolving power than lower field macroscale counterparts, therefore making it an ideal tool for conformation interpretation. Early studies revealed the physical correlation between conformation and electrophoretic mobility. In 2007, Craighead's group[28] experimentally analyzed the conformation-mobility relationship of stretched DNA in nano-channels. Their experiments showed that DNA mobility increased with degree of folding and it correlated the number of DNA folds to effective mobility. Later, Karns et al.,[7] demonstrated a microfluidic conformation change-based EMSA for the analysis of riboswitch aptamers. These small RNA genetic regulators undergo a conformational change when bound to their small molecule probes, often resulting in a compaction of molecular radius. The enhanced sieving power of PAG coupled with high-resolution microfluidics enabled detection of the small mobility differences between the conformationally-distinct bound and unbound riboswitch populations, which are not robustly detectable using a conventional slab gel format. This and other microfluidic EMSAs provide a quantitative platform for analysis of small conformation-based mobility shifts.

Microfluidic EMSAs found most of their use in detecting changes in analyte molecule size and/or charge[29]. Binding affinity can alter the mass and/or charge of a target analyte, thereby inducing an electrophoretic mobility shift. A broad range of biomolecules has been successfully used as affinity probes. Microfluidic affinity-based EMSAs can discriminate between bound and unbound analyte, revealing quantitative information on the analyte concentration, equilibrium dissociation constant (K_D) and kinetic rate constants (k_{on} and k_{off}).

Conventional microfluidic electrophoretic affinity assays take up heterogeneous format in which the affinity reagent is immobilized on the solid substrate, and subsequent flowing-through target sample molecules then react with the immobilized affinity target and get

captured. Quantification of the bound targets then provides more information of the binding reaction.

In contrast, microfluidic EMSAs take up homogeneous format where no sample immobilization is required (see Figure 1.2). Here, the target sample and affinity reagents are incubated off device and equilibrate before loaded on for analysis. Separation of the bound and unbound sample is followed by quantification of the each component in the reaction. One specific type of microfluidic EMSAs that utilized antibody as the affinity reagents is termed as immunoassay.

Homogeneous microfluidic EMSAs have several advantages over the heterogeneous affinity assay. Firstly, compared to the surface-based heterogeneous format, homogeneous format requires no analytes immobilization thereby simplifying the experimental implementation. In some cases, the affinity probe requires special chemical treatment that further adds to the complexity of the assays. Secondly, EMSAs improve the specificity of the assay. Heterogeneous format risks high possibility of non-specific binding when analyzing complex biological samples, as those samples typically contain thousands of proteins that can interact with the affinity probes. With the homogeneous EMSAs format, one could alternatively access the mobility information of migrating bands, thus enabling precise identification of the sample target of interests. Lastly, in certain studies where reaction constant is measured, immobilization could alter the physical property of the affinity reagents, e.g. hiding the binding sites on the molecule, therefore making the measurement results inaccurate. In homogeneous assay, all analytes are kept in free solution, enabling precise characterization of the binding reactions.

Adaption of EMSAs onto microfluidic format has enabled highly sensitive and quantitative measurements compared to conventional tools. Miniaturization substantially reduced experimental time and sample consumption. The first quantitative homogeneous microfluidic EMSAs were developed in the late 1990s by Harrison and co-workers.[30-32] In this pioneering work[30], the researchers used fluorescently labeled anti-bovine serum albumin (BSA) antibody to detect BSA in a standard double-T channel microfluidic chip. The antibody and antigen solutions were mixed off-chip prior to on-chip EMSA. During electrophoresis, the immuno-complex migrated slower than the free antibody and hence the two separated from each other. The abundance of each population was measured with fluorescence quantification. The use of high electric fields greatly accelerated immunoassay throughput. Several other immunoassays were later demonstrated. For example, Huang et al. coupled chemiluminescence (CL) to a competitive assay[33-36]. Here, horseradish peroxidase (HRP)-labeled antigen and its antibody were mixed and loaded on a standard double-T channel for separation. CL reaction solution was introduced downstream the separation channel to visualize the analytes. Human serum proteins including testosterone[33], thyroxine[34,35], and phenobarbital[36] were quantified. Enhanced signal was observed from enzymatic amplification and a lower limit of detection (LLOD) of a few nanomolar was reported. Microfluidic immunoassays were also applied for point-of-care diagnostics. Schmalzing et al.[37] used the standard cross channel microchip as a format for competitive immunoassays to detect thyroxine (T4) in human sera. A fixed amount of fluorescein-labeled T4 and anti-T4 polyclonal antibody were incubated with sera and

separated on-chip, from which the T4 concentration in the sera was determined. The LLOD of the assay was ~40 nM. The detection sensitivity was enhanced to a LLOD of 2.2 nM by introducing chemiluminescence[35].

Quantitative microfluidic EMSAs also report the equilibrium constant K_d. Such measurements are similar to the design of immunoassays. In particular, slight assay modifications were made to accommodate to the measurement of binding pairs with different kinetic natures. For K_D determination of fast-interconverting binding pairs, only one migrating peak is observed as associate/disassociation happens faster than the electro-migration rate, and therefore a weighted mobility of free and bound analytes is recorded and concentrations are calculated. K_D determination in EMSAs of slow-interconverting binding pairs would yield resolvable, distinct peaks for the bound and free analyte, and their concentration information is directly measured from the peak area under the curve. A detailed discussion involves kinetic Damköhler regime and can be found elsewhere[27]. Various groups have demonstrated microfluidic EMSAs that measure K_D for both rapidly and slowly interconverting binding pairs. Chuang et al.[38] fabricated a PEG-modified cross-channel glass microchip, which was free of surface charge adsorption, to measure K_D of estrogen receptor (ER) and estrogen response element (ERE). Such binding pair has rapid interconverting kinetics and the binding disassociation constant K_D was measured via the mobilities of the fluorescently-labeled ERE. For slowly interconverting pairs, Clark et al.[39] studied the self-assembly performance of supramolecular protein-nucleic nanostructures on a commercially available Agilent DNA 7500 labchip. All forms of the assembly structure with different stoichiometry of the DNA backbone and associating proteins are observed, benchmarking the slab-gel results, however, with much lower sample consumption.

Multiplexed microfluidic EMSAs have also been developed to enable high-throughput analysis. Typically, K_D and kinetic measurements rely on a series of concentration titration studies that involve multiple data point collection and the traditional implementation with single-plex microchip format limits its practicability. Additionally, the recent advent of single cell analysis[40] has also called for rapid, quantitative and scaled-up analysis. Therefore, high-throughput microfluidic EMSAs would be beneficial to these analyses. Several researchers have made efforts in creating high-throughput EMSAs platform. For example, Bromberg et al., designed a 96-plex platform by distributing the microfluidic channels radially on a circular glass substrate [41]. In their work, a mixture of fixed concentration of fluorescein-labeled TNT (2, 4, 6-trinitrotoluene) and anti-TNT antibody was incubated with a varying amount of unlabeled TNT, and together analyzed on-chip. Cathode, anode, and waste reservoirs were created in two concentric PDMS rings on the 96-lane radial microchannel plate. Quantitative measurements of unlabeled TNT concentration were demonstrated over a wide dynamic range of ~2 to 530 nM (converted from the concentration units reported by the authors). Though progress has been made to scale up the microfluidic EMSA tools, such efforts are still scarce, and future efforts in this field are warranted.

1.4 Thesis overview

This dissertation reports the development of polyacrylamide gel based high-throughput molecular binding analytical tools. Distinct approaches and microfluidic designs were accomplished to assay two main classes of molecule: RNA riboswitch and fragment antigen-binding fragment (Fab) throughout the dissertation.

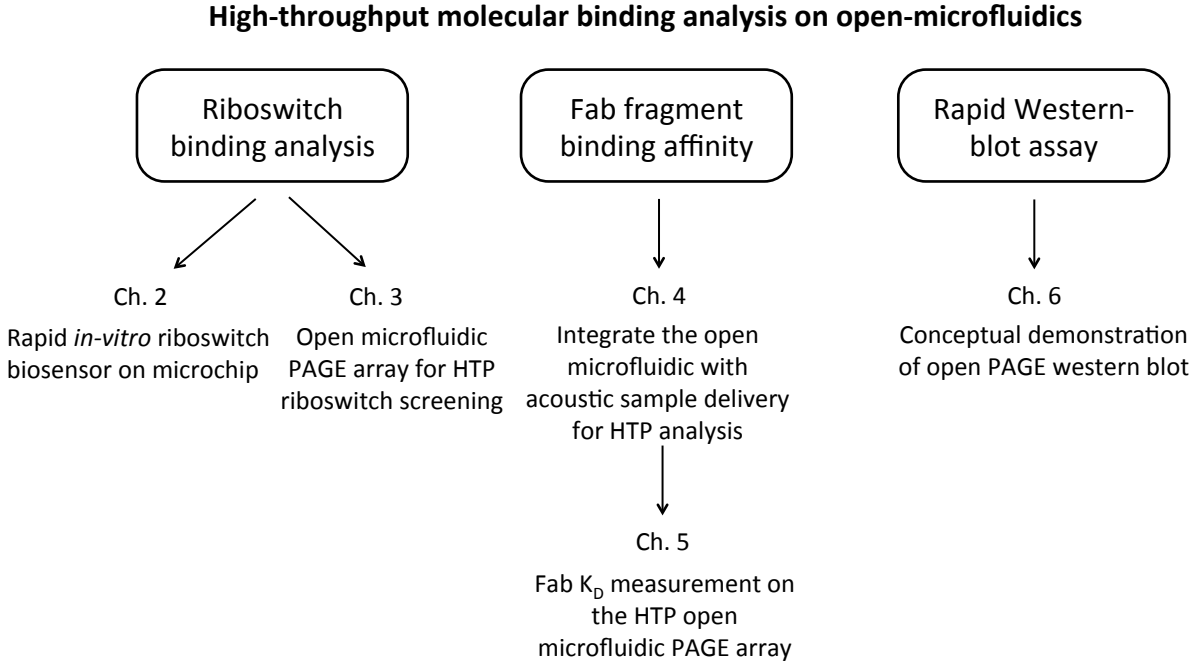

In chapter 2, we developed a rapid in-vitro cyclic-di-GMP riboswitch based biosensor from the previously reported μMSA. We established the standard curve for cyclic-di-GMP concentration and performed successful measurement of cyclic-di-GMP in bacterial cellular extracts. In chapter 3, we detailed the fundamental physical properties of the open microfluidic free-standing polyacrylamide gel electrophoresis assay (*fs*PAGE) and utilized it for HTP riboswitch binding analysis.

In chapter 4 and 5, we pioneered the integration of *fs*PAGE with the acoustic sample delivery system and developed novel automated binding affinity measurement tools for Fab molecules with highest reported throughput. The assay eliminates the cumbersome manual sample loading previously involved in performing *fs*PAGE and greatly improves the electrophoretic uniformity of the assay.

In chapter 6, we demonstrated the conceptual *fs*PAGE western blot assay on a single unit format. The assay features transfer stacking of sample that greatly enhances the detection sensitivity and electrophoretic antibody probing that substantially reduces the assay time.

Chapter 2: Microfluidic riboswitch EMSA for Cyclic-di-GMP biosensing

Reprinted with permission from: Kellenberger, C. A., Sales-Lee, J., Pan, Y., Gassaway, M. M., Herr, A. E., & Hammond, M. C. (2015). A minimalist biosensor: Quantitation of cyclic di-GMP using the conformational change of a riboswitch aptamer. RNA biology,12(11), 1189-1197.

2.1 Introduction to riboswitch and current challenges in riboswitch research

Gene regulation by RNA is widespread in living organism. While most regulation processes rely on transcription-mediated signaling pathway, one common mechanism in bacteria uses certain sequence of mRNA to directly affect the genetic expression. These elements are called riboswitches and are typically located at 5' end of the untranslated region that precedes the translation start site on the mRNA.[42] Riboswitch senses ligand in the cellular domain and react by altering the down-stream mRNA transcription, thereby affecting gene expression. Various types of ligands are reported to target riboswitches, including metallic ions, nucleic acids and amino acids.[43] Riboswitch's ability and function in regulating gene expression is closely tied to secondary RNA structure. Unlike double-stranded helix nucleic acids that form perfect Watson-Crick base pairing, riboswitch RNA folds back on its own structure and forms into double stranded hairpins, and these are helix-segments capped by loops. A brief schematic of riboswitch regulation process is described in Figure 2.1.

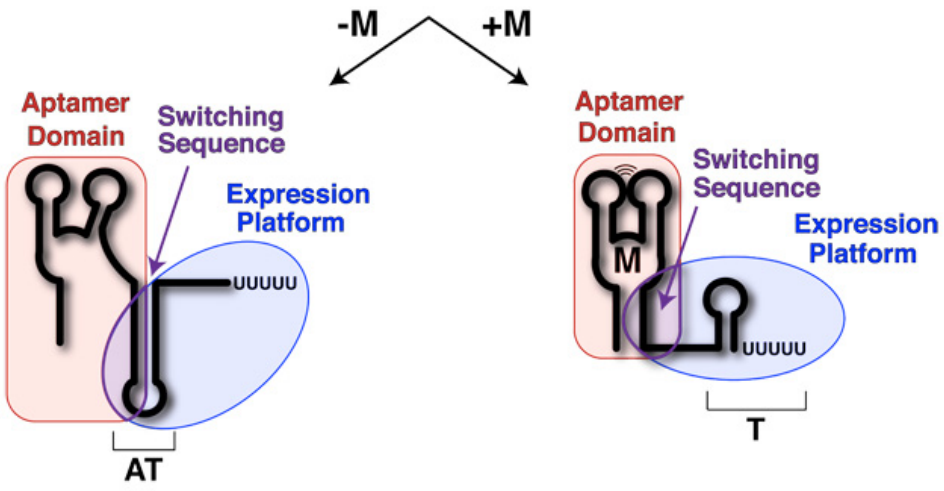

Figure 2.1 Schematic shows riboswitch conformation change with ligand binding. Riboswitch alter secondary structures after gene regulation upon ligand interaction. Riboswitch is composed of an aptamer domain and an expression platform with a switching sequence shared by both. When metabolite (ligand) is not bound (-M), the expression platform would incorporate the switching sequence into an anti-terminator stem-loop (AT) and transcription proceeds. When metabolite binds (+M), aptamer domain would incorporate the switching sequence, and the expression platform folds into a terminator stem-loop (T),

stopping the transcription. In the schematic, aptamer domain (red), switching sequence (purple), and expression platform (blue). ([42]Reprinted with permission from Nature Education 3(9):9. Riboswitches: A Common RNA Regulatory Element.)

A riboswitch is composed of two parts, the ligand binding aptamer domain, and the expression platform domain that switches secondary structure between two states in response to ligand binding on aptamer domain.[44] A segment of switching sequence sits in between, which alternates its position between aptamer and expression domain and affects the RNA transcription. In figure 2.1, when the ligand M is not present, the expression platform incorporates the switching sequence and forms an antiterminator stem-loop and allows the transcription to proceed. When M is present and bound to aptamer, the switching sequence, in turn, incorporates into the aptamer domain and a terminator stem-loop is folded on expression platform, stopping the transcription. In the riboswitch-mediated regulation, molecular conformation change happens on both domains and is a critical step that directly modulates the ongoing transcription process. In fact, most riboswitches discovered reports on transcription-level regulation, while a small number have also been found to act on translation process, e.g., through sequestration of the Shine-Dalgarno sequence.[45] In any cases, conformation change is a critical step involved in riboswitch mediated genetic regulation and both the thermodynamic and kinetic aspects of the process are currently under wide investigation.[46,47]

Riboswitches are classified into families by the ligands they bind to. Up to date, researchers have identified more than 10 families of riboswitch. The target ligands include coenzymes, standard amino acids such as lysine and purine nucleobases. Further, the same family of riboswitch is subcategorized into classes that share common sequence pattern and secondary structure. For example, cyclic di-GMP (c-di-GMP) riboswitches bind the cyclic di-GMP, a second messenger in bacterial cells, in order to regulate a variety of genes controlled by this signaling molecule. Two classes of c-di-GMP have been predicted by bioinformatics and later experimentally identified as c-di-GMP-I riboswitch and c-di-GMP-II riboswitch, who share no known sequence and structural features.[48,49]

Current riboswitch research centers on the following topics: 1) Identify new riboswitches with bioinformatics and experimental tools, 2) Quantitative measurement of riboswitch-ligand binding reaction, 3) Experimentally validate the riboswitch-ligand binding reaction[50], (4) Reengineering riboswitches for gene therapy[9] and 5) Target riboswitch as antibiotic drug development.[8]

Currently, riboswitches were identified through bioinformatic tools (e.g., BLSS, mfold, Rfam, R2R), and special algorithm were designed to look for evolutionary conserved sequence, e.g. those share similarity in the un-translated region on RNA.[51-53] These putative riboswitch candidates were then experimentally validated. However, the development of laboratory validation technique is far lagging behind the progress achieved with computational prediction. Powerful analytical tools would aid in identifying ligand pairs for orphan riboswitches, and expedite the development of other riboswitch-based biomedical application, such as biosensor and antibiotic screening.

Therefore, exploring high-throughput analytical tools for riboswitch screening, ligand pairing and quantitative characterization of binding interaction has become an urgent task for riboswitch study. Current existing riboswitch binding validation primarily relies on bench-top assays that determine ligand binding in a variety of ways. Some common riboswitch binding assays are: Förster resonance energy transfer (FRET)[11], Fluorescence polarization (FP)[12,54], in-line probing[10], equilibrium dialysis assay[55] and isothermal calorimetry[13].

These conventional analytical tools are generally low-throughput for riboswitch binding analysis and suffer from notable limitations. For example, gold standard screening tools, such as FRET and FP, though powerful and sensitive, are slow, and require site-specific labeling of labeling and takes up substantial infrastructure.[56] Recently, droplet microfluidic FP and FRET have improved assay throughput but have not been applied to the study of riboswitches.[57,58]

Alternatively, slab-gel PAGE, is widely used in studying molecular binding interactions. In particular, electrophoretic mobility shift assays (EMSAs), introduced by Garner and Revzin[59], have played an important role in the study of numerous inter-molecular binding reactions including riboswitches. EMSAs measure changes in the physical properties of a target analyte (i.e., size, charge, conformation) upon binding with a ligand. Binding-induced changes can shift the electrophoretic mobility of the target analyte, a measurable quantity allowing characterization of the binding reaction.[60,61] For riboswitch, such mobility shift typically stems from a more compact molecular conformation during ligand binding compared to the unbound form.[62] Therefore, during electrophoresis, the complex/compact structure would exhibit higher electrophoretic mobility and therefore migrate faster in the separation.

However, conventional macro-scale EMSAs are conducted on slab-gel format and slow in separation analysis, making it unsuitable for fast and scaled-up riboswitch binding analysis. For example, binding of the Vc2 GEMM-I riboswitch to its ligand c-di-GMP would induce a significant structural compaction of the riboswitch aptamer, which can be resolved on PAGE EMSAs.[62] However, to resolve the two conformations, that is, to separate the bound and unbound riboswitch on slab gel EMSAs, it would require up to 17 hours.[7] Apparently, slab-gel EMSA lacks the resolving power to separate the small mobility shift by molecular binding induced conformational change, rather than weight or charge. Further, such format is unable to provide quantitative capacity for detailed riboswitch binding analysis.

To expedite research on validating/utilizing riboswitch functionality and binding affinity, as well as high-throughput riboswitch screening/discovery and ligand validation, we need to improve the quantitative analytical capacity of slab-gel EMSAs and develop tools that can provide enough quantitative capability and robust, detailed analysis on riboswitch function.

2.2 Riboswitch binding assay on microfluidic EMSA (μMSA)

Our understanding of riboswitch binding function can be accelerated with advanced high-throughput tools with quantitative capability. In recent years, researchers have introduced a variety of formats that could upgrade the conventional EMSAs systems. An earlier effort was

made by Stebbins et al. where they introduced capillary electrophoresis (CE) for EMSAs to analyze binding between the trp repressor in Escherichia coli and the trp operator (DNA). The mobility shift was resolved in 6 min.[63] Microfluidics was later introduced to further strengthen resolving power of EMSAs and speed up the analytical process. Microfluidics offers high level of repeatability and better quantitative capability, compared to both slab-gel and CE format. Karns from Herr lab introduced microfluidic EMSAs (μMSA) to study the binding characteristics of S-adenosylmethionine-I riboswitches (SAM).[7] As mentioned in the earlier chapter, a key advantage of this microfluidic electrophoresis platform is the efficient heat dissipation due to a large surface area-to-volume ratio in microchannels. Therefore, the favorable thermal transport characteristic enables the use of relatively high electric field (e.g., 400 V/cm on microfluidics and ~10 V/cm on slab PAGE), thus resolving binding pairs in 30 s (compared to 17 h on slab PAGE). The study validated several computationally predicted riboswitch candidates with unparalleled speed and precision, and also quantitatively measured the binding affinity K_D, for two classes of SAM riboswitches with distinct binding kinetics properties with statistical repeatability that's unattainable with conventional slab-gel EMSAs tools.

Microfluidic tools would enable researchers to validate riboswitch-ligand binding reaction and potentially open the door to large-scale riboswitch/ligand screening and new molecules discovery, as well as optimizing conditions[7] for riboswitch binding/ligand selection. In addition, the high-throughput property and unparalleled resolving power offered by microfluidic scalable format also sees a broad relevance in molecular biology research and pharmaceutical industries. This includes but is not limited to constructing bacterial metabolites biosensor[64], engineering artificial riboswitch for genetic control[65] and even gene therapy[66].

2.3 Establishing uMSA sensor for Cyclic-di-GMP

C-di-GMP is an important second messenger signaling molecule in bacteria that play roles in virulence, mobility and biofilm formation. It has been the subject of extensive research. Key questions in c-di-GMP signaling study includes c-di-GMP dependent regulation, temporal resolution of c-di-GMP signaling, and multiplicity of cdi-GMP metabolism enzymes in various bacteria[67]. An essential part in all these studies is the ability to perform quantitative and robust *in vitro* c-di-GMP concentration measurement. Therefore, in order to further advancing c-di-GMP biology we would like to build up a sensitive and facile tool that would allow us to detect the change of concentration if c-di-GMP and study a variety of organisms that uses c-di-GMP as part of metabolism.

Current c-di-GMP detection method such as HPLC-MS[68] typically requires significant sample purification and circular dichroism[69] detects c-di-GMP with low sensitivity (micromolar concentration). Other highly selective fluorescent biosensors rely on natural c-di-GMP protein binder.[70,71] These protein-based biosensors are constructed by fusing fluorescent protein to PilZ domain-containing proteins that together triggers the change in FRET and therefore reports binding events. However, the protein based biosensor are typically used *in vivo*, and would require extensive purification procedure if used *in vitro*.

On the other hand, riboswitch based biosensor for c-di-GMP shows great advantages over conventional approach as riboswitch RNA can be made via *in vitro* transcription, eliminating the time-consuming and laborious purification process and possibility of sample contamination with cellular extracts. To date, the GEMM-I class riboswitch aptamer in Vibrio Cholerae (Vc2) has been coupled to spinach to construct a fluorescence biosensor. Spinach is a RNA mimic of GFP and is fused to riboswitch through its P1 stem.[72] Spinach is capable of binding and switching on the fluorescence of a dye called 3,5- difluoro-4-hydroxybenzylidene imidazolinone (DFHBI).[64] Both spinach and DFHBI are non-fluorescent in unbound form and will fluoresce in the event of binding. For the biosensor, binding to c-di-GMP triggers the conformation change of Vc2 which in turn affects the conformation of the spinach domain. Typically, ligand binding stabilizes the spinach structure and turning on the fluorescence. Other similar approaches have also been developed and studied.[73]

Prior studies have proven the use of riboswitch as a quantitative and reliable *in vitro* c-di-GMP detection method. However, the construction of Vc2-spinach involves sophisticated genetic engineering approach and is not very accessible with standard biology lab setting. On the other hand, the conformation change induced by ligand binding can itself be detected via EMSAs, as such difference would cause a change in electrophoretic mobility of the molecule. Direct detection of mobility shift obviates the need to construct complex Vc2 riboswitch derivatives and would save time in biosensing application. This "minimalist approach" has not been reported before.

The slab-gel EMSAs based c-di-GMP biosensor was constructed with radio labeled (P^{32}) Vc2 riboswitches. A point mutation was introduced to tetraloop in the P2 stem loop of Vc2, impairing a base-stacking interaction with the tetraloop receptor in the P3 stem (A33U Vc2). This introduction had two functions: 1) to increase the relative mobility shift upon c-di-GMP binding, reducing the EMSAs time required to fractionate the bound/unbound population. 2) Reduce the equilibrium time for riboswitch-ligand binding. WT Vc2 has equilibrium time of estimated few months while the A33U Vc2 reaches equilibrium in 75 hours.

Generally, molecular binding equilibrium time depends on the dissociation constant K_D and the concentration of each binder. However, due to signal saturation, the concentration of radio labeled A33U was set as low as 100 pM. To further reduce the equilibrium time, a riboswitch "doping strategy" was utilized, where low amount of P^{32} (100 pM) labeled A33U was added into high concentration of unlabeled A33U (1 uM). With the mixing strategy, the equilibrium was reached in 30 min. Figure 2.2A and 2.2B shows the comparison of equilibrium time before and after the doping strategy. With the addition of excessive unlabeled A33U, the concentration of riboswitch greatly exceeded the K_D, and at this concentration condition, the amount of bound RNA was directly proportional to the c-di-GMP in the sample solution, and more exactly, the c-di-MGP equals that of the bound riboswitch. A standard curve for c-di-GMP was generated in Figure 2.2C.

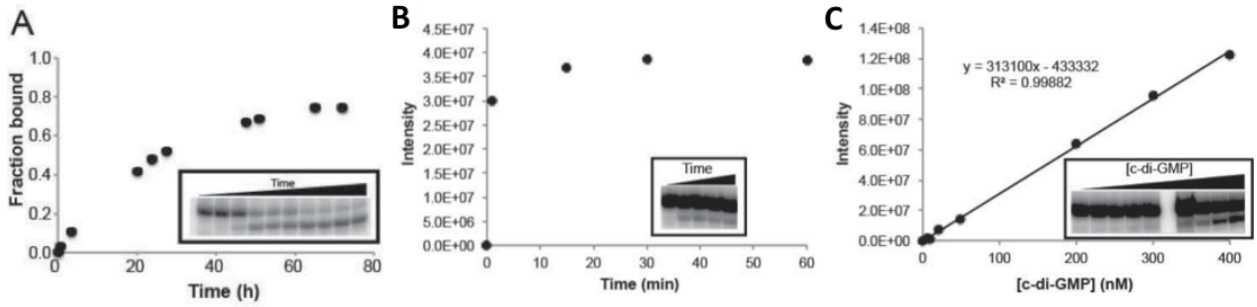

Figure 2.2 Optimization of EMSAs-based c-di-GMP biosensor. (A) Analysis of equilibration time of A33U Vc2 binding c-di-GMP. Less than 100 pM 32^P A33U Vc2 Riboswitch was incubated with 1 nM c-di-GMP for various times before loading on a 10% polyacrylamide gel run for 14 h at 4 °C. (B) Equilibration time for an excess of A33U Vc2 to bind c-di-GMP. Approximately 100 pM 32^P A33U Vc2 was mixed with 1 μM unlabeled Vc2 and 100 nM c-di-GMP, and incubated for various times. Separation was performed on 10% native polyacrylamide gel run for 14 h at 4 °C. (C) Standard curve of c-di-GMP binding A33U Vc2. A range of 0-1000 nM c-di-GMP were incubated with ~100 pM 32^P A33U Vc2 and 1 μM unlabeled Vc2 RNA for 30 min and analyzed on a 10% native polyacrylamide gel run for 14 h at 4 °C. ([50] Adapted with permission from RNA biology 2015, 12, A minimalist biosensor: Quantitation of cyclic di-GMP using the conformational change of a riboswitch aptamer.)

While the reaction time was greatly reduced with the point mutation and doping strategy, the slab-gel format EMSA still require >10 hours gel electrophoresis, which is the limiting factor in scaling up the analysis for high-throughput format. In addition, the traditional slab-gel is resource consuming, making it an unsuitable assay for precious sample testing and assaying.

As detailed in Karns. et al, μMSA is the workhorse that could serve broad riboswitch relevant studies and provides fast, quantitative and reliable analysis. For this particular analysis, we sought to design a μMSA based biosensor that was capable of 1) quantitative precise analysis of peak shift measurement for assessment of c-di-GMP concentration. 2) Comparable equilibrium time and standard curve constructed with μMSA. 3) Resource-sparing operation (low sample consumption, time-efficient analysis). Here, we would detail the design considerations for Vc2 riboswtich analysis, followed up with endogenous c-di-GMP concentration measurements in real cell extracts.

2.4 Materials and Methods

Reagents. DNA oligonucleotides encoding the riboswitch sequence were purchased from Elim Biopharmaceuticals (Hayward, CA) and IDT (Coralville, IA). C-di-GMP was purchased from Axxora, LLC (Farmingdale, NY). Alexa Fluor 488 (AF488)-labeled trypsin inhibitor (TI) was purchased from Invitrogen (Waltham, MA).

***In vitro* transcription.** DNA templates were made through PCR amplification using primers that added the T7 polymerase promoter sequence. The templates were transcribed using T7 RNA polymerase (NEB, Ipswich, MA) in 40 mM Tris-HCl, pH 8.0, 6 mM $MgCl_2$, 2 mM spermidine, and 10 mM DTT. RNA was purified by denaturing (7.5 M urea) 6% polyacrylamide gel electrophoresis (PAGE) and was extracted from gel pieces using Crush Soak buffer (10 mM Tris-HCl, pH 7.5, 200 mM NaCl and 1 mM EDTA, pH 8.0). RNAs were precipitated with ethanol and re-suspended in TE buffer (10 mM Tris-HCl, pH 8.0, 1 mM EDTA). Thermal hydrolysis assay was used to determine the accurate RNA concentrations.[74]

Fluorescent RNA labeling. RNAs were fluorescently labeled with AF488. Briefly, the 3' end of the RNA was oxidized with sodium periodate and then AF488 hydrazide (Life Technologies, Carlsbad, CA) was coupled to the RNA in sodium acetate buffer. The RNA was precipitated in ethanol and then purified by PAGE as previously described.

Microfluidic device fabrication. Glass microfluidic chips (N12B) were designed in-house and fabricated with standard wet etching process by Perkin Elmer (Hopkinton, MA). Prior to gel polymerization in-chip, each microchannel was washed with 1 M NaOH for 10 minutes. To prepare the chip for polyacrylamide gel polymerization, the microchannels were silanized with a degased solution of 3-(trimethoxysilyl)-propyl methacrylate (Sigma Aldrich, St. Louis, MO), glacial acetic acid (Sigma Aldrich), and water (Mediatech, Menassas, VA)(2:3:5, v/v/v). The solution was introduced to the chip by capillary force and incubated for 30 minutes and then washed with methanol and water. A 3%T to 18%T discontinuous polyacrylamidegel (%T indicates the total concentration of acrylamide: bis, w/v; 3.3% was the weight percentage of bis-acrylamide in total monomer, w/w) was employed to enhance the separation resolution. The discontinuous gel was fabricated with UV photopatterning. First, the gel precursor solutions were prepared by diluting 30% (w/v) acrylamide/bis-acrylamide (Sigma Aldrich, St. Louis, MO) with the 10× Tris-Borate (TB) buffer and water to achieve the desired total acrylamide concentration (3%T, 10%T or 12%T). The precursor contains 1× TB buffer with 0.2% (w/v) watersoluble photoinitiator 2,2-azobis[2-methyl-N-(2-hydroxyethyl) propionamide] (VA-086, Wako Chemicals, Richmond, VA). Precursor solutions were degassed using sonication (~5 min) before use. 18%T gel was first introduced into the channel with capillary action and used as separation gel. Then, the chip was aligned over a transparency mask with a 4 mm x 500 μm opening (designed in-house and fabricated by CAD/Art Services,Inc., Bandon, OR) so that the region of the separation channel directly downstream of the injection junction was exposed. The mask and glass chip were aligned on an inverted Nikon Diaphot 200 microscope (Melville, NY) and the exposing UV light was sourced from a Hamamatsu Lightning Cure LC5 UV light source (Hamamatsu City, Japan) through a UV transmission objective lens (UPLANS-APO 4x, Olympus, Center Valley, PA) on the microscope. The masked chip was exposed to UV light for 270 sec at a beam intensity of ~4.5 mW/cm2 (measured with a UV513AB Digital Light Meter, General Tools, New York, NY). After that, unpolymerized precursor solution was replaced with 3%T precursor solution by sequentially applying vacuum to wells RW, BR, and RR (Figure 2.3A). Once the 3% precursor solution was in place, the entire chip was then flood exposed for 8 min at ~10 mW/cm^2 on a 100 W filtered mercury UV lamp (UVP B100-AP, Upland, CA).

μMSA operation. μMSA device is a glass microfluidic chip comprised of 2 intersecting microchannels (80 mm deep and 20 mm wide), each terminating in fluid wells (See Figure 2.3A for device infrastructure). Fluid wells are notated as: reagent reservoir (RR), reagent waste (RW), buffer reservoir (BR), and buffer waste (BW). Pipette tips (1 cm long) were cut and placed into the wells to expand the reservoir volume. Run buffer (1X TBMK) contained 89 mM Tris, 89 mM boric acid, 3 mM MgCl2, and 10 mM KCl. The binding reactions (10 μL) were prepared in 0.5 mL Eppendorf Lo-Bind tubes which contains the following components: 1X TBMK, 1 mM riboswitch RNA, 100 mg/mL yeast tRNA, 500 nM AF488-conjugated trypsin Inhibitor (TI*) and indicated concentrations of c-di-GMP. Yeast tRNA is used to protect the riboswitch RNA from degradation by RNases. TI* was used as an internal standard for precise quantification. The mixture was heated at 70 ℃ for 3 min and cooled for 10 min at room temperature to renature the RNAs before mixing withc-di-GMP and TI*. The riboswitch binding reaction was incubated off-chip and 4 μL sample was pipetted into the RR. Other wells were filled with 4 μL of 1X TBMK buffer. To provide electricity, platinum electrodes were inserted into each well and were connected to a custom built, 8-channel high voltage power supply with current/voltage feedback control. μMSA was performed in constant current mode. First, samples were electrophoretically loaded into the RR-to-RW microchannel by applying -12 mA to the RR. At the same time, -2 mA were applied to both BR and BW as pinching voltage and grounding RW for 1 min. After the loading process was stabilized, the voltage plan was switched to sample injection/separation, by applying -32 mA to BR, 10 mA to RR and RW as pulling voltage and grounding BW. The result was the injection of a plug of sample into the separation channel at the t-junction and the sample was electrophoresed into the BR-to-BW microchannel, which housed a 3–18 %T discontinuous sample stacking and separation gel.

μMSA imaging and data analysis. Full-field images of peak migration and fluorescence were collected via an Olympus IX-70 inverted epi-fluorescence microscope equipped with a Peltier cooled charge-coupled device (CCD) camera (CoolSNAP HQ2, Roper Scientific, Trenton, NJ) and a 10X objective. An X-Cite1 exacte mercury lamp (Lumen Dynamics, Mississauga, Canada) provided the illumination source, which was then filtered by an XF100-3 filter (Omega Optical, Brattleboro, VT). In equilibrium time studies, the camera exposure time was 100 ms. For concentration calibration, electrophoresis was monitored in real time and halted when the unshifted RNA band migrated to the 1 mm marker, followed by collection of a 500 ms exposure image. Images were analyzed using ImageJ software (NIH, Bethesda, MD). Fluorescence intensity was collected along the axis of the separation channel and averaged in the transverse direction. Post-processing was performed with OriginPro 8.0 (OriginLab, Northampton, MA). A built-in non-linear Gaussian peak-fitting algorithm was employed to calculate peak position and area under-the-curve (AUC) from the axial fluorescence signal. To quantify the amount of bound riboswitch, we introduced TI^* as an internal standard molecule. Instead taking the absolute value of AUC of the bound riboswitch, we normalized it to that of TI therefore minimizing the run-to-run variation. Signal-to-noise ratio (SNR) was calculated by dividing the maximum intensity value of the Gaussian fit by the root mean square (r.m.s) noise of neighboring regions of signal. Peaks were considered detectable when SNR >3, as per convention.

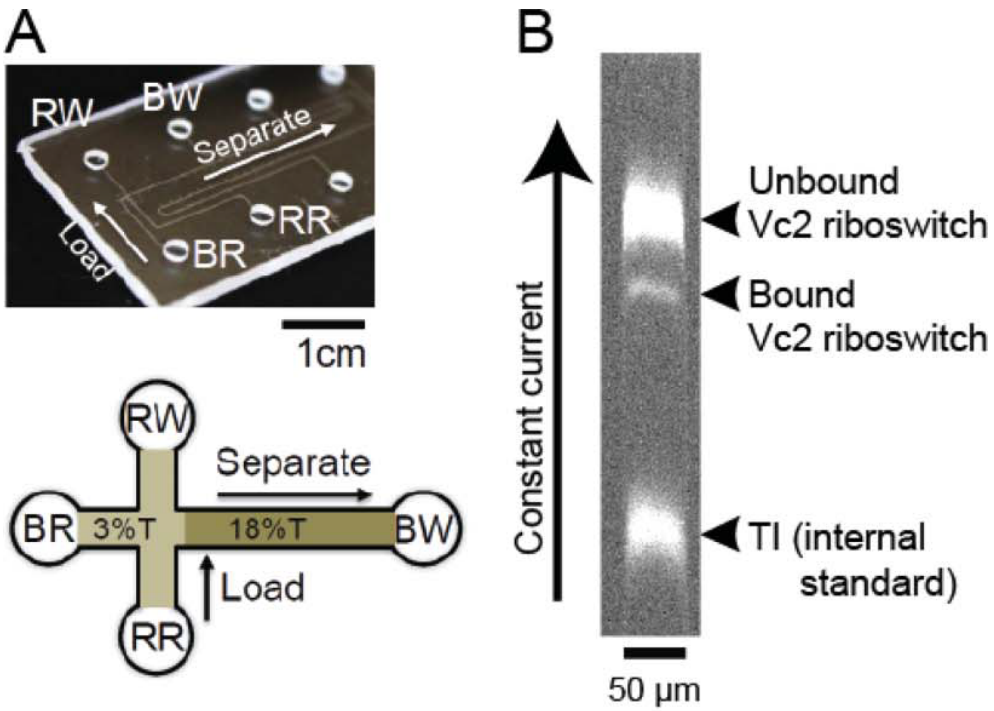

Figure 2.3 µMSA enables rapid separation of bound and unbound riboswitch with conformation change. (A) Photograph of the µMSA glass chip. Microchannel network is comprised of two intersecting microchannels, each terminating in a fluid reservoir. Reservoirs are: buffer reservoir, BR; riboswitch reservoir, RR; riboswitch waste, RW and buffer waste, BW. Bottom is simplified schematic of the microchannel network. (B) Example of full-field image of binding experiment. A binding reaction containing 100 nM c-di-GMP and 1 µM AF-labeled RNA was incubated for 60 min and was then loaded on a polyacrylamide gel run for 30 s at RT. ([50]Reprinted with permission from RNA biology 2015, 12, A minimalist biosensor: Quantitation of cyclic di-GMP using the conformational change of a riboswitch aptamer.)

Cell extraction of E. coli. E. coli strains from the Keio collection[75] were obtained from the E. coli Genetic Stock Center (Yale University). The wild-type E. coli K-12 strain was BW25113 [F-, Δ(araD-araB)567, ΔlacZ4787(::rrnB-3), λ–, rph-1, Δ(rhaD-rhaB)568, hsdR514]. Mutant strains were isogenic derivatives of BW25113 and included JW1278-1 (Δgmr-722::kan), JW2052-1 (ΔyegE-765::kan), JW3493-2 (ΔyhjH-780::kan), JW5291-1 (ΔyeaJ-783::kan). Fresh cultures of 15 mL of LB (BW25113) or LB/kanamycin (mutant strains, 50 µg/mL kanamycin) were inoculated 1:40 with overnight cultures grown at 37 °C. Cultures were grown in a 37 °C incubator with shaking for approximately 7 h, then the OD600 was measured and cell pellets were collected by centrifugation at 4,500 rcf for 10 min at 4 °C. An organic-aqueous extraction of cell pellets was performed as described previously[68]. Briefly, the pellets were resuspended using 600 µL acetonitrile/methanol/water (40/40/20, v/v/v) on ice for 20 min with occasional vortexing. The suspension was further extracted at ambient temperature for 20 min, then cell debris was pelleted with centrifugation at 13,200 rpm for 20 min at 4 °C. The supernatant was carefully removed and stored on ice and the pellet was extracted twice more with 300 µL extraction buffer. The combined supernatants were

evaporated to dryness by rotary evaporation and the dried material was resuspended in 200 µL deionized H_2O. For analysis by µMSA, 5 µL of concentrated extract was added to bring the final volume of the riboswitch binding reaction to 10 µL (final concentrations are 1 µM renatured AF488-labelled RNA, 100 µg/ml tRNA, 1X TBMK buffer and 500 nM TI*). The reported c-di-GMP concentration values are for the concentrated cell extract, take into account the 2X dilution factor, and are normalized to OD600.

2.5 Characterize the µMSA design for c-di-GMP sensing

The microfluidics has several advantages over conventional slab-gel format in performing EMSAs. Generally, we use separation resolution (SR) to quantify the separation between two bands. According to chapter 1, SR can be calculated as:

$$\mathrm{SR} = \frac{(\mu_1 - \mu_2)\mathrm{Et}}{2(\sqrt{{\sigma_0}^2 + 4\mathrm{D}_1\mathrm{t}} + \sqrt{{\sigma_0}^2 + 4\mathrm{D}_2\mathrm{t}})} \quad (1)$$

µ is the electrophoretic mobility of band, E is the electric field used in electrophoresis and t is the elapsed time. The product of mobility difference, electric field and time equals the distance between two peaks. σ_0 is the initial standard deviation of the width of the band and D is the diffusion coefficient of the analytes. As can be seen from this equation, increasing E or decreasing σ_0 can both increase the SR with in a certain period of time, and that is realized on microfluidic EMSAs. Firstly, as described in Section 2.4, up to 400 V/cm electric field was applied during EMSA separation to expedite the separation of bound and unbound A33U, compared to 10-20 V/cm with slab-gel electrophoresis. Secondly, initial bandwidth in microfluidic format equals the width of the channel at ~30 µm, compared to few millimeter in the slab gel format. As a result, mobility shift were successfully resolved on the 18%T separation channel of µMSA in 30 seconds (shown in Figure 2.3B). On the other hand, the same process took up ~12 hours to complete. The use of microfluidic achieved ~1440 fold reduction in separation time.

2.5.1 Binding equilibrium study

To inform the design of c-di-GMP biosensor, the dynamic binding equilibrium process was monitored to record the time required to reach equilibrium. Unlike the radiolabeling sample that reports pM detection sensitivity, 1µM fluorescent A33U riboswitch was used as the probing reagents to enhance the sample visualization and reduce the equilibrium time. In experiments, the binding solutions were prepared and quenched with 50% glycerol water solution at 1, 5, 15, 30, 60, 90 and 120min. The quenched solution was assayed with µMSA and the intensity ratios of bound RNA to the internal standard (TI) were calculated at each time point. Figure 2.4A shows the time-dependent A33U signal equilibrating with c-di-GMP. As can be seen from the figure, the reaction reaches equilibrium in less than 30 minutes.

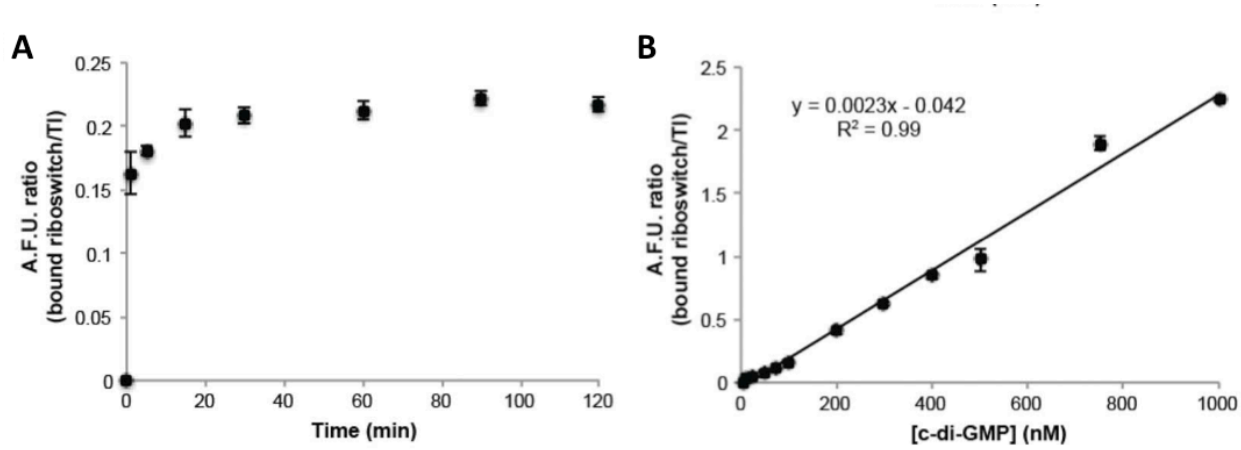

Figure 2.4 Characterization of the µMSA biosensor. (A) Analysis of equilibration time required for an excess of RNA to equilibrate with c-di-GMP. Binding reactions containing 1 µM Alexa Fluor 488-labeled RNA and 100 nM c-di-GMP were incubated for a series of times and subsequently loaded on µMSA for 30 s' separation at room temperature. (B) Standard curve of A33U Vc2 binding c-di-GMP. A binding reaction containing 1 µM Alexa Fluor 488-labeled RNA with 0-1000 nM c-di-GMP concentrations was incubated for 60 min and subsequently analyzed on µMSA for 30 s at room temperature. In all studies, TI* was used as an internal standard. A.F.U. stands for arbitrary fluorescence units. ([50]Reprinted with permission from RNA biology 2015, 12, A minimalist biosensor: Quantitation of cyclic di-GMP using the conformational change of a riboswitch aptamer.)

2.5.2 Concentration titration study

A standard curve for c-di-GMP detection was generated via µMSA using 1 µM AF488-labeled RNA with c-di-GMP concentration ranging from 0-1000 µM. The bound RNA increases linearly with the concentration of c-di-GMP (Figure 2.4B). The lower detection limit is 10 nM, at which the SNR ratio is ~6.7(See Figure 2.5). This concentration linearity and detection sensitivity were comparable to the slab-gel format. Therefore, the benefits of µMSA as well as the great reduction in analysis time make the assay an advantageous assay for sensitive and rapid c-di-GMP measurements.

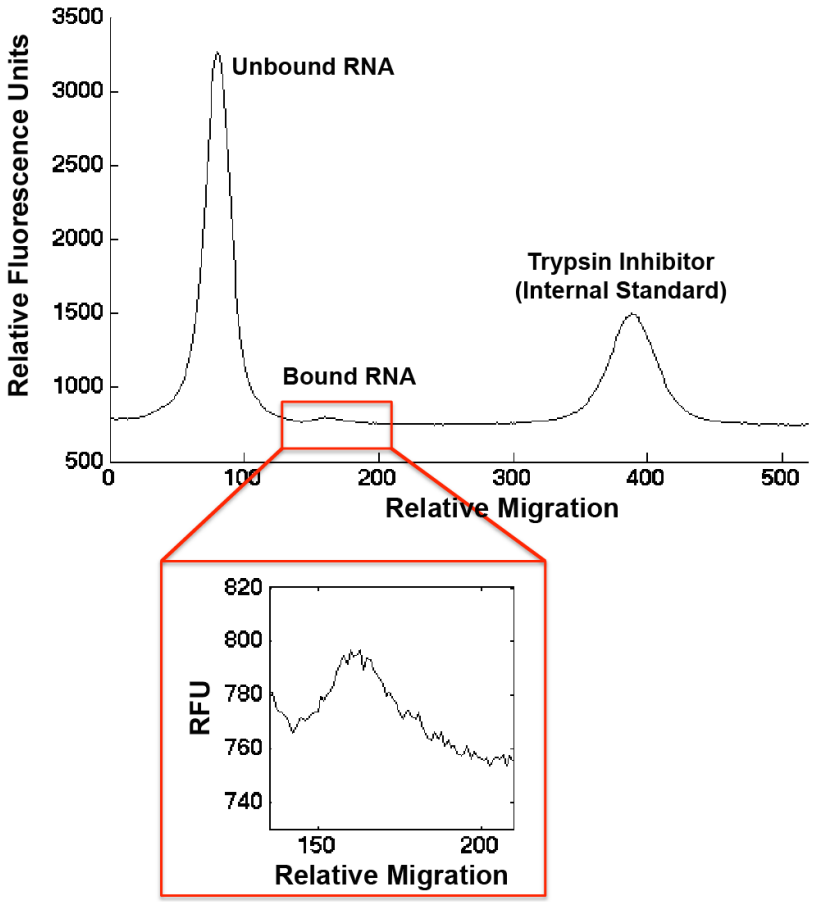

Figure 2.5 Detection limit of µMSA using 1 µM RNA. The electropherogram from a µMSA assay with 1 µM RNA and 10 nM c-di-GMP is shown. The inset highlights the SNR (~6.7) of the bound RNA band under these conditions. ([50]Reprinted with permission from RNA biology 2015, 12, A minimalist biosensor: Quantitation of cyclic di-GMP using the conformational change of a riboswitch aptamer.)

2.6 Cellular extract measurement with µMSA

The µMSA was used for *in vitro* c-di-GMP detection in real sample extract sample. Previous studies have shown that phosphodiesterases and diguanylate cyclases will affect biofilm formation and/or motility phenotype in different E. coli strains[76,77], and therefore it is believed that these two molecules were active in adjusting the c-di-GMP concentration in bacterial cells. We expected that knocking out the phosphodiesterases would increase c-di-GMP concentrations and knocking out the diguanylate cyclases would decrease c-di-GMP concentrations. Here, we measured the c-di-GMP concentrations in these mutant strains to validate the µMSA usage.

We performed an organic-aqueous extraction of cell pellets from Keio collection strains grown to stationary phase (OD600~3) and measured the endogenous c-di-GMP concentrations. The strains analyzed were BW25113, the wild-type E. coli K-12 strain, and

isogenic derivatives of BW25113 with the following single gene deletions: Δgmr, ΔyhjH, ΔyegE, and ΔyeaJ. GMR and yhjH are both deletion mutants of phosphodiesterases and yegE and yeaJ are deletion mutants of diguanylate cyclases. Theoretically, Δgmr and ΔyhjH were expected to have higher concentration of c-di-GMP and the rest two mutants having lower concentrations.

We quantified c-di-GMP levels directly from these crude cell extracts via μMSA and triplicate runs on the μMSA platform gave consistent values for each sample. (See Figure 2.6) However, we unfortunately observed high variability between two independent biological replicates from experiments performed on two different days. We hypothesized this is likely due to the facts that the Keio strains were not the same strains used in the phenotype assays, and the growth conditions were different as well. These differences may change the expected c-di-GMP concentrations, as E. coli harbor multiple diguanylate cyclases and phosphodiesterases (up to 29) whose expression levels are influenced by growth conditions.

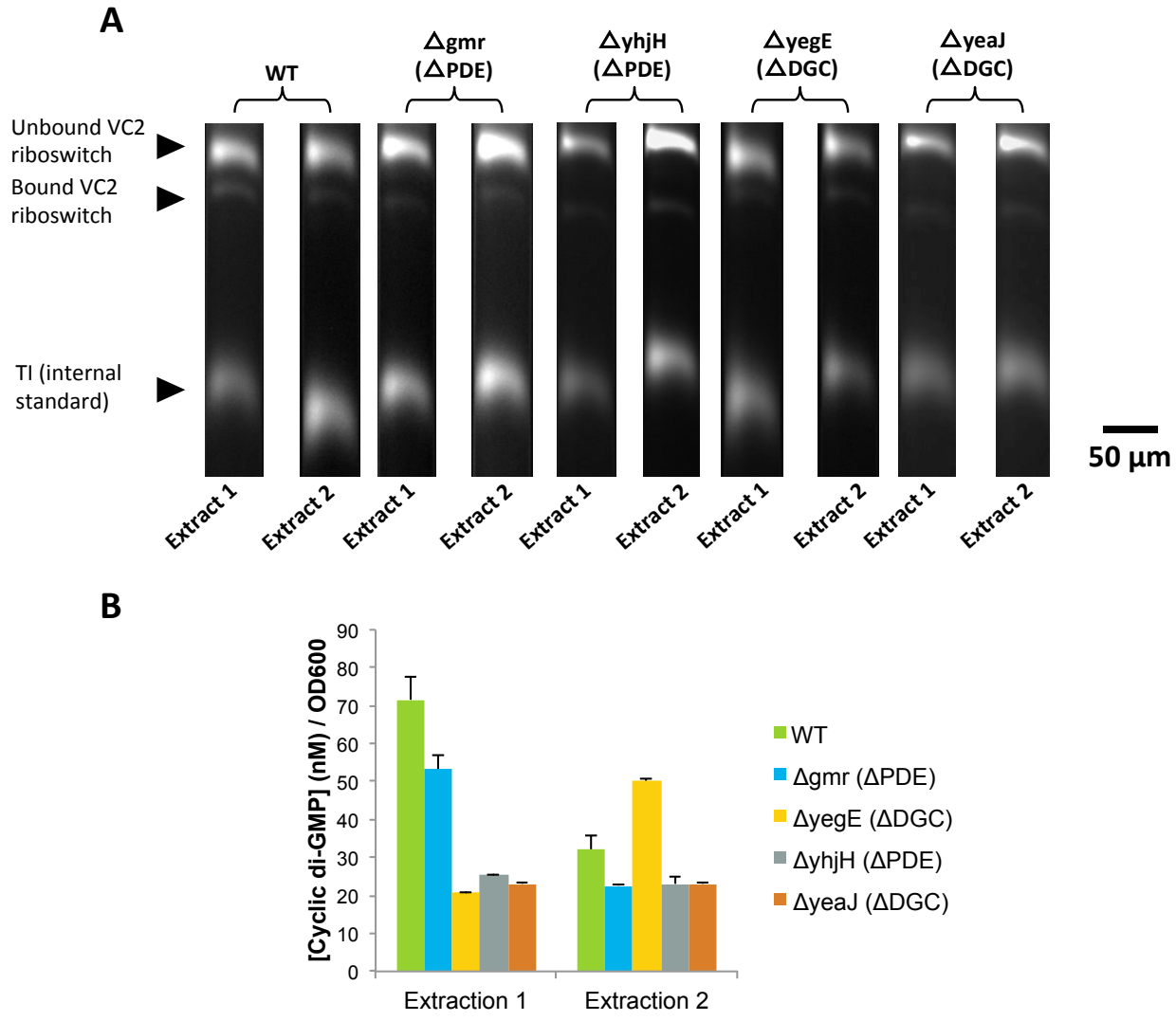

Figure 2.6 Direct detection of c-di-GMP from crude E. coli cell lysates via μMSA. Quantifications of c-di-GMP are shown for two sets of independent biological replicates. (A) Electrophoretic separation of bound and unbound riboswitch for each sample. (B) Cyclic-di-GMP concentration quantification for each sample. Error bars represent the standard deviation from triplicate measurements via μMSA. ([50]Adapted with permission from RNA biology 2015, 12, A minimalist biosensor: Quantitation of cyclic di-GMP using the conformational change of a riboswitch aptamer.)

2.7 Conclusion

By introducing an electrophoretic mobility shift assay for the detection of riboswitch conformation change, we established a "minimalist biosensor" for *in vitro* c-di-GMP concentration measurement. Careful adaption of the assay onto microfluidics format yields high-resolution and quantitative RNA separation with resource-sparing operation. An important outcome of this integration is that it provides an assay that can be accomplished in a practical time-scale amenable for mass adoption for laboratory test with only low-amount of fluorescently labeled riboswitch RNA. The fluorophore labeling procedure on the *in vitro* transcribed riboswitch, combined with the μMSA strategy, can potentially be applied on RNA of any kind and length.

We foresee future assay optimization to potentiate the accurate concentration measurement of c-di-GMP from crude cell extract samples. The high variability of cell extract results likely revealed a major challenge in the difference of biological sample and extraction efficiency. Hopefully, with the high-throughput analytical capability offered by μMSA, large number of cell sample replicates can be assayed and any statistical significance can be reliably characterized.

Chapter 3: High-throughput free-standing polyacrylamide gel electrophoresis (*fs*PAGE) for riboswitch EMSAs

Reprinted with permission from: Pan, Y.; Duncombe, T. A.; Kellenberger, C. A.; Hammond, M. C.; Herr, A. E. Analytical chemistry **2014**, 86, 10357-10364. http://pubs.acs.org/doi/full/10.1021/ac502700b

3.1 Introduction

In chapter 2, we introduced use of microfluidic electrophoretic mobility shift assays (μMSA) for quantitative binding analysis of riboswitch.[7] Compared to the traditional slab gel EMSAs, the microchip-based assay permits use of much higher separation electric field (40 times) with substantially lower sample consumption (few μL), reducing the total processing time for up to 1000 times.[7,78,79] We have further adapted the system into a riboswitch based in vitro cyclic-di-GMP biosensor for crude bacterial cell extracts measurements.[50]

However, regardless of the rapid analysis, the microchip format was limited to single and serial implementation of separations. Consequently, though the separation took only 30 seconds, the entire assay protocol (i.e., loading-separation-washing) required ~3 min, limiting usefulness in high-throughput screening. A recent breakthrough in increasing analytical throughput takes advantage of multiplexed formats. In 2000, Ferrance et al.[80] demonstrated an 8-plex multichannel microfluidic separation system for rapid clinical diagnostics. Later, Ross and colleagues[81] demonstrated a 16-plex gradient elution moving boundary electrophoresis tool for monitoring enzyme activity and inhibition. Researchers have also introduced microfluidic systems compatible with powerful, conventional biological tools (e.g., a microplate format). For example, a 384-plex radial microfluidic capillary electrophoresis tool developed by Emrich et al.[82] supported ultrahigh-throughput genetic analyses. In 2003, Gaunt et al.[83] established a microplate gel array platform for SNP genotyping, in which a PAG molded with sample wells was seated on a silane-treated glass plate. With the molding strategy, 768 wells were fabricated in the PAG sheet, yielding the highest reported multiplexed electrophoresis tool to our knowledge. At the single-cell level, Gutzkow et al.[84] developed a 96-plex minigel platform for high-throughput comet assays, using cell-suspended agarose droplets patterned on a piece of polyester film (Gel bond). Engelward and colleagues[85,86] have developed the CometChip, a sheet of agarose gel patterned with microwells that house single cells. The CometChip has been applied to assess genotoxicity mediated by engineered nanoparticles. In 2014, the Herr lab introduced a microfluidic device that enables completion of thousands of concurrent single-cell western blots.[40]

Building on our previous work which reported electrophoretic resolution of proteins in 96-plex *fs*PAG electrophoresis (*fs*PAGE) assay[87], we now address an unmet throughput need for riboswitch screening. We detail design considerations for successful introduction of multiplexed *fs*PAG-EMSAs. Screening for changes in riboswitch conformation presents new analytical challenges for an EMSA system. For context, our previous *fs*PAGE protein

analyses measured large relative electrophoretic mobility shifts between adjacent peaks (i.e., 2x changes in the electrophoretic mobility) in a standard low conductivity buffer. Riboswitch mobility shifts are comparatively small – 10% relative mobility shifts (bound and unbound) – and require high conductivity buffers, which limits the possible assay time before heating effects disrupt the assay. In this work, we quantitatively characterized the *fs*PAGE platform and optimized the system to improve sample injection and resolving power over short migration distances and assay times. Through optimization studies, we determined optimal conditions for performing high-throughput (< 3 min electrophoresis) and massively multiplexed (96-plex) *fs*PAGE. In the process, we elucidated fundamental physical relationships inherent to the *fs*PAGE platform, not previously described.[87] In addition, this work analyzed how the electrode proximity to EMSA units affected electrophoretic velocity variation across the large 96-plex array. Through optimization, we achieved excellent unit-to-unit uniformity across a 96-plex array – an important advance over previous *fs*PAGE studies.[87] After optimization, we applied the *fs*PAGE-EMSA platform to 96 concurrent EMSAs of the Vc2 riboswitch aptamer binding interaction with c-di-GMP. *fs*PAGE-EMSAs yielded assay throughput of 10 data points per minute, orders of magnitude more efficient than either conventional slab or microfluidic EMSAs. Successful *fs*PAG-EMSAs may form the basis for large-scale screening of riboswitches and other macromolecular targets.

3.2 Materials and Methods

Reagents. Solutions of 30% (w/v) (29:1) acrylamide/bis-acrylamide, glacial acetic acid, glycerol, and Triton X-100 were purchased from Sigma Aldrich (St. Louis, MO). 10X Tris-borate-magnesium-potassium (TBMK) run buffer was prepared by dissolving 890 mM tris base (Fisher Scientific, Hampton, NH), 890 mM boric acid (Fisher Scientific), 30 mM magnesium chloride (EMD chemical, Gibbstown, NJ) and 100 mM potassium chloride (Sigma Aldrich) into 1 L of molecular biology grade (DNase-, RNase- and Protease-free) water (Mediatech, Manassas, VA). AlexaFluor 488 (AF488) conjugated Trypsin Inhibitor (TI*, 21 kDa), Ovalbumin (OVA*, 45 kDa) were purchased from Life Technologies Corporation (Carlsbad, CA). Photoinitiator 2,2-azobis [2-methyl-N-(2-hydroxyethyl) propionamide] (VA-086) was purchased from Wako Chemical (Richmond, VA). GelBond® PAG film was purchased from Lonza (Basel, Switzerland). Photo-masks were designed with AutoCad® student edition (Autodesk, San Rafael, CA) and printed with Brother MFC-9320C digital color printer (Brother International Corporation, Bridgewater, NJ) on a transparent film (3M, St. Paul, MN).

Preparation of RNAs. Fluorescent riboswitch RNAs were prepared according to protocol described in Karns et al.[7]. Briefly, DNA templates were generated using primers that appended the T7 promoter sequence directly upstream of the aptamer sequence. RNAs were then transcribed in vitro using T7 RNA polymerase (NEB) and purified by denaturing PAGE following standard protocols. Following oxidation of the 3' ribose with $NaIO_4$, RNAs were reacted with AlexaFluor 488 hydrazide in the dark, and purified via denaturing PAGE. The accurate RNA concentration was determined via a thermal hydrolysis assay[88] to remove effects of hypochromicity, and the labeling efficiency was calculated as previously described[7].

Protein (TI* and OVA*) solutions were prepared by diluting a stock solution with water and 10X TBMK into indicated concentrations. To prepare the binding reaction solution, c-di-GMP riboswitch, 10X TBMK buffer, 1 mg/ml yeast tRNA and water were mixed in a 0.5 ml Eppendorf Lo-Bind tube at indicated concentrations. The final mixture solution contained 1X TBMK, 100 μg/ml yeast tRNA and c-di-GMP riboswitch. Yeast tRNA is used to improve the stability of RNA against degradation. The mixture was heated at 70 ℃ for 3 minutes and cooled for 10 min at room temperature to renature the RNA. C-di-GMP and an internal standard (TI*) were added into the solution. The sample mixture was placed in a dark room and equilibrated at room temperature for 1 hour.

***fs*PAG fabrication and electrophoresis operation.** *fs*PAGs were fabricated via UV photopatterning.[87] The PAG precursor solution contained 20%T acrylamide (w/v), 3.3%C bis-acrylamide crosslinker (w/w) and 0.2% VA-086 photo-initiator (w/v). Prior to UV exposure, the precursor solution was degassed for 2-3 min under house vacuum with sonication. To briefly recap the fabrication, a surface-functionalized polymer sheet (Gelbond®) was placed on top of a borosilicate glass substrate. Two spacers with predefined thickness (greater than Gelbond®) were then aligned on two sides of Gelbond® and a glass plate was laid on spacers to act as top cover. The PAG precursor solution was pipetted into the gap between the Gelbond® and the glass cover, such that the height of *fs*PAG was defined by the height difference between the spacers and the Gelbond® (from 70 to 600 μm). The PAG precursor solution was then exposed to UV light through a photo-mask, selectively polymerizing the regions of interest. The intensity and time for UV exposure were optimized for each monomer concentration. For 20%T 3.3%C PAGs, 70 s exposure at 20 mW/cm^2 (measured by OAI 308 UV intensity meter, OAI, San Jose, CA) was employed. After UV exposure, the polymerized *fs*PAG structures were gently washed with water to remove unpolymerized monomers. The entire process (mask design, printing and gel fabrication) takes 1 hour, making the process amenable to rapid prototyping of new device designs and gel conditions. *fs*PAG height was measured with MicroXAM-100 Optical Profilometer (ADE Phase Shift, Tucson, AZ).

After photopatterning, the *fs*PAG was soaked in run buffer for 10 min on an Orbitron shaker. When removed, a pipet tip connected to house vacuum was applied to and around each well to remove residual run buffer via suction. Sample solution was then manually pipetted into the sample wells. Two electrode wicks wetted with run buffer were aligned atop the *fs*PAG at both ends of the sheet-like structures. Graphite electrodes were placed in contact with the electrode wicks. The entire electrophoresis setup was housed in an environmental chamber[87] and connected to an external high-voltage power supplier (PowerPac HV; Bio-Rad Laboratories). Unlike conventional slab gel electrophoresis, submerging the thin *fs*PAG structure in buffer confounds the assay in three ways. Firstly, submerging the *fs*PAG structure makes loading of the <1 uL sample volumes into the injection wells difficult. This is because ultra-low volume loading relies on hydrophilicity of well surface which loses effectiveness when submerging under buffer solution. Secondly, owing to the placement of the electrode wicks and the use of thin *fs*PAG features (z-axis), submersion leads to loss of analyte, as species readily disperse out of the thin gel and into covering buffer layer due to diffusion and z-component of electric field. Mass losses to the buffer layer result in reduced detection sensitivity performance. Lastly, the covering buffer greatly increases the system conductivity, which leads to higher current value and temperature, potentially affecting the

binding affinity. Unless otherwise stated, *fs*PAGE was performed with 100 μm 20%T *fs*PAG in 1X TBMK buffer containing 20% glycerol at an applied electric field of 60 V/cm.

Imaging. Fluorescence imaging was conducted using an inverted epi-fluorescence microscope (Olympus IX-70) equipped with a 2X objective (PlanApo, N.A. = 0.08, Olympus, Center Valley, PA). The illumination source was an X-Cite® exacte mercury lamp (Lumen Dynamics, Mississauga, Canada) filtered through an XF100-3 filter (Omega Optical, Battleboro, VT). A Peltier cooled charge-coupled device (CCD) camera (CoolSNAP HQ2, Roper Scientific, Trenton, NJ) attached to the microscope collected fluorescence images. Large area imaging for the 96-plex EMSAs was performed with a scan slide function controlled by Metamorph software (Molecular Devices, Sunnyvale, CA). Image processing was performed with ImageJ (NIH, Bethesda, MD) and subsequent data analysis was performed with OriginPro 8.0 (OriginLab, Northampton, MA). Fluorescence intensity profiles were generated by averaging the fluorescence signal over the transverse dimension of *fs*PAG and each peak was fitted with Gaussian distribution. To quantify the fluorescence intensity of the analytes, we took the height of the Gaussian peaks. To quantify the resolving power of electrophoresis, we utilized the metric separation resolution (SR), defined as $SR=\Delta L/4\sigma$. ΔL is the distance between bands (scale with migration distance) and σ the standard deviation (band width=4σ).

Computational simulations. Simulation of *fs*PAGE was performed on COMSOL Multiphysics® v4.2a (COMSOL, Inc., Palo Alto, CA) with Transport of Diluted Species and Electric Currents 3D physics modules. Developed to assess non-uniformity of electric field lines, our model neglected thermal effects and employed two assumptions. First, evaporation during electrophoresis was neglected and the height of the *fs*PAG structures was assumed to remain constant. Second, temperature was assumed to remain constant. Run buffer (1X Tris-glycine) conductivity in aqueous solution was measured by B-173 Compact Conductivity Meter (Horiba Scientific, Kyoto, Japan). Run buffer conductivity in the *fs*PAG structures was estimated to be similar to that of PAG in glass microfluidic chips, as described by Duncombe et al.[89] The mobility and diffusivity of the model protein, TI, was estimated as per Herr & Singh[90] and Hughes et al.[91]. The voltage boundary conditions were set at each terminus of the *fs*PAG structure. For post-simulation data analysis, we averaged the protein concentrations over the transverse *fs*PAGE lane dimension at the 120 s time point to generate analyte concentration profiles, which were then analyzed in OriginPro 8.0 to calculate the bandwidths. In simulations, electric field strength was set to 60 V/cm.

3.3 Minimize separation dispersion with optimized sample injection

A schematic of high-throughput *fs*PAG-EMSA platform (96-plex) for screening riboswitch-ligand interactions is displayed in Figure 3.1. Unlike the electrophoretic separations in planar microfluidic devices that traditionally employ a t-channel configuration where sample loading and subsequent separation occur in each of the two orthogonal channels, in *fs*PAG, sample loading and injection are performed along a single spatial axis, in a manner similar to conventional slab PAGE. Therefore the quality of the electrophoretic separation is sensitive

not just to injection dispersion of analyte, but also to conditions in the sample well during the separation process (Figure 3.1).

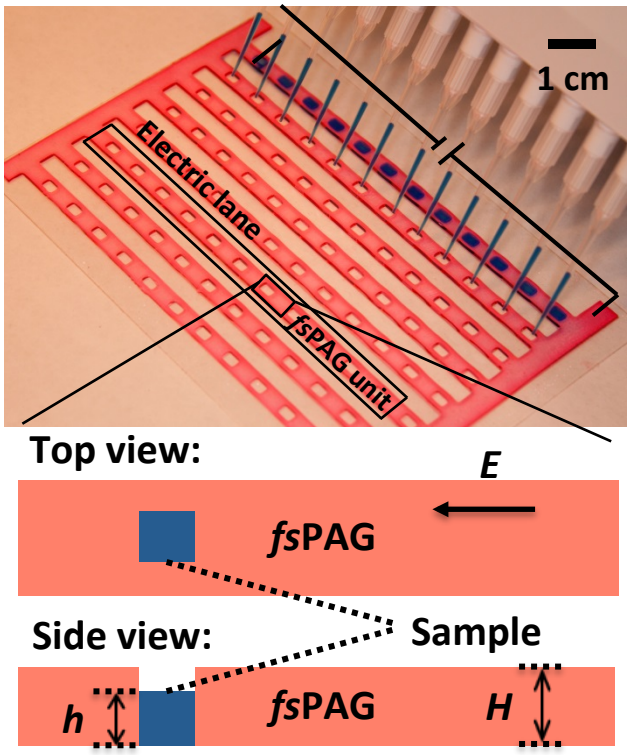

Figure 3.1 *fs*PAG design for microfluidic EMSAs. Image of a 96-plex *fs*PAG array. Sample wells are open rectangular regions. The PAG is dyed red to enhance contrast. A schematic of a single *fs*PAG unit is shown below. Sample well is embedded in the *fs*PAG. Gel structure and sample fluid heights are indicated by H and h. ([92]Reprinted with permission from Anal. Chem., 2014, 86 (20). High-Throughput Electrophoretic Mobility Shift Assays for Quantitative Analysis of Molecular Binding Reactions)

Given the open format and orientation of the *fs*PAG structures, sample is pipetted into the sample well from above. Depending on the volume of the sample well and the volume of the sample itself, the sample aliquot may not necessarily fill the entire well volume. Thus, to understand the sensitivity of separation performance on sample loading in this open sample well configuration, we simulated *fs*PAGE and the associated electric field strengths across a range of sample aliquot heights (h) relative to the *fs*PAG structure height (H) in COMSOL®. The standard convection-diffusion equation was used as governing equation (see equation 4 in chapter 1). In the simulation, protein concentration was set to 100 nM in the well and 0 nM elsewhere in the gel body as the initial conditions. Conductivity of 1X tris-glycine was used to set up the electric property of the gel. For all gel boundaries, no-flux conditions were applied. Though the simulation is performed for TI, the results of band shape and electric field also apply to a wide range of biomolecules including riboswitches. Electrical resistance of the sample well can be described by $R_w = \rho \cdot l_w/(w_w \cdot h)$, where ρ is sample resistivity, l_w and w_w are the axial length and width of the well. Consequently, reducing h would increase the resistance in the well, causing a greater voltage drop over the sample well region along the separation

axis (U_w) and, by Ohm's law, a reduced voltage drop over the gel region along the separation axis (U_g), as $U_w+U_g=U$ (applied voltage). As shown in Figure 3.2A, when $h/H \geq 0.4$, no notable transverse band skew or associated skew-induced axial dispersion was observed. Appreciable non-uniformities in the electric field distributions were also not evident. In contrast, when $h/H < 0.4$, skewing of the protein peak was observed as is the reduced migration distance. The $h/H < 0.4$ configuration essentially described a poorly filled sample well. Dispersion observed in the poorly filled well cases is attributed to high resistance and correspondingly high voltage drops across the sample well when limiting sample volume is present. Protein migration distance (Figure 3.2B) increased monotonically with increasing fractional fluid height in the well (h/H). Concomitantly, we observed a general trend of decrease in band width with increasing h/H. Consequently, we adopt sample well loading height in the $0.4 < h/H < 1.0$ range as a design rule for *fs*PAGE.

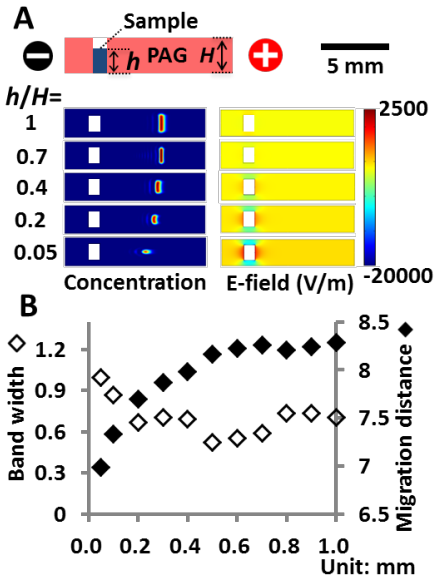

Figure 3.2 Minimize separation dispersion with optimized sample injection. (A) Simulation of *fs*PAGE of TI with different sample loading heights with COMSOL® tools. Axial well length=1mm E=60V/cm. B) Simulation results of bandwidth and migration distance for different h/H conditions. ([92]Reprinted with permission from Anal. Chem., 2014, 86 (20). High-Throughput Electrophoretic Mobility Shift Assays for Quantitative Analysis of Molecular Binding Reactions)

3.4 Thermal analysis of open *fs*PAG structures

For a given *fs*PAG structure, we consider Joule heating during electrophoresis. We can describe the heat balance by:

$$UI = A(\dot{q}_C + \dot{q}_E) \quad (1)$$

On the left hand side of equation 1, we see heat generation given by the product of the applied voltage (U) and the electrical current (I). The right hand side represents heat loss from convection $\dot{q}_C$ and evaporation $\dot{q}_E$, where A is the *fs*PAG structure surface area. Figure 3.3 illustrated the heat balance of *fs*PAGE. We can estimate A = lw and I = Us_gwH/l, where l is *fs*PAG structure length, w is the structure width, H is the structure height and σ_g is *fs*PAG conductivity. Given the large ratio (50-100) of the planar dimension (~1 cm) to the *fs*PAG height (~0.1 mm), we neglect heat dissipation from the sides of the gel structures. We can relate heat losses to operating conditions and the structure geometry:

$$\frac{U^2}{l^2}\sigma_g H = \dot{q}_C + \dot{q}_E \qquad (2)$$

Equation 2 states the sum of $\dot{q}_C$ and $\dot{q}_E$ increases with σ_g and H. According to Langmuir's evaporation model and the Antoine equation describing the temperature-vapor pressure relationship[93], both $\dot{q}_C$ and $\dot{q}_E$ increase with temperature. Therefore, increasing either s_g or H would result in both higher $\dot{q}_C$ and $\dot{q}_E$. In addition, the relative evaporative loss rate (fractional water loss in the gel body), also increases with H (See Appendix A). Dependences on geometry and thermal properties are directly relevant to riboswitch *fs*PAG-EMSA operation. Firstly, riboswitch binding to ligand depends on the local ions and their concentrations. As such, the TMBK buffer employed for riboswitch EMSAs is appreciably more conductive than typical gel electrophoresis buffers. For context, the TMBK buffer is ~7 times more conductive than tris-glycine buffer systems previously utilized in *fs*PAGE for protein analysis. Secondly, the open architecture of the *fs*PAG structures is susceptible to evaporative loss, leading to weak electrophoretic stability.

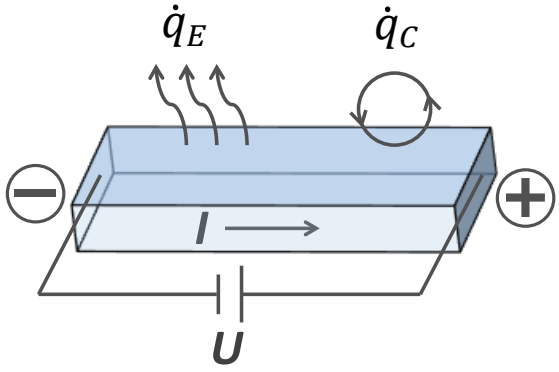

Figure 3.3 Schematics of heat balance in *fs*PAGE. Joule heating generates heat in the gel body, and two main sources of heat dissipation, heat convection $\dot{q}_C$ and evaporative heat loss $\dot{q}_E$, are shown in the graph.

To understand the as-of-yet unexplored influence of device geometry (H) on the thermal and electrical characteristics of *fs*PAGE-EMSAs, we monitored the relative current (normalized by initial current value) during *fs*PAGE for a range of H values (70 to 600 μm). For gels where H < 70 μm, both fabrication and sample loading were difficult, causing irreproducible

initial conditions so these *fs*PAG structures were not considered. For all structures studied, U was held fixed (E = 60 V/cm) and the TBMK run buffer contained 20% glycerol (glycerol helps to improve current stability and details can be found in a later section). As shown in Figure 3.4A, taller *fs*PAG structures (H ≥ 400 µm) exhibited an initial ramp up in current followed by a steep decrease in current after ~60 s of operation. The shorter *fs*PAG structures (H ≤ 200 µm) showed less dynamic behavior, but did exhibit a slow reduction of current during operation. Especially evident in the large structures, we attribute the initial current rise to an increase in gel temperature owing to Joule heating which, in turn, affects evaporation and ion concentration, leading to increased conductivity. In accordance, we attribute the observed subsequent sharp decrease in current to physical collapse of the gel structures owing to dehydration. Dehydration shrinks the porous gel matrix, thus reducing the conducting cross-section of the *fs*PAG lane. During the period when fluid is still present, the increasing resistance would reduce the current. Given these observations, we sought to minimize the rate of current drop to improve EMSA performance stability over an anticipated EMSA duration (Figure 3.4B). Using estimates from enclosed microchannel EMSAs of the c-di-GMP riboswitch (mobility shift of 2.5×10^{-6} $cm^2/V\cdot s$), a 3 min separation is anticipated to allow full resolution of the mobility shift between bound and unbound riboswitch (Figure 3.4B). At this 3 min time point, a *fs*PAG structure with H = 100 µm maintains ~90% of the initial current value, whereas the H = 600 µm structure maintains just ~40% of the initial current. Consequently, all subsequent EMSAs were conducted in *fs*PAG structures of 100 µm tall.

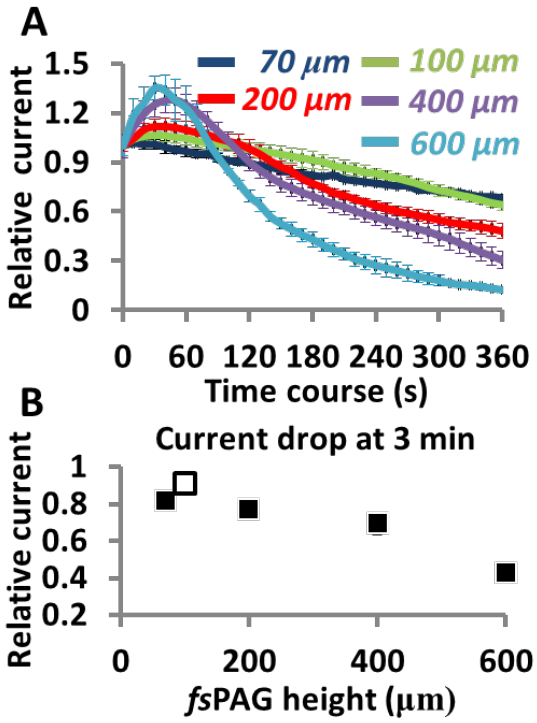

Figure 3.4 *fs*PAG geometry impacts current stability during electrophoresis. (A) Current stability over time during *fs*PAGE at E= 60 V/cm. *fs*PAG of 70-100 µm preserves most conductivity. (B) Current drop measurement for a range of *fs*PAG structure heights at 3 min. The highest relative current (white data point) is observed at 100 µm. ([92]Reprinted with

permission from Anal. Chem., 2014, 86 (20). High-Throughput Electrophoretic Mobility Shift Assays for Quantitative Analysis of Molecular Binding Reactions)

3.5 Improve the *fs*PAG thermal and structural stability

To improve the thermal and structural stability of the *fs*PAG device, we consider the addition of glycerol into the run buffer. Glycerol offers a lower vapor pressure and evaporation rate than water[94], thus we hypothesized that the addition of glycerol to the *fs*PAGE buffer should decrease the evaporative losses. However, the viscosity increase stemming from glycerol addition would also decrease analyte mobility and dispersion (via diffusion)[95, 96]. While glycerol was employed as a sample additive in our previous *fs*PAGE protein assays, we sought here to understand the influence of glycerol contents on thermal and electrophoretic characteristics of gel system, as well as the assay repeatability during *fs*PAGE-EMSAs in high conductivity buffers[87]. To determine a suitable glycerol concentration for *fs*PAG-EMSAs, we investigated the *fs*PAGE by monitoring the electrical current, structural integrity, analyte mobility, analyte bandwidth and resolving power of electrophoresis over a range of glycerol concentrations and electrophoresis times. In Figure 3.5A we monitored the electrical current in a 100 μm tall *fs*PAG every 10 s for a total 360 s of electrophoresis (60 V/cm). The *fs*PAGE run buffers contained varying glycerol concentrations from 0% to 30% (v/v). An immediate increase in relative current was observed during the first 30 s of electrophoresis followed by a monotonic decline in current over the remainder of the experiment. As expected, the additional glycerol concentration improved the electrical stability over the course of electrophoresis, as compared to systems with no glycerol present. Compared to a system with no glycerol, a system with 30% glycerol supported more than double the current after 6 min of operation (57.6% for 30% glycerol vs. 23.5% for no glycerol). We attribute the improved current stability of a glycerol containing system to the enhanced *fs*PAG structural integrity resulting from reduced evaporative loss.

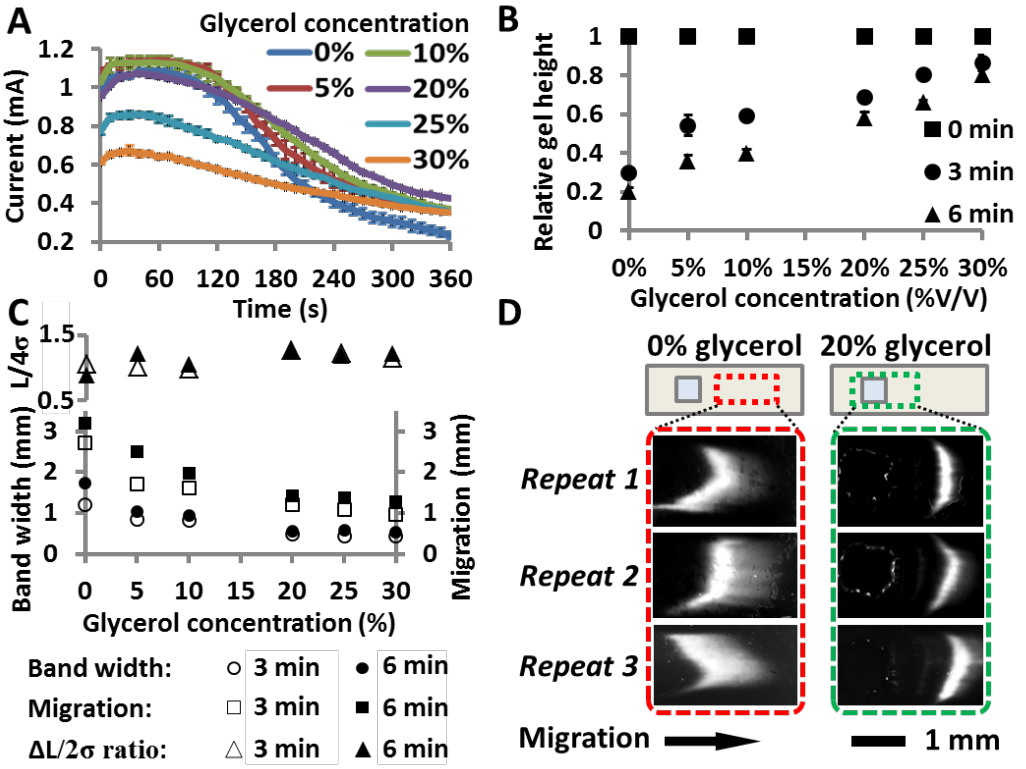

Figure 3.5 Glycerol addition improves *fs*PAGE operational stability. (A) Current dynamics of *fs*PAG structures with different glycerol concentrations. (B) Optical profilometry of gel height relative to initial structure height at set time points during *fs*PAGE. Initial height=100 µm. (C) Measurements of migration distance, bandwidth and their ratio at different glycerol concentrations during *fs*PAGE at 3 and 6 min. Protein: 500nM OVA. (D) Fluorescence images of protein band migration during *fs*PAGE for 0% and 20% glycerol at 3 min during separation. E=60 V/cm. *fs*PAG height=100 µm. ([92]Reprinted with permission from Anal. Chem., 2014, 86 (20). High-Throughput Electrophoretic Mobility Shift Assays for Quantitative Analysis of Molecular Binding Reactions)

To explore the impact of glycerol addition on electrical conductivity, we measured both the current and the height of *fs*PAG structures after 0, 3, and 6 min of electrophoresis run times for a range of glycerol concentrations. Addition of glycerol to the run buffer increases hydrodynamic resistance[95,96] and reduces ion mobilities. As detailed in Figure 3.5A, the initial current measured in a 30% glycerol device was 60% of the current measured in a *fs*PAG structure free of glycerol. We further noted that the addition of >25% glycerol to the *fs*PAG structures modulates electrical current stability over time (Figure 3.5A). Employing the *fs*PAG height as a proxy for the volume of solution retained in the *fs*PAG structure, we further observed that loss of *fs*PAG height during electrophoresis decreased with increasing glycerol concentration (Figure 3.5B). After 6 min of electrophoresis, the height reduction of *fs*PAG structures containing 30% glycerol was just ~20% lower than the initial structure height, whereas structures with no added glycerol saw height losses of > 80%. Based on these observations, we hypothesize that glycerol assists with maintaining *fs*PAG structural stability thus extending the effective electrophoresis time.

To evaluate the influence of enhanced viscosity (reducing mobility and diffusion) on the separation performance, we performed *fs*PAGE across a range of glycerol conditions on H = 100 μm tall structures with fluorescent scalar TI*. For the conditions studied, the resultant TI* migration distance (L) and bandwidth (4σ) are reported in Figure 3.5C. As anticipated, increasing glycerol concentrations reduced both the TI* migration distance and band width. To quantify the resolving power, we considered the ratio between migration distance and bandwidth (L/4σ) as an approximation for separation resolution in more complex samples. After 3 and 6 min of electrophoresis time, structures containing glycerol yielded notably higher resolving powers than structures containing no glycerol.

To assess device reliability, we compared the band shape over three separate trials in structures with 0 and 20% glycerol concentrations. Figure 3.5D shows resultant images after 3 min of electrophoresis time, with dramatic band distortion and variation observed in the replicates with no glycerol present. Unsuitable repeatability and bad band shape control were likely caused by rapid evaporation, giving rise to non-uniform gel drying which leads to heterogeneity in analyte mobility across the gel. In contrast, structures containing higher glycerol concentrations (20%) yielded a consistent band with notably less transverse skew. Thus, run buffer containing 20% glycerol provided performance suitable for 3 to 6 minute separations at (60 V/cm) in *fs*PAG-EMSA current stability, separation performance, and reliability.

3.6 Separation uniformity on scaled-up *fs*PAG assay

To realize a high-throughput EMSA platform, we fabricated a 96-plex 20%T *fs*PAG array measuring 60 mm x 70 mm (Figure 3.6). The array is comprised of 8 parallel *fs*PAG lanes, each housing 12 separation units in series with a 4.5 mm unit-to-unit distance. To electrically address the array, graphite electrodes were placed atop electrode wicks orthogonal to each *fs*PAG lane and ~2 mm away from the first and last separation unit in each lane. In previous work, we observed significant unit-to-unit variation in analyte migration distance on large *fs*PAG arrays, especially in units on the periphery of the device.[87] To understand and address migration variation, we measured the migration distance of a scalar (fluorescently labeled 500 nM OVA*) at a set time and tested significance of unit-to-unit variation with an ANOVA test (See Figure 3.6A and Appendix B for details). In particular, we sought to assess the spatial variation in migration distance between peripheral groups and the central region (groups assigned in Figure 3.6A). For each peripheral group, ANOVA was performed to analyze its variation against the central region group a, where no spatial variation is present. In the present ANOVA study with 96-plex *fs*PAGE, the $F_{critical}$ value is 4.00 (α=0.05), meaning any calculated F value greater than 4.00 indicates significant difference in migration distance. For *fs*PAG lanes at the top and bottom of the array, no significant variation in migration distance was observed as compared to migration distances observed in the central array region (F values 0.14 and 0.70, respectively). In contrast, regions adjacent to the electrodes showed significant variation in scalar migration distance. As compared to the central region of the array, the 1st and 2nd columns adjacent to the cathode electrode supported a higher scalar

velocity (F values 438 and 121, respectively) and the 12th column directly adjacent to anode supported a lower scalar velocity (F value 205). We hypothesized that electrolysis during electrophoresis altered the pH proximal to each electrode. At the cathode, electrolysis should generate excess OH^- ions and elevate the local pH causing proteins to increases in negative charge and mobility. Conversely the anode would see generation of excess H^+ ions and lower the local pH, thus reducing protein charge and mobility.

While there were several possible approaches to address pH polarization – including increasing buffering capacity or implementing buffer reservoirs – we opted to simply redesign the electrode region of the 96-plex *fs*PAG array to offset the graphite electrodes from the first and last separation columns. The modified electrode regions increased the array area from 4200 mm^2 to 7000 mm^2. With the o*ffs*et electrode placement (Figure 3.6B), ANOVA reported no significant region-to-region variation in migration distance for the scalar (F=1.67, 2.21 and 0.05 for columns 1, 2 and 12, respectively).

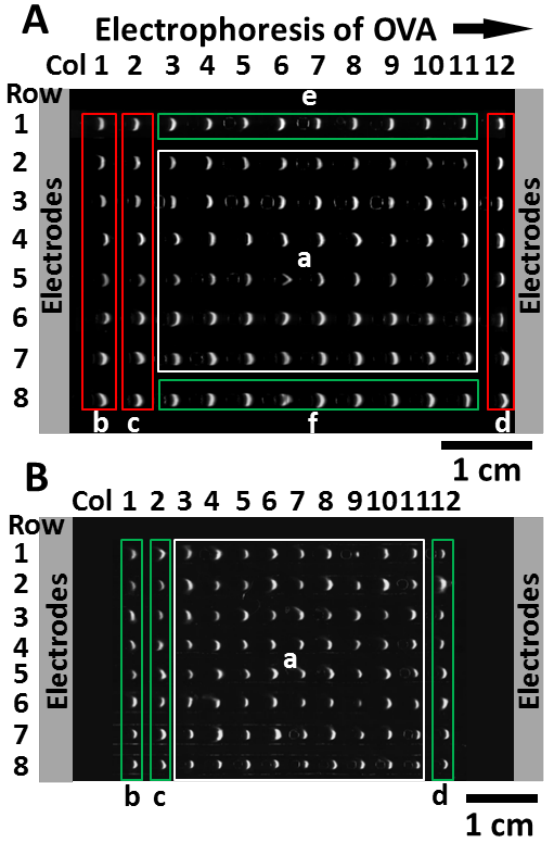

Figure 3.6 Unit-to-unit variation of migration distance on the 96-plex *fs*PAGE. (A) Fluorescence imaging of 96 concurrent OVA *fs*PAGE. A gel defect was detected in Row 5, Col 6, resulting in a "band bowing" on this unit (excluded from calculations). 96 units were grouped into regions. Central region group: a; Other peripheral groups: b-f. F value for migration distance: a-b: 438; a-c: 121; a-d: 205; a-e: 0.14; a-f: 0.7. Significant variations were observed for a-b, a-c and a-d (squared in red). No significant variations were observed for other groups (squared in green), α=0.05. (B) Optimized *fs*PAG design with o*ffs*et between

electrodes and *fs*PAG units. Central region group: a; peripheral groups: b-d. F values: a-b: 1.67; a-c: 2.21; a-d: 0.05; No significant variations were observed (squared in green), α=0.05. $F_{critical}$=4.00 for ANOVA on 96-plex *fs*PAG. ([92]Reprinted with permission from Anal. Chem., 2014, 86 (20). High-Throughput Electrophoretic Mobility Shift Assays for Quantitative Analysis of Molecular Binding Reactions)

3.7 *fs*PAG EMSA for Cyclic-di-GMP riboswitch

Having established the optimized *fs*PAG conditions, the 96-plex *fs*PAG-EMSAs were applied in high-throughput detection of binding of the Vc2 aptamer to c-di-GMP. Based on previous in-chip EMSAs as well as previously characterized Vc2 binding rates[97], the expected inter-conversion rate between bound and unbound RNA is slower than the rate of electromigration, indicating that the EMSAs will resolve the binding-induced conformation change into two distinct bands. The separate bands visualized in the slow inter-conversion regime allow for the K_d or a standard curve of the system to be calculated by the relative intensity of each peak[98].

To analyze ligand binding to the Vc2 aptamer, we constructed a 96-plex 20%T *fs*PAG for high-throughput riboswitch *fs*PAG-EMSAs (Figure 3.7A). The array has 9 mm horizontal well-to-well spacing and 9 mm lane-to-lane distance such that a standard multi-channel pipette provides a suitable macro-to-micro interface. The binding reactions contained 1 μM RNA and 0-900 nM c-di-GMP using 500 nM of TI* as an internal standard. Based on the high affinity of the Vc2 aptamer for c-di-GMP (K_D ~ 11 pM)[97], the high RNA concentration used here results in the generation of a standard curve rather than a K_d curve, which would require the concentration of one reagent to be below the K_d. Electrophoresis was performed for 2.5 min followed by fluorescence scanning of the array. The observed mobility shifts demonstrate the successful application of 96 parallel EMSAs in < 3 min (Figure 3.7A). The ligand bound and unbound riboswitch were resolved within half the axial length of a unit, leaving room for further improvement in array density. Figure 3.7B reports the time evolution of the separation resolution between the unbound Vc2 aptamer and the c-di-GMP-bound RNA, where the SR exceeds 0.5 from 2 min.

As shown in Figure 3.7C, the fluorescence intensity of the bound RNA band increased as the c-di-GMP concentration in the sample increased linearly (R^2=0.9893). Note that, for each concentration point, 12 repeats were averaged to improve the assay precision, yielding a standard error of less than 0.07 for all concentrations. The *fs*PAG-EMSA of 96 units in 10 min (5-6 min of setup and loading + 3 min separation) yielded a throughput of ~10 data/min as compared to ~0.3 data/min[7] for serially loaded, in-chip microfluidic EMSAs and ~0.01 data/min[7] for slab PAGE-based EMSAs (17 hours for 10 lanes).

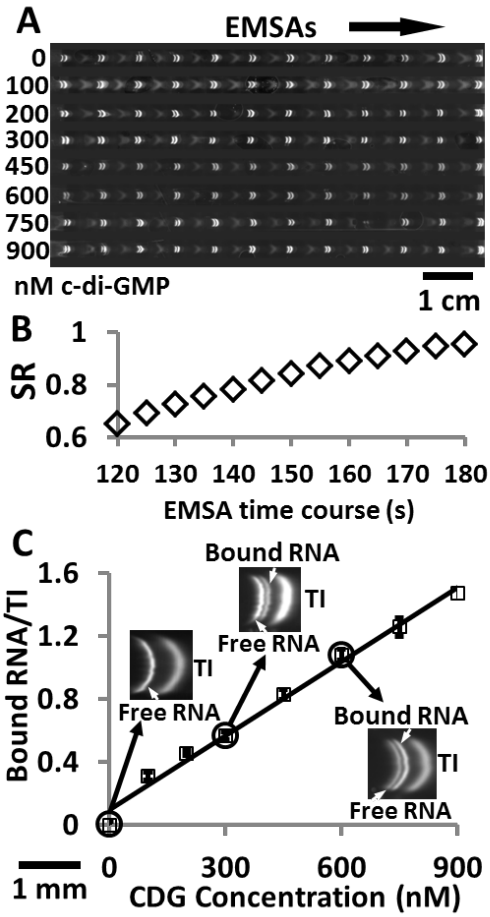

Figure 3.7 High-throughput *fs*PAG-EMSAs riboswitch. (A) Fluorescence images of c-di-GMP riboswitch EMSAs on a 96-plex *fs*PAG. Vc2 RNA (1 μM) was incubated with increasing concentrations of c-di-GMP (0-900 nM) and the binding reactions were assayed using TI* (500 nM) as the internal standard. The arrow points E-field direction. (B) SR monitoring showed mobility shift was resolvable at 2 min. (C) Normalized intensity of bound RNA increases with c-di-GMP concentration (R^2=0.9893). Insets zooms in the fluorescence micrographs of RNA separation. ([92]Reprinted with permission from Anal. Chem., 2014, 86 (20). High-Throughput Electrophoretic Mobility Shift Assays for Quantitative Analysis of Molecular Binding Reactions)

3.8 Conclusion

To afford a capacity for concurrent operation of electrophoretic mobility shift assays, we explored *fs*PAG structures seated on an open planar polymer substrate. The open architecture allows for ready pipetting of macro-scale sample into microfluidic sample wells, as well as compatibility with post-separation sample manipulation. To adapt the *fs*PAG for riboswitch EMSAs in high conductivity run buffers, we studied three major design aspects of the device, including: (i) the dependence of EMSAs performance on sample well electrical properties

(40%-100% loading of sample well maximize SR), (ii) the interplay between the *fs*PAG structure geometry and run buffer recipe, with the time dependent electrical properties of the system (100 μm *fs*PAG in 1X TBMK containing 20% glycerol yields highest electrical stability), and (iii) the unit-to-unit variation across the large-format *fs*PAG array and strategies for mitigation of variability (2 cm away from electrodes). Going forward, we believe the *fs*PAG-EMSAs assay need to improve in the following 2 aspects. First, the present platform shows poor performance for electrophoresis times > 3 min. For assays that require substantially longer separation times (> 5 min), a semi-enclosed *fs*PAG structure will be more suitable, which retains the facile open format while potentially providing longer separation duration. Additionally, the cumbersome manual loading process significantly limits the overall throughput of the assay (~5 min loading out of 10 min total assay). Automation of *fs*PAGE loading with robotic sample loading systems (< 2 min loading) will likely further advance the screening capacity and impact of quantitative, precision EMSAs. For instance, the integration of *fs*PAGE with acoustic liquid handler is detailed in Chapter 4.

A pilot study of 96-plex *fs*PAG-EMSAs for Vc2 c-di-GMP riboswitch aptamer binding reactions were demonstrated with linearity observed in a ligand concentration titration study. We envision that the improved detection sensitivity of the assay will allow K_D measurement for high-affinity interaction (K_D < 1 nM), and future studies will seek to harness the open gel structure to perform post-separation staining and signal amplification, further improving the detection sensitivity. Taken together, the streamlined yet powerful *fs*PAG-EMSAs offer a promising platform for rapid binding reaction analyses, and support molecular binding screening assay in a quantitative, high-throughput and reliable manner.

Chapter 4 Enhance the analytical precision and throughput of *fs*PAGE with acoustic droplet ejection (ADE)

4.1 Challenges of high-throughput sample delivery on *fs*PAGE and introduction to existing liquid transfer system

The development of high-throughput free-standing polyacrylamide gel electrophoresis (*fs*PAGE) platform has greatly benefited the quantitative analysis of molecular binding reactions with enhanced specificity/sensitivity and reduced laboratory infrastructure. In brief, *fs*PAGE has the following advantages over conventional electrophoretic tools.

- Simple fabrication. The *fs*PAG is manufactured with either photo-patterning or micro-molding that are easily affordable by conventional office color printer and low-end laser cutter, enabling rapid prototyping of gel design iteration.
- Low device infrastructure and easy integration with standard laboratory equipment. *fs*PAGE is performed within customizable electrophoresis chambers that can be easily designed and manufactured on a standard 3D printer[87,92].
- Scaled-up analysis. *fs*PAG can be adapted into microarray structure to house 96 or 384 concurrent separation units, gaining broad relevance in high-throughput screening application of a variety of biological substances.
- Easily controllable spatial modulation of the gel structure enables advanced electrophoretic analysis. Our group has demonstrated gradient *fs*PAG that showed enhanced separation resolution with reduced device footprint.[99]
- The open format *fs*PAGE allows post-separation analytes accessibility. Such feature potentiates direct western blotting analysis with diffusive antibody probing after separation.

Despite the advantages, sample loading on multiplexing *fs*PAGE remained a challenging task, especially for devices with higher separation unit density. The difficult sample loading has limited the *fs*PAGE for high-throughput analysis in two aspects: (1) Time-consuming and inconsistent sample loading. A typical manual sample loading with pipette on 384-plex *fs*PAG takes roughly 20 min. Additionally, the non-ergonomic liquid handling adds to the inconsistency of delivered sample volume in each well, lowering the uniformity of the assay. (2) Evaporation of loaded sample occurs during the sample delivery process. According to evaporation model[100], remarkable size reduction is observed for millimeter-sized droplets in the quiescent air with in tens of minutes. With liquid evaporation, the differential sample volume between early and later loaded wells further reduce the unit-to-unit repeatability.

Therefore, we sought to establish a reliable, robust and easy-to-perform sample delivery strategy for high-throughput *fs*PAGE. To achieve this goal, we considered following approaches: (1) Multi pipette. (2) Manual pin tools that can be installed on the commercial automatic liquid handler. (3) Acoustic liquid delivery.

Multi pipette, or multi-channel pipette, was designed to match the industry standard microplate dimension, and can be used for *fs*PAGE sample delivery. However, there are several limitations with this approach. First, the *fs*PAG wells are of similar size of pipette tips, making the gel easily prone to accidental damage. Second, the difficulty in manual alignment adds to complexity of operation that requires lengthy user training and practice. Third, low sample delivery (50-400 nL) often incurs high level of volume inaccuracy, decreasing the uniformity of the parallel analysis. In summary, we conclude that multi pipet is not an appropriate way for sample delivery on gel.

Pin tools are another possible sample delivery solutions for *fs*PAGE, as they are designed to transfer low volume of samples. Pin tools delivery is a way of contact dispensing originally used in other application such as clinical testing and later was adapted for micro-high-throughput screening (μHTS) because of its simplicity and reliability.[101] However, earlier pin tools had a reputation for low accuracy.[102] Generally, the amount of volume being transferred is dependent on the surface tension between the source liquid and pin materials, as well as the geometry of the contact surface. In the recent decades, optimization has been made to improve the delivery accuracy, including cutting a precise nano-slot on the tip of the pin and surface treatment with hydrophobic/lipophobic coating (HLC).[103] Commercial pin tools come in a variety of form factors, including 24, 48, 96, 384 and 1536 pins. The floating design of the pin tools allows "soft pin tips landing" on the destination surface, eliminating the possibility of hard touch that would break device.

Pin tools enabled *fs*PAG sample transfer was illustrated in Figure 4.1. Figure 4.1A shows the alignment of a rack of 96 pin tools with *fs*PAG device. The pin used here has a set delivery volume of 25 nL, and multiple (4) transfer cycle is required to fully fill the well (100 nL in volume). Between each cycle, the pins will go through a set of washing procedures with cleaning solution (proprietary by vendor), distilled water and alcohol, as shown in Figure 4.1B. Figure 4.1C and 4.1D illustrated the liquid transfer onto 96-plex and 384-plex *fs*PAG using blue ink doped water as a demonstration. Two observations were made regarding the sample delivery.

1) Volume variation. Quantitative volume analysis can be performed with electrophoretic tools, which is detailed in the following sections, while a visual comparison of the delivered sample volume in the two square red windows has sufficiently illustrated the volume variation. The volume variation stems from contact force between pin tips and the well surface, which determines the "unloaded" volume from the tip of the pin to the substrate. The floating structure of the rack of pins combined with the limited flatness of the *fs*PAG device were putting inconsistent contact degree between tip of the pin and the target substrate, resulting in a high degree of variation in sample loading.

2) Location inaccuracy. The floating structure of the pin tools rack could induce horizontal deviation of pin tools during landing. As a result, the sample droplet unloaded from the tip of the pin does not always settle in the well. To quantify such deviation, we evaluated the overlap between the delivered sample droplet and area of the well and classified the delivery into 3 levels. Fully filled: the entire sample drop stays in the well; Partially filled: 0-100% of

the droplet overlapped with well; Fully offset: the entire sample drop lay out of the well. (See Figure 4.1E for details) Using this criteria, Figure 4.1F counted the number of wells in each class. Out of 384 wells, only 71 wells were fully filled. For the rest 313 wells, 305 wells are partially filled and 8 wells were fully offset. From the delivery results, it is clear that less than 20% of the wells were fully filled with sample solutions. Though further replicates were necessary to confirm and verify the quantitative delivery performance, we determined such pin tools were highly unreliable for conducting robust liquid transfer on gel. Therefore we decided not to proceed along this direction for our study.

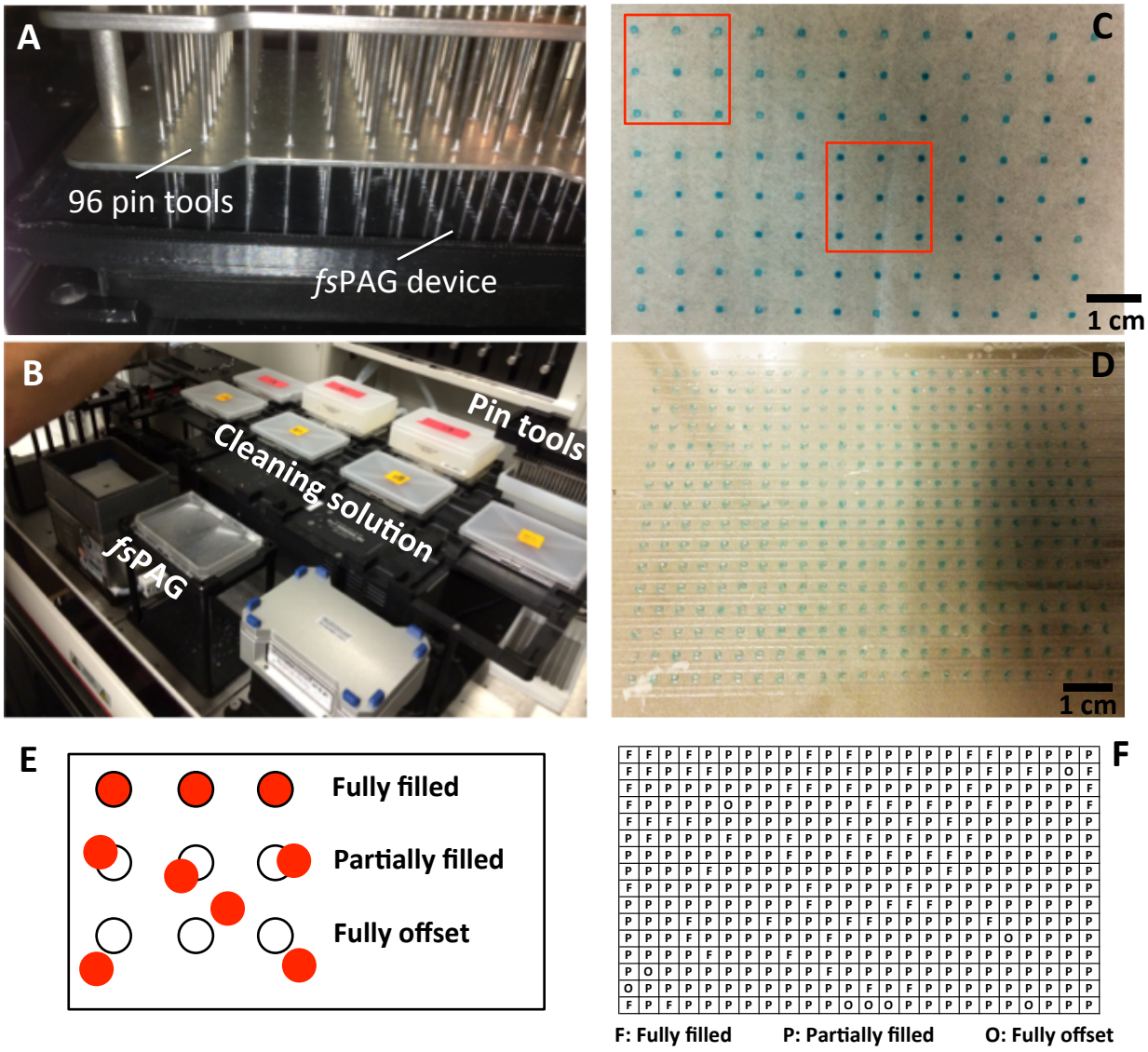

Figure 4.1 Sample transfers with pin tools on *fs*PAG. (A) Alignment of a 96 pin tools rack with *fs*PAG device. (B) A schematic of entire transfer stage. Between each transfer cycle, the pin tools go through serial tip washing in cleaning solution. (C) Transfer result of blue ink doped water on 96-plex *fs*PAG. (D) Transfer result of blue ink doped water on 384-plex

*fs*PAG. (E) Criteria for classifying sample delivery into the three categories: fully filled (F), partially filled (P) and fully offset (O). (F) Classification of each sample deliveries in well in D according to the standard in E.

Acoustic droplet ejection (ADE) is a commercialized non-contact liquid transfer technology that has seen dramatic growth in the low volume liquid handling market in the recent years. ADE, or acoustic liquid handing, uses high-frequency ultrasound energy to focus the excitation energy near the surface of the liquid to generate small droplets and eject them towards destination plates. ADE was pioneered in the early 1920s. A high-energy acoustic source was placed in oil and the resulting oil surface behaved like "erupting oil droplets like a miniature volcano".[104] Later, as researchers gather deeper understanding of the ultrasound, ADE technology has developed and people were able to precisely control the frequency of sound wave and focus the energy on the surface to quantitatively modulate the generation of droplets with predefined size and ejection speed.[105,106] ADE has several advantages over conventional contact liquid transfer approach: 1) Fast sample delivery. Droplets generation and dispense occur in ~10^2 Hz. 2) Eliminate sample cross-contamination. Since ADE is a non-touch liquid handling technique, there is no concern about mixing or contaminating samples from source plate. 3) Save material costs. No solid (pipette, pin tools) is involved in ADE that saves costs on these consumables/materials. 4) Easy/simple parameters control. Unlike pin tools where the accuracy of the transferred volume depends on a variety of factors, one could simply adjust the droplets size/uniformity by modulating the excitation frequency, power and wave pattern of the ultrasound.

Considering the small well size, thin structure and gel fragility of the *fs*PAGE device, ADE could serve a promising and powerful tool for high-throughput and robust liquid transfer (Figure 4.2). In this chapter, we detailed study of ADE based technology——Labcyte Echo® 525 liquid handler (Echo) to perform small volume liquid transfer on gel.

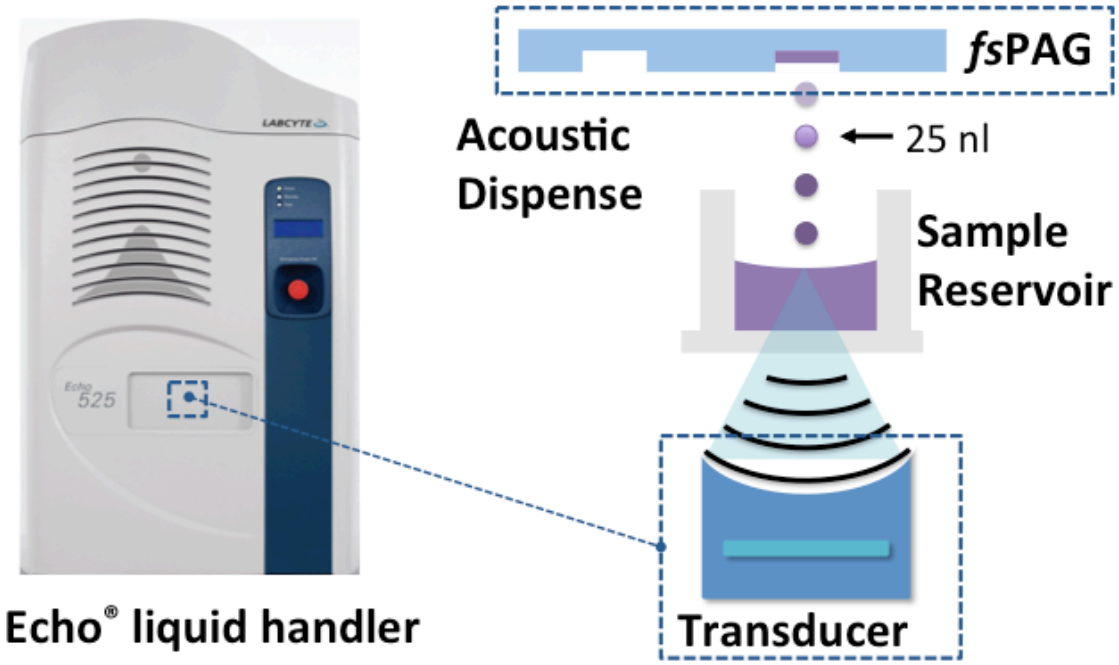

Figure 4.2 A schematic of integration of ADE with *fs*PAG on Echo liquid hander. Ultrasonic transducer was installed at the center of Echo and excited by analog signal to generate ultrasound. The acoustic energy is focused at the surface of the sample liquid and each ultrasound pulse ejects 25 nL of droplet from the sample reservoir to the destination *fs*PAG device.

4.2 Materials and Methods

Reagents: Sample buffer for alignment test was made by diluting 10X tris-glycine (Sigma Aldrich, St. Louis, MO) in water doped with red food dye (McCormick, Sparks, MD) to a final concentration of 1X. 0.2% of bovine serum albumin (BSA) was added to sample buffer to match the components of antibody binding reaction solution described in Chapter 5. Protein ladder used in uniformity test was made by diluting Alex fluor 555-labeled BSA (BSA*) and Alex fluor 555-labeled ovalbumin (OVA*) in 1X sample buffer (excluding red dye) to yield a final concentration of 50 nM for each.

***fs*PAG micro-mold fabrication:** *fs*PAG was fabricated with micro-molding. Micro-molding provides an easy way to fabricate open polyacrylamide gel structure, and it addresses the over-polymerization problem commonly seen with photo-polymerization described in chapter 3. Traditionally, micro-molds were manufactured by SU-8 based soft lithography[40], however, this approach is slow and requires clean room equipment and heavy infrastructure. We therefore developed a novel approach for fast and simple fabrication of micro-molds. The new method uses laser cutter (Full Spectrum laser model HL40-5G-110, Las Vegas, NV) to selectively pattern *fs*PAG structure on Kapton® tape (Kapton) on silicon wafer as the substrate. This approach was proved to be effective in fabricating meso-scale *fs*PAG structure with gel height ranging from 50-500 μm. The protocol involves several steps. First, rinse the surface of

silicon wafer with methanol, Isopropyl alcohol (IPA) and water for 2 times. Then, carefully attach a layer of 1 mil thick Kapton tape on the cleaned surface of the silicon wafer. Use a flat roller to get rid of as many air bubbles strapped between the Kapton layer and silicon wafer as possible. Place the silicon wafer on the platform in the laser cutter. Tape the wafer to secure its position. Turn on the laser cutter and open RetinaEngrave3D on the connecting PC. Import the design file into RetinaEngrave3D. To ensure the laser track is recognized by the system as "linear structure" with no width, change the line width of design file to 0.00025 point in the CAD software before loading it onto RetinaEngrave3D. For a 1 mil thick Kapton layer, set the cutting parameters: Speed = 80, Power = 0.3, Path = 2. Close the lid of the laser cutter and start the cutting. When the cutting completes, clean the ashes in the laser track with water rinsed Kimwipe. Carefully hold the silicon wafer in place because a second cut will resume on the same location and this ensures the second cut will precisely land on the first laser track. Next, perform a second round of cut, followed by ash cleaning. Repeat the "cut-clean" cycle for 3 times. At this point, the 1 mil thick Kapton is fully cut through. Take out the silicon wafer. Peal off the Kapton along the laser track. The mold should be ready for use. For thicker *fs*PAG micro-mold structure, multiple layers of Kaptons can be stacked together. It is suggested to pattern one layer at a time, that is, to stack multiple micro-mold together rather than cutting through multiple layers. It is difficult to cut through multiple layers at one time.

***fs*PAG micro-molding:** The 10%T, 3.3%C *fs*PAG structure used in this study was made via *fs*PAG micro-molding. The PAG precursor solution contained 10%T acrylamide (w/v), 3.3%C bis-acrylamide crosslinker (w/w) and 1% VA-086 photo-initiator (w/v). The precursor solution was then degassed for 2-3 min under house vacuum with sonication and carefully poured over the micro-mold on silicon wafer. The surface-functionalized polymer sheet (Gelbond®) was capped over the precursor solution and pressed down against the surface of the micro-mold. Excess precursor solution was removed with Kimwipe. Carefully place the Gelbond® to ensure no air bubbles were trapped in the molds. Flipped the molding infrastructure and placed in the UV exposure system (OAI model 30 collimated UV light source, San Jose, CA) for UV photo-polymerization. For 10%T 3.3%C PAGs, 40 s exposure at 20 mW/cm^2 (measured by OAI 308 UV intensity meter, OAI, San Jose, CA) was employed. After UV exposure, the *fs*PAG was patterned on the Gelbond® ready for use. The *fs*PAG device can be stored in water or buffer for long-term use.

Echo operation: The Labcyte Echo® 525 liquid handler was used to perform ADE from source plate to destination. In selecting the source plate, 6-reservoir well plate (6-res) was used in uniformity measurement and distance study. *fs*PAG was mounted onto a standard 384 well plate with "2-step registration strategy" described in Section 4.3 and inserted into Echo for transfer. The transfer was programed and performed with in-house build Echo Plate Reformat software provided by Labcyte Inc.

Electrophoretic variation measurement and distance optimization: Protein ladder spiked solution was transferred onto *fs*PAG in Echo and electrophoresis was conducted in electrophoresis chamber at 50 V/cm for 75 seconds. The gel was then placed in nitrogen airflow for 5 min until the structure was fully dried, followed by fluorescence imaging on microscope described in Chapter 3. To quantify the uniformity of peak intensity in

electrophoresis, fluorescent intensity profile in each separation unit was generated by averaging the intensity values in the transverse direction along the separation lane. A custom written Matlab code calculated the peak intensity (area-under-curve) and read out the variation. To optimize the distance for ADE transfer, band intensity variation was measured over a range of gel-source plate distance of 0.5, 1, 1.5 and 2.5 mm.

4.3 Integration strategy for *fs*PAG and Labcyte Echo® liquid handler

As an instrument originally designed to handle standard microplates, the Echo system does not directly work with *fs*PAG. Therefore, the development of a robust and precise gel-Echo integration strategy is essential to guarantee the location precision of liquid transfer and electrophoresis performance. To convert the *fs*PAG into a "working block" compatible with Echo, we developed a "2-step registration" protocol to precisely mount the *fs*PAG device onto the microplate, which is then inserted to Echo for ADE transfer. The strategy is schematically shown in Figure 4.3. Briefly, the *fs*PAG card is aligned onto a substrate microplate with pre-printed target grid. Firstly, the target grid is printed on a transparent microplate sealing film attached on the top surface of a 384-well plate using a red food dye spiked water solution (see Figure 4.3 step 1 and 2). In this way, the target grid precisely mapped out the locations of droplet landing, which is a system-specific property that varies from machine-to-machine. Then, the red dots were labeled with permanent marker pen to register the location information for long-term use. Next, the *fs*PAG were aligned onto the sealing firm with sample well overlapping the target grid. In the last step, the gel-plate structure was flipped and inserted to Echo for liquid transfer. Using this strategy, droplets from ADE dispense would land exactly in the sample well with geometrical precision. Here, we call the target grid printing the first registration and gel-grid-plate alignment the second registration.

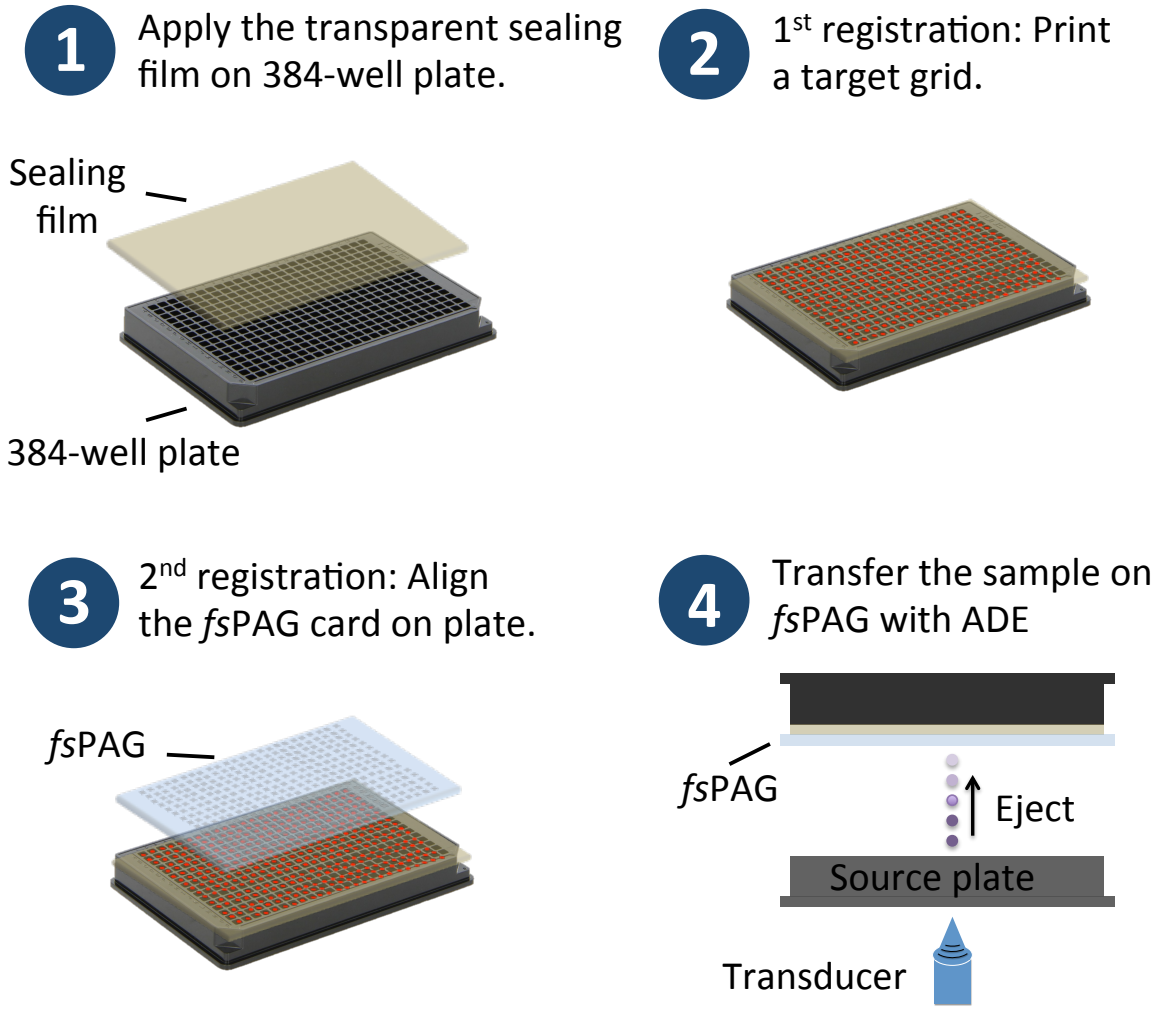

Figure 4.3 "2-step registration" strategy to integrate the *fs*PAG onto Echo. Step 1: A transparent sealing firm is attached on the surface of the 384-well micro plate. Step 2: Target grid was printed on the sealing firm on Echo. Step 3: Place the *fs*PAG device by aligning the sample well to the target grid. Step 4: Flip the device and set up on Echo for ADE sample delivery.

The use of "2-step registration" aligning strategy greatly improved the delivery location accuracy. Figure 4.4 compared the sample solution delivery patterns by ADE and pin tools. With the novel aligning method, we achieved 100% fully filled sample wells in liquid transfer, and such results were repeatable across 3 replicates. Compared to the delivering results using pin tools that yields <20% fully filled well, the ADE powered *fs*PAG loading significantly improved the loading quality and saved processing time (3 min vs 20 min).

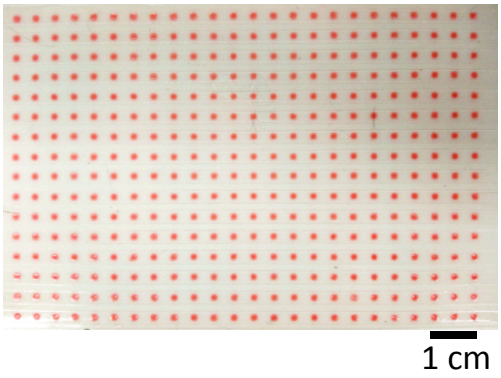

	ADE (n=3)	Pin tools
Fully-filled	384	71
Partially-filled	0	305
Fully-offset	0	8

Figure 4.4 Location accuracy of ADE-*fs*PAG sample loading and comparison with pin tools. Left, sample delivered by ADE achieved 100% fully filled sample well. Right, comparison of location accuracy of ADE and pin tools. In pin tools powered *fs*PAGE, only <20% of the wells were fully filled.

The above comparison clearly verified the "2-step registration" strategy as a robust and reliable method for fast small volume liquid transfer on gel.

4.4 Benefits of ADE-driven *fs*PAGE analysis

Following the location accuracy achieved with "2-step registration" strategy, this section will detail the volume uniformity and electrophoretic performance in *fs*PAGE. In electrophoretic analysis, peak intensity of the analyte directly reflects the concentration of each component in the sample solution, and is quantified by taking the area-under-curve (AUC) value of analyte bands. To precisely reflect the concentration information in the analyte solution and enable comparability in sample wells, it is desired to have a uniform "intensity response", that is, minimal intensity value difference across all separation units for nominally same amount of "input" sample solution. Such electrophoretic property can be determined by quantifying the peak intensity uniformity in each unit when all the separation units were assayed with the same analyte solution. To ensure the comparability in sample wells, it is important to verify the uniformity of the peak intensity. In a 384-plex *fs*PAGE, the collective uniformity of peak intensity in separation units is determined from two components: sample volume uniformity and intrinsic variation of the multiplexed *fs*PAGE. The intrinsic variation of multiplexed *fs*PAGE further comes from two sources: 1) Not all dispensed droplets go in to the gel, partial bouncing of droplets to the surrounding gel and incomplete droplet merging reduces the amount of analytes migrate into the gel. 2) Physical intrinsic variation in *fs*PAG units. The differences in well size and shape all increase the non-uniformity of peak intensity.

The labcyte ADE technology ensures <5% CV in delivered sample volume across 384 units. Combining the intrinsic unit-to-unit variation, the uniformity in peak intensity reflected the systematic uniformity of the new assay. To quantify the value, we performed an OVA*-BSA* ladder separation and extracted the AUC of the BSA* band in each unit. We than averaged the BSA* intensity across 384 units and calculated the CV value. We used the BSA* intensity CV

to represent the peak intensity uniformity of the system. The lower the CV, the better the uniformity.

We dispensed 100 nL of protein ladder sample solution into the *fs*PAG wells and quantified the peak intensity uniformity in Figure 4.6. The left graph Figure 4.6A showed fluorescent image of the protein ladder separation. A zoom-in micrograph showing separations in 3 horizontally consecutive units were laid below the 384-plex image. As a comparison, same protein ladder separations with manual sample loading were shown to the right. In Figure 4.6B, we measured the intensities of BSA* in each separation unit and listed data in the matrix in Figure 4.6B. We further plotted the intensity values of each separation unit in the graph to the right of the data matrix. Similarly, we performed the same analysis with *fs*PAG of manual sample loading in Figure 4.6C. Figure 4.6D plots the peak intensity CV for the two sample delivery modes (n=3). 75% reduction in the peak intensity CV was observed when acoustic liquid transfer was performed. Both the visual comparison and quantitative data have shown remarkable improvements in the unit-to-unit uniformity of peak intensity in ADE sample transfer. Additionally, ADE transfer saved more than 80% sample loading time, further improving the analytical throughput.

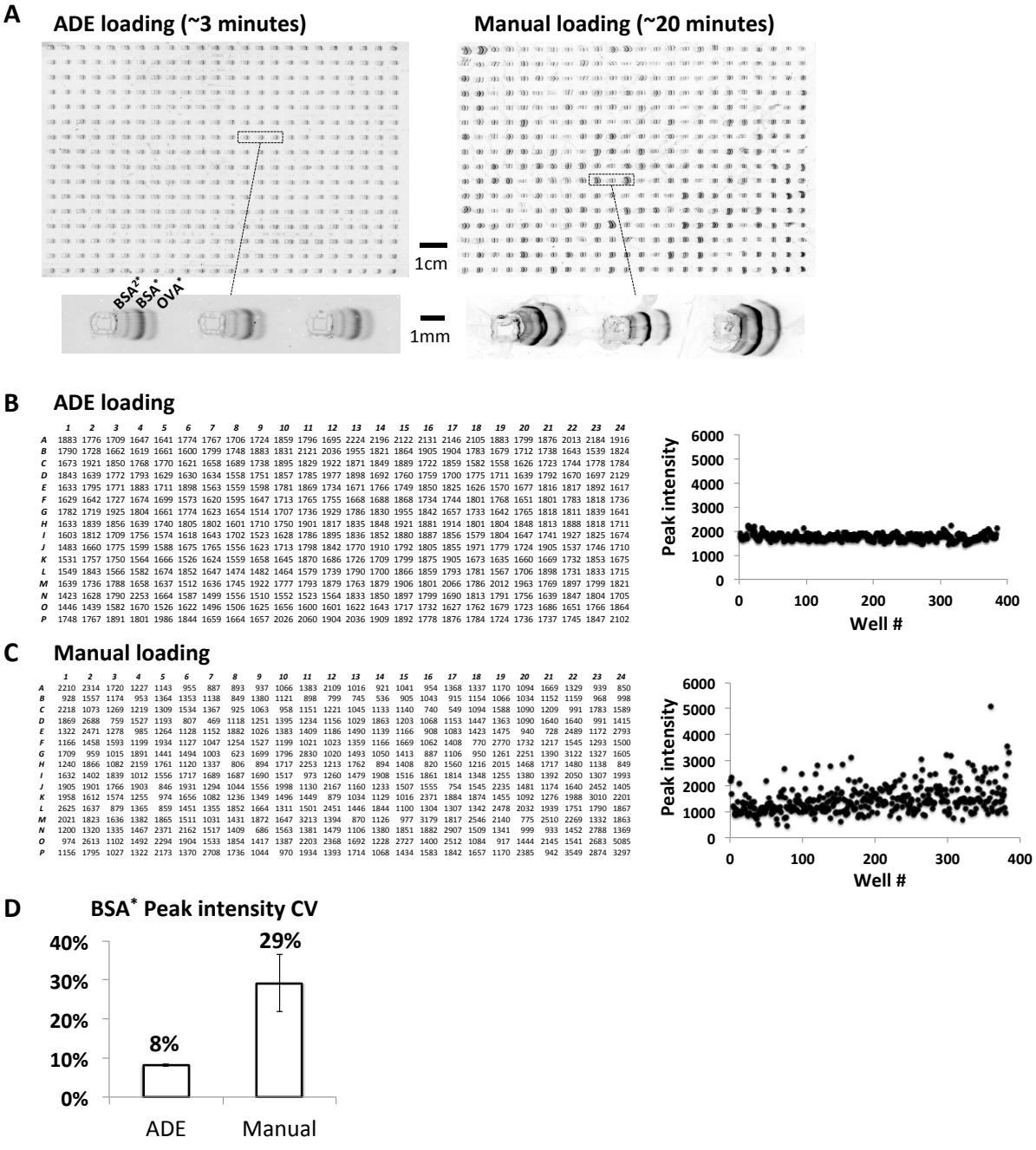

Figure 4.5 Comparison between ADE and manually loaded *fs*PAGE. (A) Fluorescent image of protein ladder separation comparison between ADE and manually loaded *fs*PAGE. Zoom-in pictures were shown below the 384-plex images. A dimer of BSA* was observed in separation. (B) For ADE loaded fsPAGE, the peak intensities of BSA* were measured in each separation unit and plotted in one diagram. (C) For manually loaded fsPAGE, the peak intensities of BSA* were measured in each separation unit and plotted in one diagram. (D) Peak intensity CV comparison between ADE and manually loaded *fs*PAGE. (n=3)

To further optimize the peak intensity unformity, we investigated the relationship of source plate-*fs*PAG distance and peak intensity CV. In this study, we quantified the BSA* intensity CV at four distances of 0.5, 1, 1.5 and 2.5 mm and plotted the results in Figure 4.6. Slight improvement of uniformity was observed as we reduce the source-to-gel distance from 2.5 mm to 0.5 mm. One possible explanation for this observation is that lowering the distance could promote droplets merging and reduce liquid bouncing.

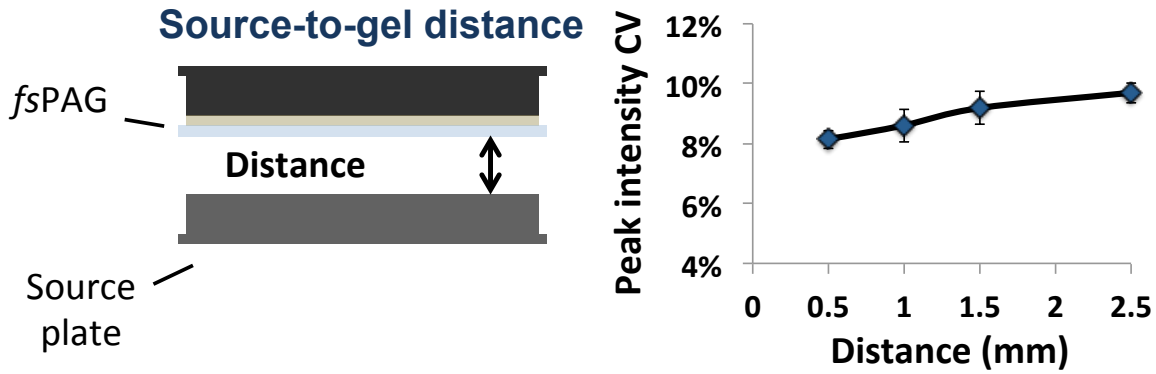

Figure 4.6 Relationship between peak intensity uniformity and source-to-gel distance. The band intensity dropped from 10% to 8% as the distance is reduced from 2.5 mm to 0.5 mm.

4.5 Potential implication of ADE sample delivery on *fs*PAGE

In this chapter, we have successfully developed a novel integration strategy that closely mate the fast, robust ADE transfer with the high-throughput *fs*PAGE array. Such integration has significantly improved the throughput of the assay and uniformity of *fs*PAGE analysis (peak intensity). Table 4.1 summarized a system performance (time, location precision, peak intensity uniformity) of ADE-, manual- and pin tools-enabled *fs*PAG sample delivery.

	Transfer time	Location accuracy	Peak intensity CV
ADE–*fs*PAG transfer	3 min/384 *fs*PAG	100% fully filled	8%
Manual-*fs*PAG transfer	20 min/384 *fs*PAG	N/A	29%
Pin tool-*fs*PAG transfer	20 min/384 *fs*PAG	<20% fully filled	N/A

Table 4.1 Comparison of system performance (transfer time, location accuracy and peak intensity CV) of ADE-, manual- and pin tool-*fs*PAG transfer.

Moreover, the automated sample delivery with high-throughput PAGE assay will find a broad relevance in many biological applications. The successful demonstration of ADE-*fs*PAGE will greatly spurred the development of electrophoresis based high-throughput screening

assay, including antibody characterization and selection (see chapter 5), riboswitch screening and drug target screening. The next chapter will detail a real biochemical application of using ADE-*fs*PAG for rapid K_D measurements of Fab fragment antibody-eGFP binding reactions.

Chapter 5 High-throughput antibody binding affinity measurements with *fs*PAGE

5.1 Introduction

Antibodies enjoy a variety of applications in research laboratory, clinical diagnostics and pharmaceutical industries[107-109]. However, a great variation of quality and performance was observed for commercial antibodies due to the difference in their production process and new approaches to improving the reliability of antibody reagents are critically needed.[4,110,111] As an example, polyclonal antibodies produced by infecting animal and monoclonal antibody from hybridomas could behave quite differently in use and even different batches of polyclonal antibodies from the same animal never result in the same mix of antibody, making it difficult for researchers to ensure their specificities and binding affinities. Scientists now recommend designing recombinant monoclonal antibodies using well-characterized sequence databases[4]. However, despite the hurdles in funding and enforcing the sequence-publishing policy, recombinant antibodies will face the same validation issues in the production of conventional polyclonal and monoclonal antibodies[112]. In any case, it is clearly that the development of an efficient and low-cost validation platform is an essential step to improve the antibody quality and reliability. Validation of antibodies includes a variety of properties such as their specificity, reproducibility and affinity and currently one challenge of antibody validation is the lack of consensus of guidelines or standardized methods for determining the validity of these reagents[113]. Particularly for the affinity validation, a universal metric —— disassociation constant (K_D, moles/liter) provides insight into molecular affinity. K_D is an equilibrium constant that describes the propensity of a large complex molecule to reversibly separate into smaller components. Though it measures the disassociation process, K_D is generally used by scientists to indicate the molecular binding affinity of the binding pair. For a typical molecular binding reaction A+B=AB, K_D is quantitatively expressed by equation 1:

$$K_D = \frac{[A] \cdot [B]}{[AB]} \quad (1)$$

As for a typical molecular binding reaction, [A], [B] and [AB] can be viewed as the concentration of target protein, ligand and the complex at equilibrium.

K_D has a wide use in life science and pharmaceutical industry and it is a critical standard in many applications such as drug screening and antibody selection. Conventionally, enzyme linked immunosorbent assay (ELISA)[114] and surface plasmon resonance (SPR)[115] were used for K_D measurements, however, due to their heterogeneous immunoassay format, those measurements requires sophisticated surface chemical treatment. For example, analyte proteins are biotinylated prior to use on streptavidin coated ELISA plate. These implementations not only extend the experimental processing time but also likely alter the physicochemical properties of the analytes. Furthermore, the surface-based measurement suffers from mass transport limitation, in which the diffusion-dominating transport

significantly increases the time for the target antigen to reach the active immobilized antibody site. In fact, some reactions may never reach equilibrium, making these assays only qualitative in characterizing the relative binding, instead of providing accurate and quantitative measurements[116,117].

Advanced surface-based commercial systems for K_D measurements were developed to enhance the sensitivity and throughput of the traditional ELISA/SPR assays, such as the Octet® system and the GE Biacore™ system. These automated systems rely on surface immobilization of the target analytes and utilize innovative way for the concentration measurement. For example, Octet® uses bio-layer interferometry (BLI) to characterize the molecular binding reaction via the interference pattern of white light[118] reflected from two surfaces: a layer of immobilized protein on the biosensor tip and a internal reference layer. Target ligand binding to the immobilized protein increases the thickness of the "bio-molecule" layer and induces a shift of the interference pattern from which the kinetic information is recorded. Regardless of the improvements achieved in experimental implementation, these assays do not overcome the intrinsic mass transport limitation of the surface-based measurements. Additionally, these measurements typically last several hours for one K_D, making them incompatible for performing high-throughput antibody affinity validation assays.

Affinity capillary electrophoresis (ACE) is a commonly used electrophoretic technique to study the molecular binding reaction and it was first used for equilibrium constant measurement of Ca^{2+} and Zn^{2+} with serum albumin using gel electrophoresis in 1960[119]. Over its 5 decades of development, ACE has evolved into a variety of different formats to accommodate different molecular types and kinetic regions. However, the basic idea behind ACE remains the same and is illustrated in Figure 5.1. ACE utilizes the binding-induced electrophoretic mobility shift to fractionate molecular populations, followed by data acquisition and K_D extraction. The schematic in figure 5.1A shows the operation of a typical ACE measurement. Incubated mixture of A and B is loaded on capillary and the molecular complex AB and free A is separated under applied electric field. The electropherogram in Figure 5.1B illustrates the formation of complex AB with the concentration titration of B. Increasing the concentration of ligand B in the mixture increases the peak intensity of AB. K_D is then extracted by quantitatively analyzing the relationship between the amount of AB and [B] concentration in the diagram shown in Figure 5.1C[120]. ACE is generally performed in homogeneous medium without stabilization reagents and do not suffer from complication related to phase-dependent behavior of solutes[121]. Another advantage of ACE is the potential adaption to scaled-up analysis. While ACEs are attractive, existing formats are low-throughput. A series of high-throughput electrophoretic tools have been invented in the last decade[87,92,122,123], some of which are amenable for rapid and quantitative K_D measurements, opening door to the innovation of ACE tools.

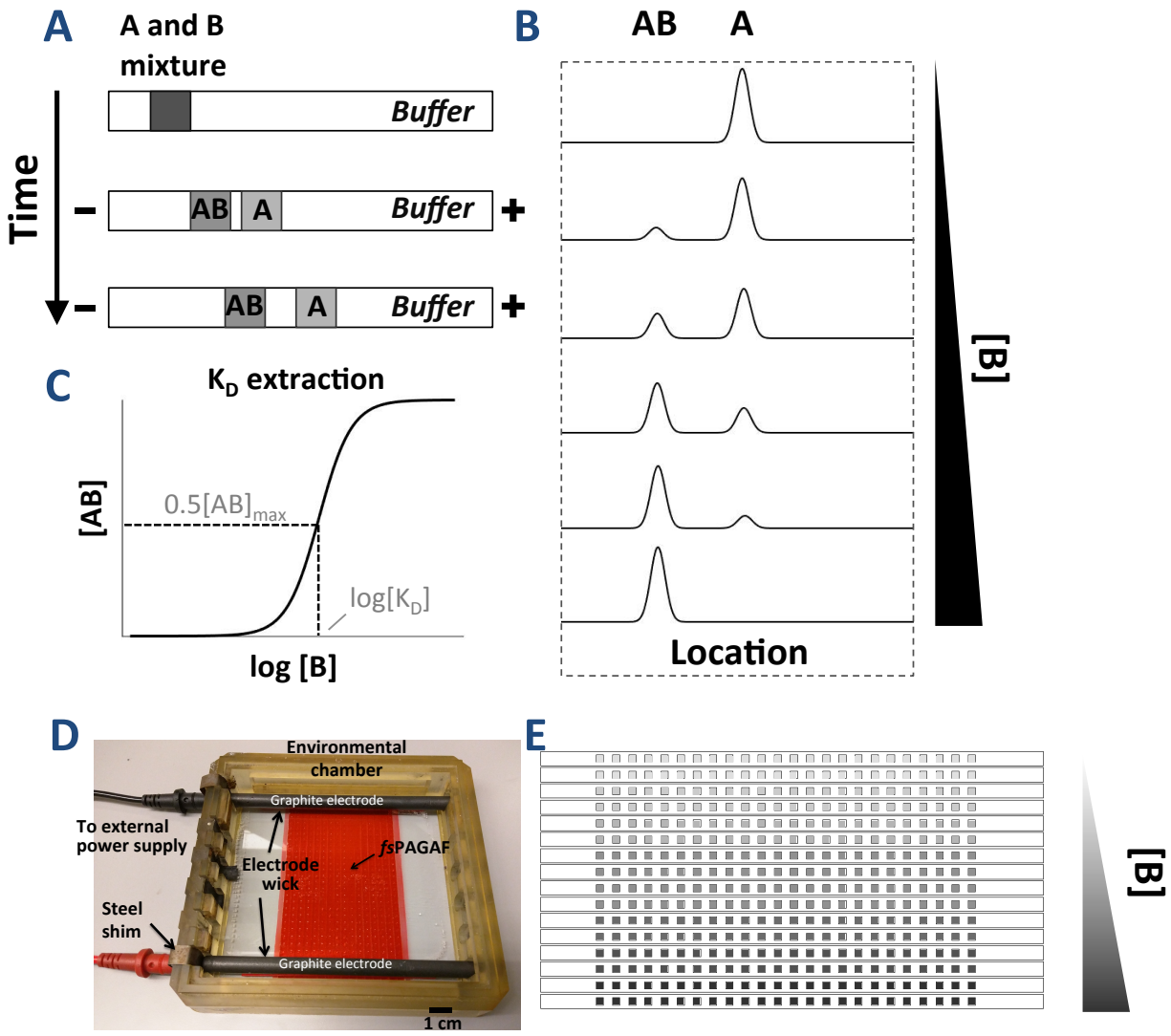

Figure 5.1 Schematic of K_D measurements in Affinity capillary electrophoresis (ACE) and *fs*PAG affinity assays. (A) Incubation solution of A and B subject to electrophoretic separation in ACE. The binding of B on A decreases the electrophoretic mobility of the complex and migrates slower than A. (B) Electropherogram of B concentration titration. Higher concentration of B increases the formation of AB. (C) The amount of [AB] is plotted against log [B] from which the K_D is extracted. (D) Experimental setup of *fs*PAGAF. *fs*PAGAF gel was dyed with red food color (McCormick, Sparks, MD). Electrode wicks and graphite were sequentially aligned on top of the two ends of the *fs*PAGAF device to electrically address the assay. (E) A schematic of reagents arrangement on 384-plex *fs*PAGAF. Fixed concentration of A with increased concentrations of B was arranged from top to bottom rows. Multiple A can be arranged horizontally in columns and assayed simultaneously.

In this study we introduced *fs*PAG affinity assays (*fs*PAGAF) for high-throughput molecular binding measurements, powered by Echo® acoustic droplet ejection (ADE). In particular, we

measured the K_D of several fragment antigen-binding (Fab) fragments for enhanced green fluorescent protein (eGFP). The assay features 384 concurrent separations on one *fs*PAGAF device (see figure 5.1D). The gel structure is dimensioned to benefit from the favorable transport scaling afforded by miniaturization. Figure 5.1D shows the electrophoretic setup of the assay. Figure 5.1E shows the schematics of spatial arrangement of ligand concentration titration for K_D measurements. A fixed concentration of A was incubated with increasing amount of B from the top to bottom rows. Multiple targets can be analyzed simultaneously. Using a 8 concentration titration measurement with triplicate data point, one piece of *fs*PAGAF could theoretically handle up to 16 target analytes in one hour (details are discussed in later sections). Table 5.1 shows that the *fs*PAGAF-ADE possesses better assay throughput, sample consumption performance than the Octet and ELISA systems.

	***fs*PAGAF-ADE**	***fs*PAGAF-manual**	**Octet Red384**	**ELISA**
Throughput	Up to16 K_D/hour	Up to 4 K_D/hour	~0.8 K_D/hour	0.1 K_D/hour
Sample consumption	~30 ng (Fab) ~65 pg (ligand)	~30 ng (Fab) ~65 pg (ligand)	~10 µg (Fab) ~ 4 µg (ligand)	~10 µg (Fab) ~ 30 ng (ligand)
Kinetic data?	No	No	Yes	Yes

Table 5.1 A brief comparison of system specifications between *fs*PAGAF and other popular affinity measurement tools.

In this study, we measured K_D of 6 anti-eGFP fragment antigen-binding (Fab) fragments on one 384-plex *fs*PAGAF. We integrated non-contact acoustic droplet ejection technology (ADE) with high-throughput electrophoretic separations on the open-microfluidic *fs*PAGAF using Labcyte Echo liquid handler to facilitate the sample reagents loading step. Our first-in-kind workflow integrated (i) rapid mesofluidic polyacrylamide gel electrophoresis arrays (*fs*PAG) for binding dissociation constant (K_D) determination with (ii) the Labcyte Echo liquid handler for automated, fast immunoreagent characterization.

5.2 Materials and methods

Reagents: 6 recombinant anti-eGFP Fab fragments (rAB1003, rAB1004, rAB1005, rAB1006, rAB1007and rAB1008) and eGFP were produced at UCSF Recombinant Antibody Network according to protocol descried by Hornsby et al.[124] Each Fab was designed to target eGFP with slight difference in the Complementarity determining region sequence. To enhance fluorescent detection sensitivity, eGFP was fluorescently labeled in house with Alexa fluor 647 (AF647) labeling kit (Thermo Fisher Scientific, Waltham, MA). Tween-20 and bovine serum albumin (BSA) powder were purchased from Sigma-Aldrich (St. Louis, MO). 4-(2-hydroxyethyl)-1-piperazineethanesulfonic acid (HEPES) buffer was purchased from Thermo Fisher Scientific. Other reagents used were the same as those described in Chapter 3.

K_D measurements with *fs*PAGAF. *fs*PAGAF device was fabricated with micro-molding as described in Chapter 4. Buffer used for binding affinity measurements contains 20 mM HEPES, 0.05% Tween-20 and 0.2% BSA (pH=7.4). To measure the K_D value, 0.3 nM eGFP was incubated in the described buffer with various concentrations of Fab fragments. After 2 hours incubation, the binding reaction solutions were loaded onto *fs*PAG and electrophoretically separated with 50V/cm electric field. 0.1-2 uL Rainin pipette was used for manual sample loading and Echo 525 was used for automated sample loading.

Sample loading with Echo 525. Sample loading was performed at Labcyte Inc. on Echo 525 according to protocol described in Chapter 4. Briefly, a 400 μm thick 10%T 3.3%C 384-plex *fs*PAG was soaked in run buffer for 5 minutes and installed on destination plate with the "two-step registration" strategy. The gel-destination plate and sample source plate were then inserted into Echo for ADE sample transfer. Sample delivery volume was set to 400 nL and 0.5 mm source plate-gel distance was used for ADE transfer according to the optimization in Chapter 4.4. After sample loading, the *fs*PAGAF gel device was taken off and placed onto electrophoresis chamber for electrophoretic separation.

Data Acquisition and processing. After electrophoresis, the *fs*PAGAF device was dried in nitrogen airflow for 5 minutes to fully remove the moisture content in the gel matrix. Fluorescence imaging of the gel was conducted using an inverted epi-fluorescence microscope (Olympus IX-70) equipped with a 2X objective (PlanApo, N.A. = 0.08, Olympus, Center Valley, PA). X-Cite® exacte mercury lamp (Lumen Dynamics, Mississauga, Canada) provides the illumination light source and imaging was taken with Peltier cooled charge-coupled device (CCD) camera (CoolSNAP HQ2, Roper Scientific, Trenton, NJ). Large-area imaging for 384-plex *fs*PAG was performed with Scan Slide function on Metamorph (Molecular Devices, Sunnyvale, CA). Imaging processing and subsequent data analysis were performed on ImageJ (NIH, Bethesda, MD) and Matlab (Natick, MA). Fluorescent signals were averaged over the transverse direction of separation lane to generate the fluorescence intensity profile and intensity peaks were fitted with Gaussian distribution. The intensity (area-under-curve) ratio of bound eGFP to total eGFP at each Fab concentration was plotted on the titration curve, and least-square fitting of binding equation (equation 2) was applied on the data to extract the K_D value.

K_D measurements with Octet Red384. The K_D value measured with *fs*PAGAF was benchmarked against Octet Red384 BLI measurement according to the standard protocol. Briefly, to measure the K_D on Octet Red384, 150 nM Fab and a series of concentration of ligand eGFP (200 nM, 100 nM, 50 nM, 25 nM, 12.5 nM and 6.125 nM) were filled in black 96-well plate. A total of 4 K_D measurements were made. To evaluate K_D results from *fs*PAGAF and provide reference, binding of rAB1003 with AF647 labeled eGFP in HEPES buffer was studied. To investigate the influence of fluorescent labeling and buffer composition on affinity, 3 more binding reactions were characterized —— rAB1003 and unlabeled eGFP in HEPES, rAB1003 and AF647 labeled eGFP in PBST (1X PBS, 0.05% Tween-20, 0.2% BSA, pH=7.4) buffer and rAB1003 and unlabeled eGFP in PBST. Anti-Human Fab-CH1 antibody coated biosensors were used for measurements. 100 mM glycine

titrated to pH=1.5 with HCl was used as regeneration buffer for biosensor in between each K_D measurements.

5.3 K_D measurement with *fs*PAGAF

Equation 1 describes the quantitative relationship between each component in a molecular binding reaction. To rearrange the equation, we would arrive at,

$$\frac{[AB]}{[AB]+[A]} = \frac{K_D}{K_D+[B]} \quad (2)$$

The left hand side of equation 2 represents the percentage of bound A in total A. The equation indicates that 50% of total A would bind to B when $K_D = [B]$. In a typical K_D measurement, we set [A] much lower than K_D so that only a small fraction of B would bind to A. Under this circumstance, $[B] \approx [B_{Total}]$ and we ignore the change in [B]. This treatment suggests that [B] can be replaced with $[B_{Total}]$ which greatly simplifies the data processing. Next, $[AB]/[A_{Total}]$ was plotted against $[B_{Total}]$ and K_D value can be extracted with least square fitting.[120]

In the Fab-eGFP system, eGFP was used as A and Fab as B. To enhance the sensitivity with fluorescent imaging, eGPF was labeled with AF647 so that sub-nanomolar concentration became fluorescenrly visible.

A time-sequential separation of bound eGFP and unbound eGFP was shown in figure 5.2.

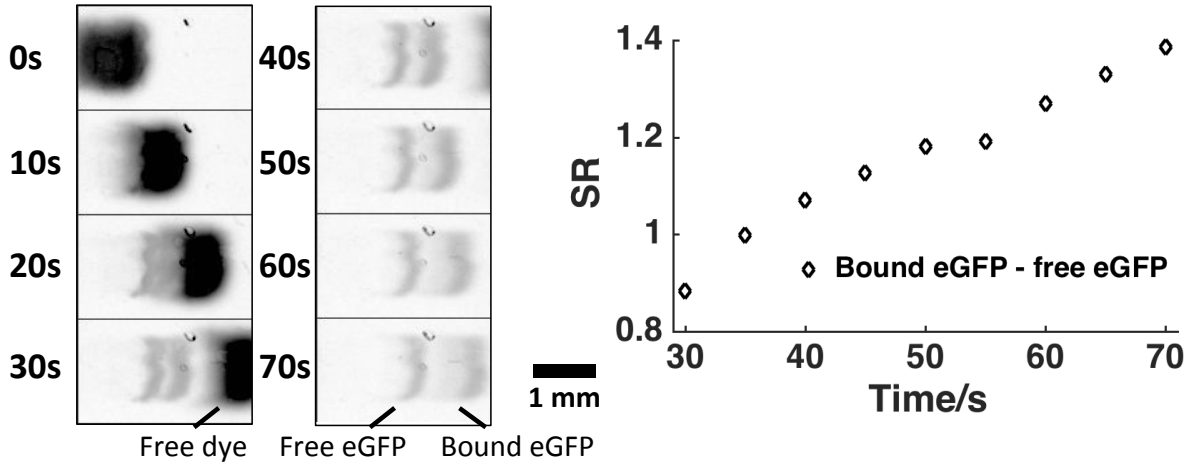

Figure 5.2 *fs*PAGAF enables fast separation of bound eGFP and free eGFP in less than 1 minute. Left shows the fluorescent time-sequential separation image of bound eGFP and free eGFP (0-70 seconds). Right diagram plots the time-sequential separation resolution (SR) of the binding pairs from 30 to 70 seconds.

The Fab-eGFP complex has a larger molecular weight than the unbound eGFP and therefore migrates with a lower electrophoretic mobility. Figure 5.2 shows the electrophoretic

separation of an incubated reaction between rAB1003 and eGFP. To quantity the separation, we define the separation resolution (SR) between the bound and unbound eGFP as,

$$SR = \frac{\Delta L}{2(\sigma_1 + \sigma_2)} \tag{3}$$

where ΔL is the peak distance and σ_1 and σ_2 are the standard deviation of the two peaks. More details of SR can be found in equation 5 of Chapter 1. At a 50 V/cm electric field, the separation resolution reached 1 in 40 second.

We next sought to measure the Fab-eGFP K_D on a multiplexed *fs*PAGAF device by manually loading the sample. To ensure data reliability, we maintained eGFP at 0.3 nM and titrated Fab concentration over 10 points from 0 nM to 500 nM. We used a 60-plex *fs*PAGAF device (9 mm unit spacing) for the measurements. At each concentration, 6 replicates of data points were taken to enhance the statistical significance. Figure 5.3A displays the separation of free rAB1003 and complex on *fs*PAGAF and Figure 5.3B shows the electropherogram of separation at each rAB1003 concentration.

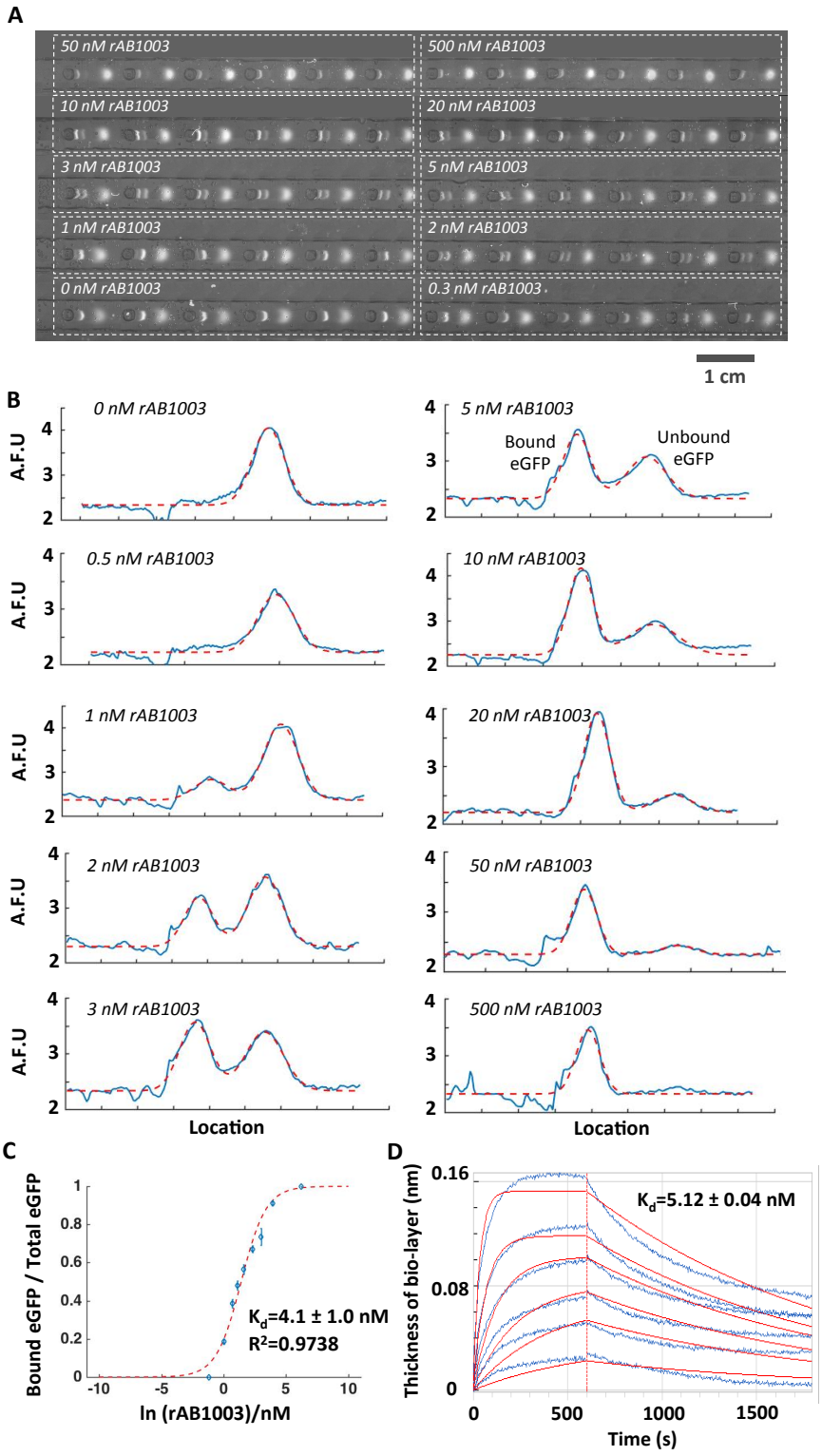

Figure 5.3 K_D measurement of rAB1003-eGFP on 60-plex *fs*PAGAF with manual sample loading. (A) 0.3 nM of AF647-eGFP was incubated with a range of concentration of rAB1003 and assayed on *fs*PAGAF. 6 replicate data points were collected at each

concentration. Separation was performed at 50V/cm for 40 seconds. (B) Electropherogram of bound and unbound eGFP separation. To estimate the intensity of each peak, the electropherogram was fitted with Gaussian distribution. Blue solid lines shows the real electropherogram data and red dashed line shows the fitting results. (C) The peak intensity ratios of bound eGFP and total eGFP (sum of free eGFP and bound eGFP) were calculated at each concentration point and plotted on a line-log diagram. Error bar was calculated from 6 replicate runs. Least-square curve fitting of intensity value at each concentration was fitted to equation 2 to reveal the K_D values. Blue diamond with error bar indicates data points and the red dashed line shows the fitting results. (D) K_D measurement of rAB1003 on Octet. 150 nM rAB1003 was incubated with 6 concentrations of eGFP and the kinetic curve was plotted for each concentration (from higher to lower). K_D and its standard deviation were extracted from these 6 measurements.

The accuracy of quantification is essential to the quality of the K_D measurement. To overcome the unit-to-unit variation problem inherent to the multiplexed *fs*PAGAF, we[92] previously used marker protein as internal standard (IS) to which the intensity of the target molecules were normalized for comparison. In *fs*PAGAF, to minimize any potential cross-reaction as well as the impact of IS on the binding reaction, we developed a "Self-IS" strategy in which we normalized the intensity of the bound eGFP to the total eGFP (sum of bound and free eGFP). Using this strategy, the relative amount of bound eGFP would theoretically increase from 0 at 0 nM Fab to 1 at saturation. Such relationship was plotted on a semi-log graph in Figure 5.3C and least-square fitting of binding data to equation 2 revealed the K_D value.

To verify the reliability of the *fs*PAGAF measurements, we benchmarked the results against the commercial Octet® system. Octet is a surface-based binding kinetic technology that uses BLI to extract the k_{on} and k_{off} and determines K_D from the kinetic data. To make the measurements, we incubated 150 nM rAB1003 with a series of AF647-eGFP concentrations (200, 100, 50, 25, 12.5 and 6.25 nM). (See figure 5.3D) According to the standard kinetic measurement protocol[120], the observed rate constants for association k_{obs} were extracted for each concentration. Theoretically, k_{obs} is linear combination of k_{on} and k_{off}.

$$k_{obs} = k_{on}[B] + k_{off} \quad (4)$$

k_{on} and k_{off} were then extracted by fitting the k_{obs} at each [B] to the linear equation 4 and K_D is calculated by taking the ratio of k_{off} and k_{on}. K_D measured from *fs*PAGAF was 4.1±1.0 nM, compared to 5.12±0.04 nM from Octet measurement, indicating the two approaches gives comparable affinity values.

5.4 Effect of fluorescent labeling and buffer composition on the K_D measurements

The K_D value is sensitive to the physicochemical state of the binding molecules and environment of the binding reaction. In fact, at least two factors could influence the K_D measurement in *fs*PAGAF. (1) *fs*PAGAF is a fluorescent detection based method for equilibrium constant measurements and fluorescent antigen labeling is a prerequisite in the assay. Covalent binding with dye likely alters the charge value and distribution on the

molecule and potentially hides/exposes the epitopes on the surface of the antigen. (2) The buffer aqueous environment also plays a critical role in affecting the binding affinity of the reaction. The commonly used PBS buffer (1X PBS + 0.05% Tween 20 + 0.2% BSA) has high conductivity and is not suitable for electrophoresis. In *fs*PAGAF, HEPES buffer was used instead. Both buffers have a pH of 7.4 and HEPES is widely used in cell culture because of its good ability to maintain physiological pH. HEPES has previously been used for K_D measurements in affinity capillary electrophoresis[125,126]. In fact, a variety of buffers were used in ACE and they all showed good compatibility[127].

Here we measured the rAB1003 K_D difference caused by fluorescent labeling and compared two buffer conditions (PBS and HEPES) with Octet. Figure 5.4 shows the affinity results from the following four conditions. (1) AF647-eGFP + rAB1003 in HEPES. (2) Unlabeled eGFP + rAB1003 in HEPES. (3) AF647-eGFP + rAB1003 in PBS. (4) Unlabeled eGFP + rAB1003 in PBS. For both buffers, 0.05% tween-20 and 0.2% BSA were added to minimize non-specific binding.

Both the kinetic and equilibrium data were summarized in table 5.2. Similar to the Octet measurements in Section 5.3, 150 nM of rAB1003 were incubated with a range of concentrations of eGFP (200 nM to 6.25 nM). For each binding reactions, 6 concentrations of eGFP were included in K_D determination to ensure measurement accuracy. As can be seen, K_Ds in HEPES were generally lower than PBS and fluorescently labeling slightly decreases K_D in both buffers. Regardless, these differences are not significant. Interestingly, we found out fluorescently labeling alters the kinetic value of the binding reaction by increasing both the k_{on} and k_{off}. Such differences in binding kinetics are potentially due to the change of charge value and spatial distribution on the molecular. Similar study has been reported elsewhere[128] where binding kinetics were measured against a series of different dye molecules. However, no direct prediction can be made to determine whether labeling increases or decreases the kinetic rate.

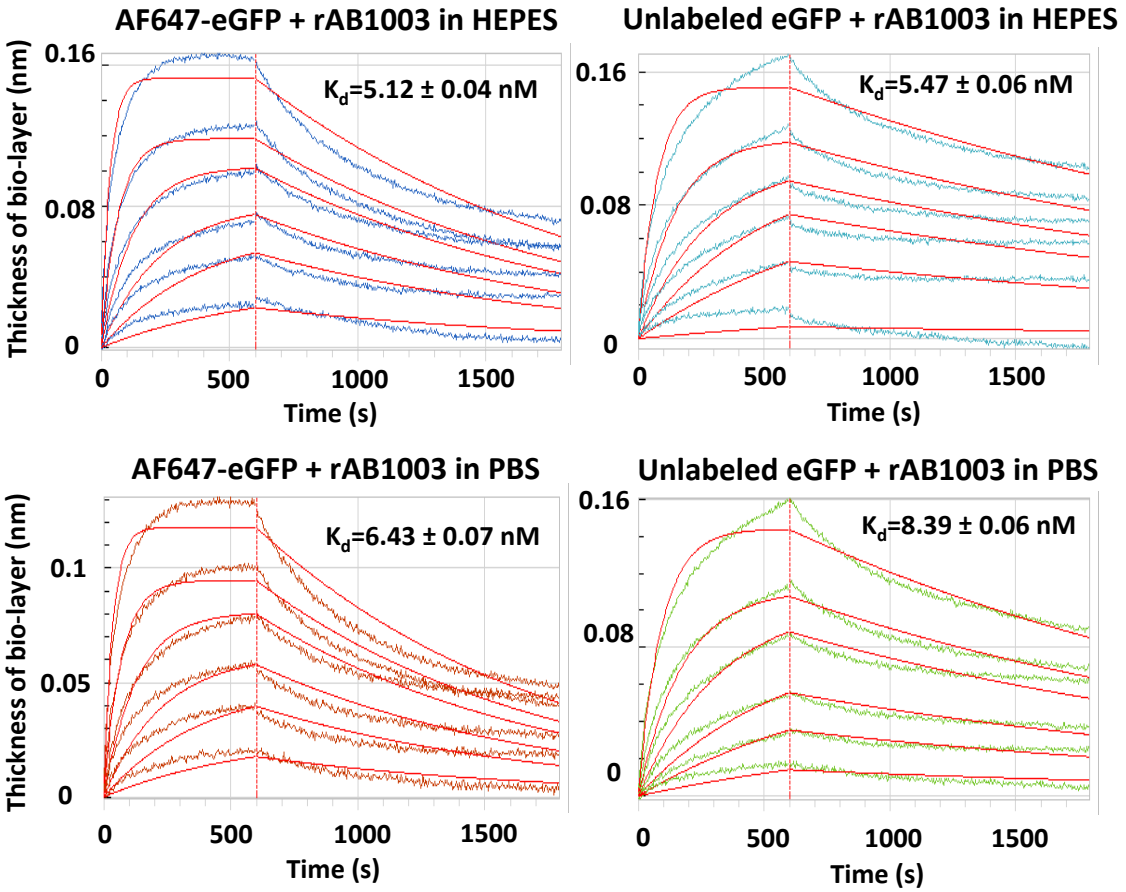

Figure 5.4 Effects of fluorescent labeling of the Fab molecule and buffer composition on K_D measurements with Octet red384. Four conditions were studied. Both raw kinetic data and fitting results (in red) were plotted.

	K_D (nM)	k_{on} ($M^{-1}S^{-1}$)	k_{off} (S^{-1})
AF647-eGFP+Fab in HEPES	5.12 ± 0.04	(14.5 ± 0.1) × 10^4	(7.43 ± 0.03) × 10^{-4}
Unlabeled eGFP+Fab in HEPES	5.47 ± 0.06	(6.50 ± 0.04) × 10^4	(3.55 ± 0.02) × 10^{-4}
AF647-eGFP+Fab in PBS	6.43 ± 0.07	(13.7 ± 0.1) × 10^4	(8.79 ± 0.03) × 10^{-4}
Unlabeled eGFP+Fab in PBS	8.39 ± 0.06	(5.20 ± 0.03) × 10^4	(4.36 ± 0.02) × 10^{-4}

Table 5.2 Summary of kinetic and equilibrium data from experiments in Figure 5.4.

5.5 K_D measurements on high-throughput 384-*fs*PAGAF

We next sought to scale up the K_D measurement into high-throughput format and automate the sample "prep-delivery-assay" workflow using the 384-plex *fs*PAGAF and Echo acoustic droplet ejection (ADE). We aimed to leverage the fast sample transfer and improved unit-to-unit uniformity brought by ADE to enhance the analytical throughput and measurement reliability (details can be found in Section 4.4). Briefly, sample loading on 384-plex *fs*PAG reduces >80% of the processing time and improves 75% of the unit-to-unit uniformity (by CV of peak intensity). With the high-density patterning of separation units, a 384-plex *fs*PAGAF can theoretically handle up to 16 K_D simultaneously, at which 8 concentration points were assayed for each binding pair with 3 replicate data points. In this study, we performed a simultaneous K_D measurement of 6 Fabs (rAB1003, rAB1004, rAB1005, rAB1006, rAB1007 and rAB1008) over 8 concentration points on a 384-plex *fs*PAGAF. (See Figure 5.5)

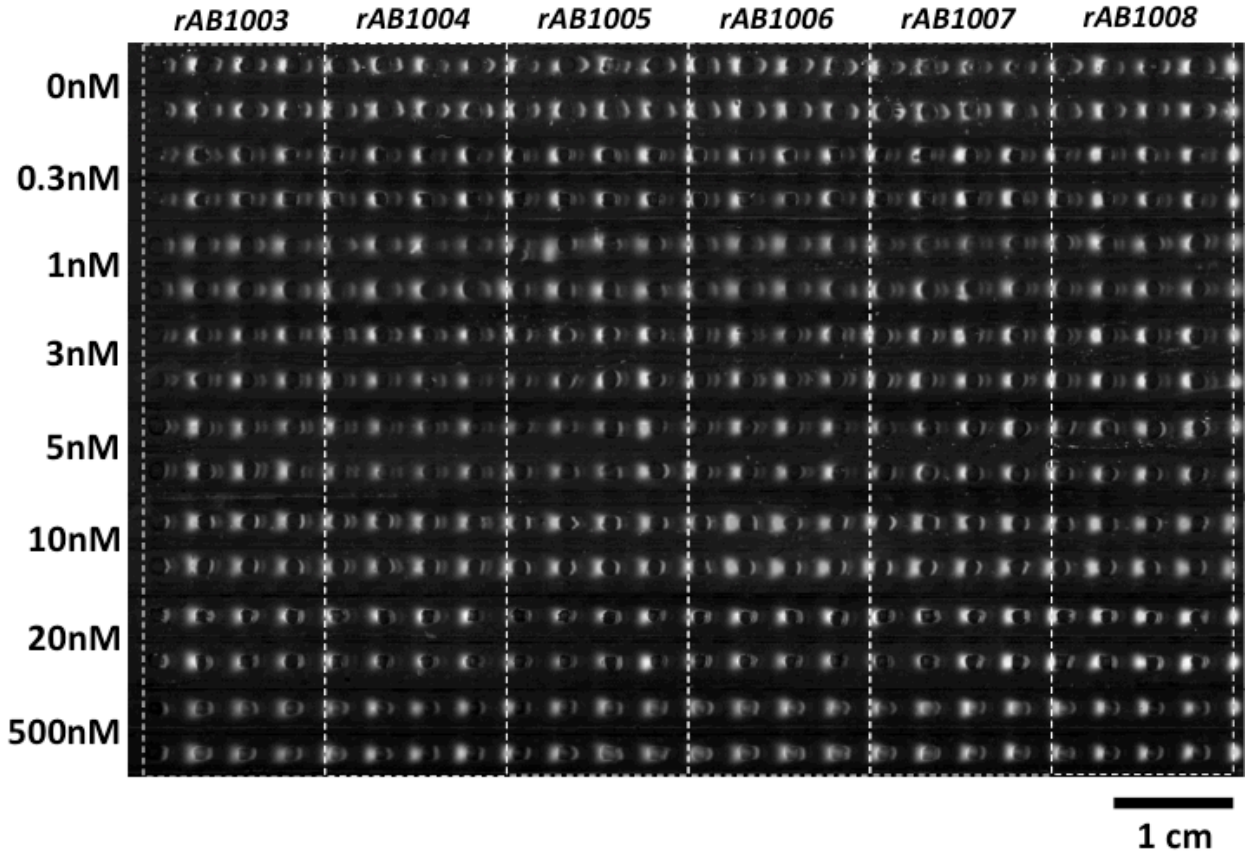

Figure 5.5 ADE loaded 384-*fs*PAGAF enables simultaneous K_D determination of 6 Fabs. 4 columns of separation units were used for each Fab (isolated by white dashed line) and each concentration point was assayed in 2 rows, producing 8 replicate of data points. 3 bands were observed in each separation unit —— bound eGFP, free eGFP and free dye (AF647), from left to right.

The measurement was performed in a similar way described in Section 5.3. For each antibody species, 0.3 nM eGFP was incubated with Fab over a range concentration from 0 to 500 nM.

Leveraging the geometry of the *fs*PAGAF design, we performed 8 replicate data points at each concentration for every Fab on the 384-format. Compared to the well-to-well distance of 9 mm in a standard 96 well plate footprint used in previous application, the 384-format has half the well spacing (4.5mm). To accommodate the reduced dimension and to restrict the fast-moving free dye in the local separation unit, we reduced the separation time to 28 seconds. Under such separation condition, the electrophoresis was optimized to terminate when the fast-moving free dye arrives at the rear edge of the next sample well. With this implementation, proximal separation units remain independent from each other so that local fluorescence quantification is not influenced by adjacent units. The electropherogram of separations at each concentration point along with affinity data for 6 Fabs are plotted in Figure 5.6 in a similar fashion of that in Figure 5.3C.

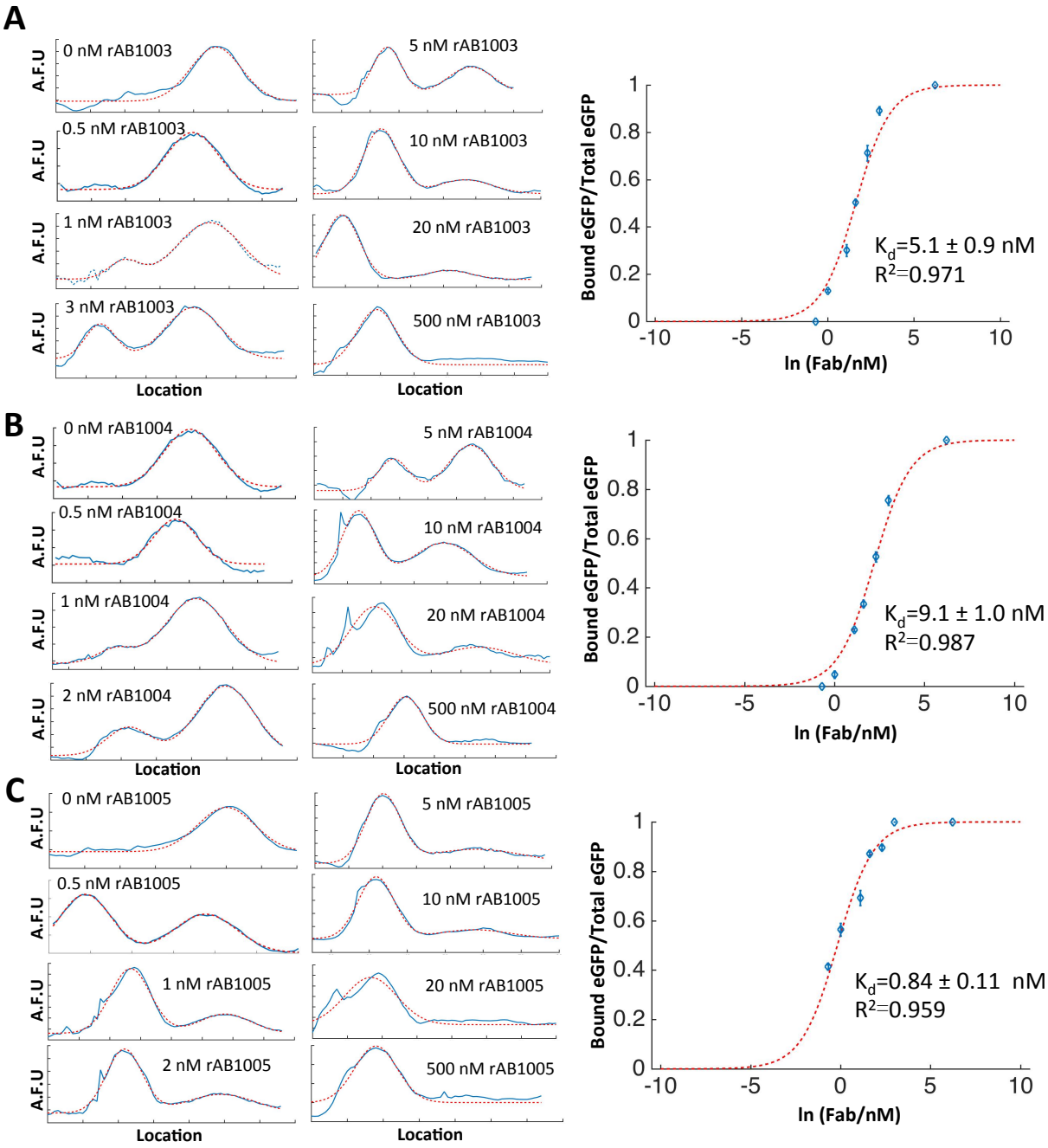
A
0 nM rAB1003
5 nM rAB1003
0.5 nM rAB1003
10 nM rAB1003
1 nM rAB1003
20 nM rAB1003
3 nM rAB1003
500 nM rAB1003
A.F.U
Location
Bound eGFP/Total eGFP
ln (Fab/nM)
K_d=5.1 ± 0.9 nM
R^2=0.971
B
0 nM rAB1004
5 nM rAB1004
0.5 nM rAB1004
10 nM rAB1004
1 nM rAB1004
20 nM rAB1004
2 nM rAB1004
500 nM rAB1004
K_d=9.1 ± 1.0 nM
R^2=0.987
C
0 nM rAB1005
5 nM rAB1005
0.5 nM rAB1005
10 nM rAB1005
1 nM rAB1005
20 nM rAB1005
2 nM rAB1005
500 nM rAB1005
K_d=0.84 ± 0.11 nM
R^2=0.959

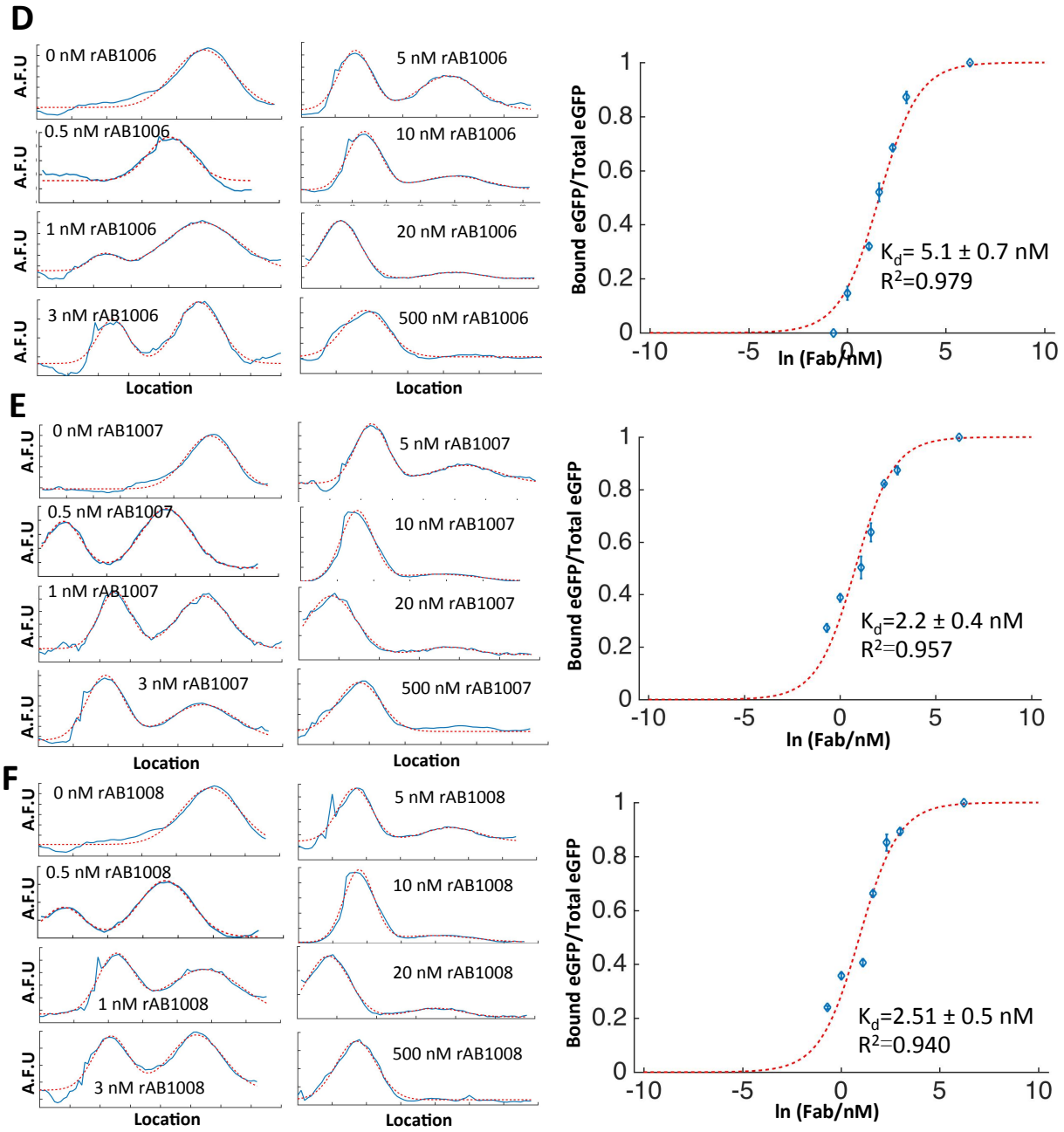

Figure 5.6 K_D measurements for 6 Fabs. The ratios of bound eGFP to total eGFP versus In ([Fab]) were plotted for all Fabs. K_D extractions were performed with least-square fitting of equation 2 on all separation data. (A)-(F) Measurements for rAB1003, rAB1004, rAB1005, rAB1006, rAB1007 and rAB1008. In all electropherograms, blue lines indicate the raw data and red dashed lines represent the fitting results. On titration curves, blue diamonds indicate data from measurements and red dashed line represents fitting results.

5.6 Conclusion

In this work, we designed and demonstrated a high-throughput, quantitative assay for robust determination of immunoreagent binding affinity characteristics. Using *fs*PAGAF, we were able to simultaneously determine the dissociation constant K_D of 6 recombinant Fab fragments. In fact, theoretical calculation indicates that with a standard format of 8 concentration points and triplicate data point K_D measurement, one piece of 384-plex *fs*PAGAF was able to handle up to 16 target analytes. From our estimation, the total processing time for a 384-plex *fs*PAGAF is ~1 hour, consisting of 30 minutes sample preparation, 5 minutes device fabrication, 3 minutes ADE sample loading, 1 minute electrophoretic separation and 20 minutes fluorescent imaging. In comparison, manually loaded *fs*PAGAF with acceptable separation performance is limited to a 96-plex format, which requires 1.2 hours total processing time. More comparison with Octet shows that a typical 96 well plate is processed in ~5 hours, producing 4 K_D with 28 data points (7 concentrations for each K_D). Figure 5.7 plots the data points per hour comparison for *fs*PAGAF-ADE, *fs*PAGAF-manual and Octet.

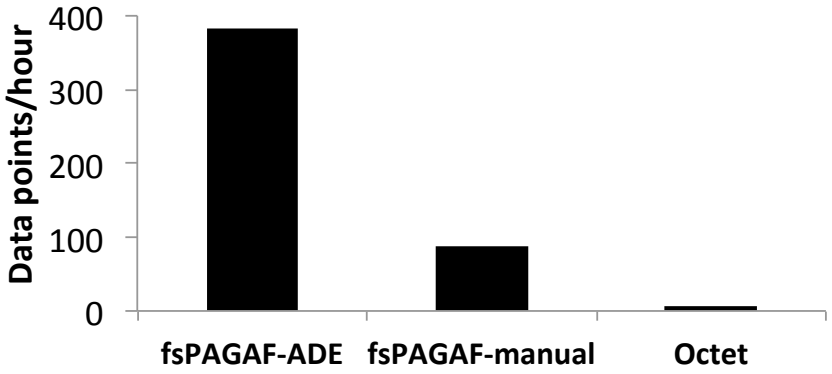

Figure 5.7 Data points/hour comparison for three systems. *fs*PAGAF-ADE, *fs*PAGAF-manual and Octet Red384.

Using a dual-prong mesofluidic design strategy, we integrated non-contact acoustic droplet ejection technology (ADE) with high-throughput electrophoretic separations. Our first-in-kind workflow integrates (i) rapid mesofluidic polyacrylamide gel electrophoresis arrays (*fs*PAGAF) for binding dissociation constant (K_D) determination with (ii) the Labcyte Echo® liquid handler for automated, fast immunoreagents characterization.

In the assay, the fast and robust ADE replaced the cumbersome manual loading, improving the unit-to-unit uniformity and expediting the workflow with scaled-up 384 concurrent separations.

Despite the advantage in affinity measurement, the current format does not report kinetic value of the binding reagents (See Table 5.1 for more details). Equilibrium constant and the kinetic rates together reflected the binding behavior of the immuno-reagents. Our lab has

recently developed a microfluidic free-standing kinetic polyacrylamide gel electrophoresis (*fs*KPAGE) assay which reports both k_{on} and k_{off} using similar open format polyacrylamide gel systems[129]. Future efforts would focus on integrating both features on one platform and create an all-in-one electrophoresis-based binding characterization tools.

Chapter 6 *fs*PAG western-blotting (*fs*PAGWB) assay

6.1 Introduction

Western blot (WB) is a widely accepted analytical tool that is used to detect specific proteins in many fundamental life science researches and clinical diagnostics[130,131]. In general, WB has a broad relevance in a variety of measurements due to its great sensitivity and specificity in tests. Such advantage stems from the nature of the assay, as WB reports two pieces of physicochemical characteristics: molecular mass/size and immunoaffinity, therefore eliminating the possibility of non-specific biases due to cross-reactivity, that are typically observed in many other immunoassays.

Nevertheless, tradition western blotting is a time-consuming and resource-heavy assay. A full WB processing generally takes up to days of experiments and ~10 μg of antibody usage. In addition, the assay involves several experimental steps and substantial preparation work[132]. The sample is first analyzed on denature polyacrylamide gel electrophoresis and electrophoretic separation of protein samples reveals their molecular mass information. Once the size is determined, the proteins are transferred onto a piece of blotting membrane (e.g. nitrocellulose or polyvinylidene difluoride), where the proteins get immobilized through non-specific hydrophobic interactions, followed by a series of complex handing steps to report immuno-identity. The membrane is first coated with a blocking protein (e.g., bovine serum albumin) to reduce non-specific interactions in subsequent steps and then incubated with immunoprobe solutions that bind to and to specifically read out the target protein.

Though conceptually straightforward, several limitations are inherent to the assays: 1) Use of low separation electric field results in long PAGE time. Generally, protein separations can take up to ~10 hours to complete. 2) The slow mass-transport during diffusional antibody probing requires overnight incubation for immuno-probing. 3) Large sample consumption (10 μg/assay) due to the size of the slab-gel. Therefore, innovation in western blot assay development to reduce resources consumption and improve assay throughput has been an unmet need.

Recent studies on protein analytical tools have greatly improved the assay throughput and processing time. For example, the microwestern arrays developed by Ciaccio et al.[133] combined slab gel format with the noncontact microarrayers to realize 96-plex WB analysis. Regardless of the improved throughput brought over by miniaturization, this approach still relies on conventional membrane transfer and diffusive probing. To further streamline the integration of separation and subsequent immobilization, a commercial capillary electrophoresis-based system called ProteinSimple utilized a technology to perform photo-activated capturing of protein onto the inner wall of capillary, followed by antibody introduction to identify the target proteins[134,135]. This approach eliminated the transfer and blotting steps. However, one limitation to this assay is the low capture efficiencies at ~0.01%, substantially lower than conventional membrane blotting, therefore cutting down the sensitivity of the assay.

The power of microfluidic separation has greatly improved the mass transport limit with reduced analysis time and achieved high-performance separation over short separation distance, therefore allowing high-density patterning of separation units to realize scaled-up analysis. As a result, western blotting benefits from adaption onto microfluidic format. Our group has previously demonstrated several versions of microfluidic western blot assays. In the study of electrostatic immobilization gel, a microchip housing 2-dimensional polyacrylamide gel was used to perform fully integrated western blot. The sample proteins were first separated in the first dimension (vertically) and electrophoretic transferred to a second stage (horizontally) charged gel. The charged gel made of cetyl trimethylammonium bromide act as electrostatic immobilization gel that captures the proteins. Subsequent immuno-probing then reveals the identity of the proteins.[136] In a second demonstration, a photoactive polyacrylamide gel was used as both a separation matrix and the blotting materials. Proteins were first separated and photo-immobilized on the hydrogel with UV exposure. As a result, the use of photoactive gel greatly simplified the experimental procedure and streamlined the sample processing.[137]

However, there are several inherent limitations to these approaches. 1) The in-chip format requires specialized instrumentation and sophisticated fabrication protocol, making them incompatible for standard laboratory analysis. 2) The in-chip format also limits assay scaling-up, as both the fabrication and electrical interfacing become difficult.

The *fs*PAGE technology with ADE could overcome these deficiencies. In this study, we introduce a scalable, automated *fs*PAG WB assay for quantitative high-throughput western blot analysis. The novel WB assay combines the 2-D design for the implementation of "separation-transfer-immunoprobing" with blotting photoactive *fs*PAGE, while introducing a new approach to using electrophoretic sample stacking (e.g., isotachophoresis (ITP) and field-amplified sample stacking (FASS)) during transfer step to achieve high-sensitivity protein detection. Using the *fs*PAGE format, the assay is potentially amenable for scaled-up analysis, powered by acoustic sample delivery (See Chapter 4 for details). Here we present design, fabrication, and preliminary conceptual demonstration of the approach.

6.2 Materials and Methods

Reagents. Alexa Fluor 488-conjugated trypsin inhibitor (TI*), FITC-conjugated bovine serum albumin (BSA*) were purchased from ThermoFisher Scientific (Waltham, MA). Beta galactosidase (β-gal) was purchased from Abcam Inc. (Cambridge, UK) and fluorescently labeled with Alexa Fluor 488 labeling kit (ThermoFisher) in-house. HiLyte 488-conjugated fibronectin (FN*) was purchased from Cytoskeleton Inc. (Denver, CO). Sodium dodecyl sulfate (SDS) was purchased from Sigma Aldrich (St. Louis, MO) and SDS tris-glycine PAGE buffer was purchased from Invitrogen (Carlsbad, CA). Other reagents were the same as described in Chapter 3.

Imaging and data processing. Fluorescence imaging was conducted using an inverted epi-fluorescence microscope (Olympus IX-70) equipped with a 2X objective (PlanApo, N.A. =

0.08, Olympus, Center Valley, PA). An X-Cite® exacte mercury lamp (Lumen Dynamics, Mississauga, Canada) filtered through an XF100-3 filter (Omega Optical, Battleboro, VT) provides the illumination source. A Peltier cooled charge-coupled device (CCD) camera (CoolSNAP HQ2, Roper Scientific, Trenton, NJ) attached to the microscope was used to collect the fluorescence images. Imaging processing was performed with Metamorph software (Molecular Devices, Sunnyvale, CA) and ImageJ (NIH, Bethesda, MD). Subsequent data analysis was performed with Matlab (MathWorks, Natick, MA).

6.3 *fs*PAG WB device design and assay operation

Performance advances of previously reported microfluidic WB assays were limited by the in-chip format. These include the sophisticated in-channel polyacrylamide gel fabrication, equipment-intensive implementation and low-throughput analysis. To overcome these deficiencies of traditional microfluidic device, we explored *fs*PAG Western blot (*fs*PAGWB). We presented the open-channel hydrogel structure in conjunction with photo-immobilization PAG chemistry on a 2-dimenssional device to elevate the analytical performance. This combined approach was an integration of sequential stages of traditional WB. Briefly, it is comprised of transient ITP-enabled sample injection, molecular weight-based protein separation with SDS-PAGE, perpendicular ITP/FASS protein transfer, photo-immobilization and immune-blotting with primary and fluorescently labeled secondary antibodies. We start by describing the geometric design of the *fs*PAGWB device and follow by details in each stage, including experimental procedures and observations.

Figure 6.1A shows the basic structure of the *fs*PAGWB device and the workflow of the assay. We employed a simple 2-part discontinuous PAG to facilitate the integration. The *fs*PAGWB is composed of a separation gel and a blotting gel made from photo-patterning and specifically, the blotting gel contains benzophenone group on the gel matrix that would covalently bind to proteins upon UV exposure.[138] To facilitate protein separation and antibody introduction, separation gel is designed to have a higher density than the blotting gel. The gel is made 100 μm tall and the entire device takes up a 18mm by 18mm footprint. To interface the device with power supply, electrode wicks were aligned on the two ends and graphite electrodes are placed on top in a similar way described in Chapter 3.

A unique feature of the assay is the use of sample stacking during transfer step. Unlike the electrostatic immobilized gel where charged PAG was pattern to capture the protein, a simple buffer exchange after separation is performed to drive the transfer in an ITP/FASS mode, depending on the electrophoretic mobility of the target proteins. In this way, sample proteins were stacked as they were swept towards the blotting gel, without the need for sophisticated PAG chemical manipulation. Figure 6.1B shows the schematics of operation of ITP/FASS on gel and Table 6.1 illustrated the differences in their physics. For a discontinuous buffer system, as is the case for tris-glycine and tris-HCl system, an interface of electrolytes (Cl^- and glycine) form upon the application of electric field. For smaller protein whose electrophoretic mobility in separation gel satisfies $\mu_{glycine} < \mu_{protein} < \mu_{Cl-}$, the protein will get sandwiched at the interface between glycine and protein once the interface sweeps through the analytes (See isotachophoresis schematics in Figure 6.1B). The migration continues in ITP mode in blotting

gel (lower density) until the electrophoresis is manually terminated. For larger protein whose electrophoretic mobility in separation gel satisfies $\mu_{protein} < \mu_{glycine}$, protein would not stack at the electrolyte interface but instead get partially concentrated and falls behind the interface. As the protein hits the gel interface and moves into a lower density gel, it gains mobility and the new mobility $\mu_{protein'}$ satisfies $\mu_{glycine} < \mu_{protein'} < \mu_{Cl-}$. At this point, the protein would overtake the interface and the electrophoresis switch to an ITP mode. Once the ITP is established, electrophoresis is terminated. Therefore, for both ITP and FASS directed transfer, the electrophoresis ends up in ITP mode and proteins get concentrated.

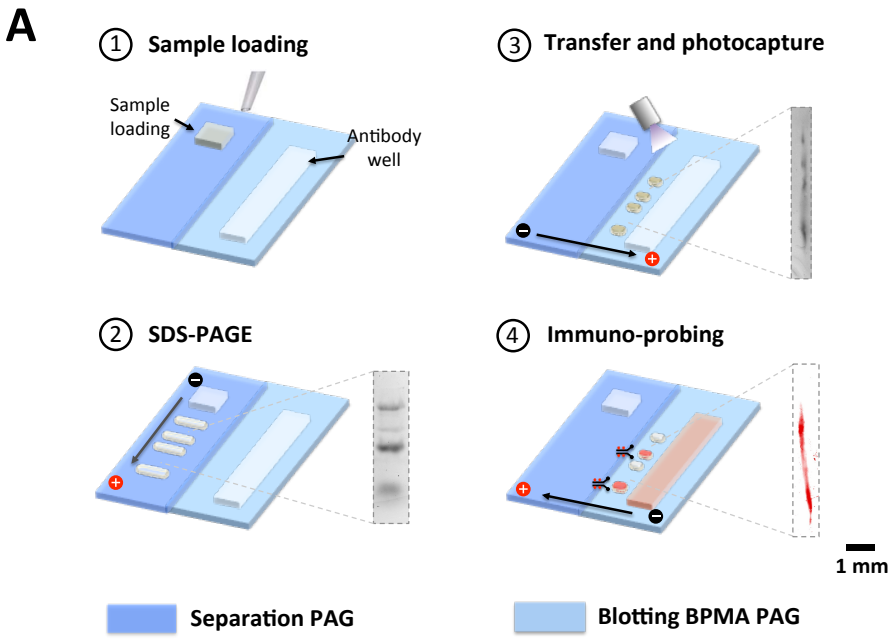

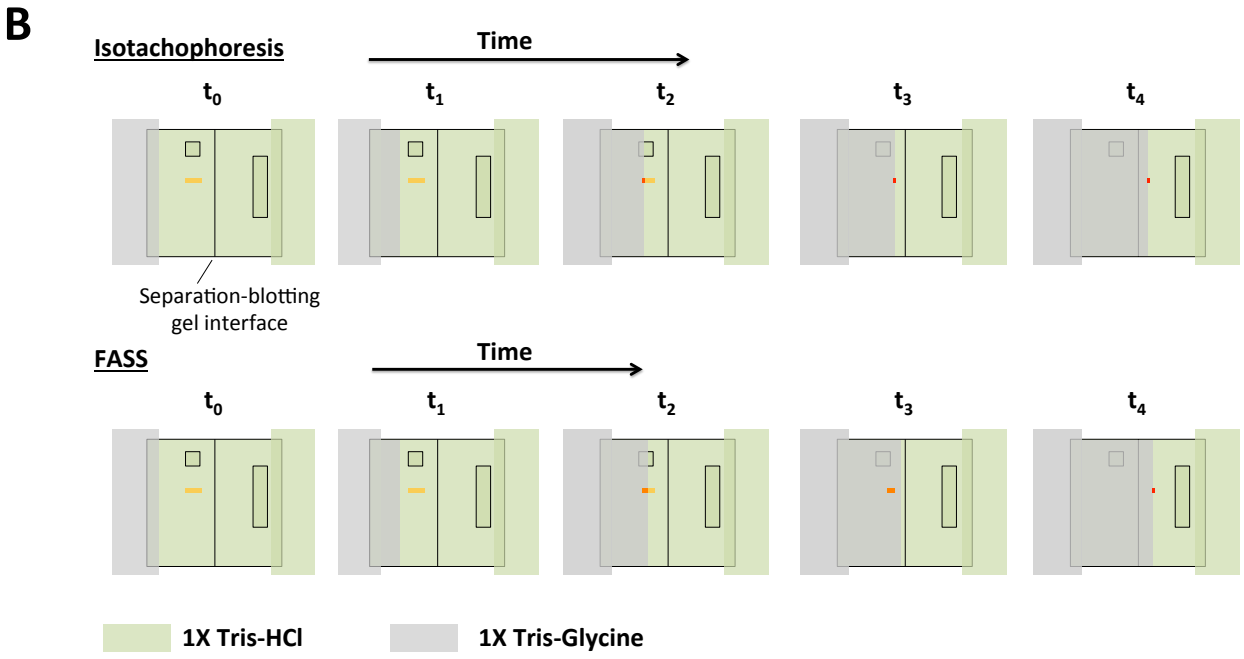

Figure 6.1 *fs*PAGWB enables rapid western blot analysis of protein samples. The aspects of scale and device structure are illustrated. (A) The *fs*PAGWB workflow is comprised of: 1) Loading the well in separation PAG with protein sample analytes solution and the well in blotting BPMA PAG with SDS-PAGE run buffer. 2) Perform SDS-PAGE separation of protein samples. 3) Exchange the run buffer with tris-HCl buffer and initiate ITP/FASS analytes transfer. Proteins are UV-captured onto the gel matrix once they arrived at blotting gel. 4) Uncaptured proteins were removed and introduction of primary antibody and fluorescently secondary antibody specific to the target protein analytes reveal the location and immuno-identities of the target analytes. (B) Protein migration in ITP and FASS. For ITP, the Cl^-/glycine interface sandwich and concentrates the protein analytes. ITP continues in blotting gel. For FASS, protein analytes fall behind the Cl^-/glycine interface and get partially concentrated. As the protein migrate into blotting gel, ITP conditions is re-established and protein over the interface and get sandwiched and concentrated at Cl^-/glycine interface.

	Isotachophoresis	FASS	Uniform buffer electrophoresis
Leading electrolytes/ions	Tris-HCl/Cl^-	Tris-HCl/Cl^-	Uniform buffer
Trailing electrolytes/ions	Tris-Glycine/Glycine	Tris-Glycine/Glycine	
Mobility relationship	Cl^- > target protein>glycine	Cl^- > glycine> target protein	N/A
What's at interface	Target protein stacked between Cl^- and glycine	Target protein behind Cl^-/glycine interface	No interface

Table 6.1 Comparison of three electrophoresis modes: Isotachophoresis (ITP), field-amplified sample stacking (FASS) and uniform buffer electrophoresis in terms of electrolytes composition, mobility relationship and interface properties.

6.3.1 Stage 1 —— Sample loading optimization and SDS-PAGE

To seek broader relevance in life science application, we adapted part of the electrophoresis condition from the well-known Laemmli buffer system[139,140] —— the use of transient ITP to preconcentrate the protein sample. To do so, the protein samples were prepared in 1% SDS, 0.05 mM Tris-HCl buffer and *fs*PAGWB device were immersed in tris-glycine buffer to create a buffer ion discontinuity across the edges of the sample well. Upon initiation of electrophoresis, the rear-stacking interface quickly overtook the front-diffusional interface and the protein sample got concentrated and moved into the gel. After the rear interface collapsed with the front interface, transient ITP terminated and transitioned into SDS-PAGE and proteins separated according to their molecular weights. Figure 6.2 illustrates the progression of transient ITP and subsequent migration with TI*.

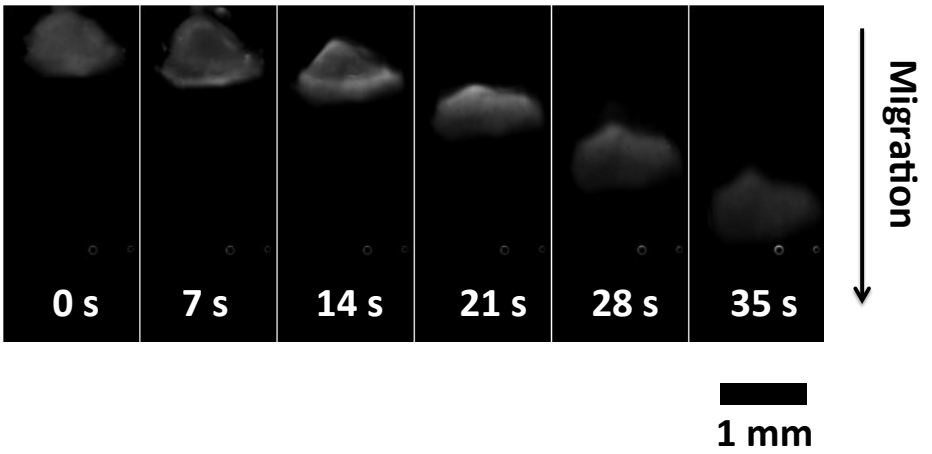

Figure 6.2 The progression of transient ITP followed by SDS-PAGE. A front-diffusional interface and rear-stacking interface form upon electrophoresis, as is evidenced in 14 seconds. The two interfaces collapses and transient ITP transits into SDS-PAGE mode.

Unlike the in-chip PAGE system where the gel geometry is defined by the size of the glass channel, *fs*PAGE introduces extra injection dispersion due to the presence of sample well. Two sources contribute to the increased dispersion. 1) A "standby time" exists between sample loading on gel and the starting of electrophoresis. Lateral (transverse) diffusion of sample proteins from the well into the gel during "standby time" could contribute to "side tails" of main band as they migrate slower due to the fact they start in gel. 2) The nature of fabrication (molding or photo-patterning) could cause serrated edges of the well, and results in "tailing" effect similar to that described in (1). The two sources are illustrated in Figure 6.3A.

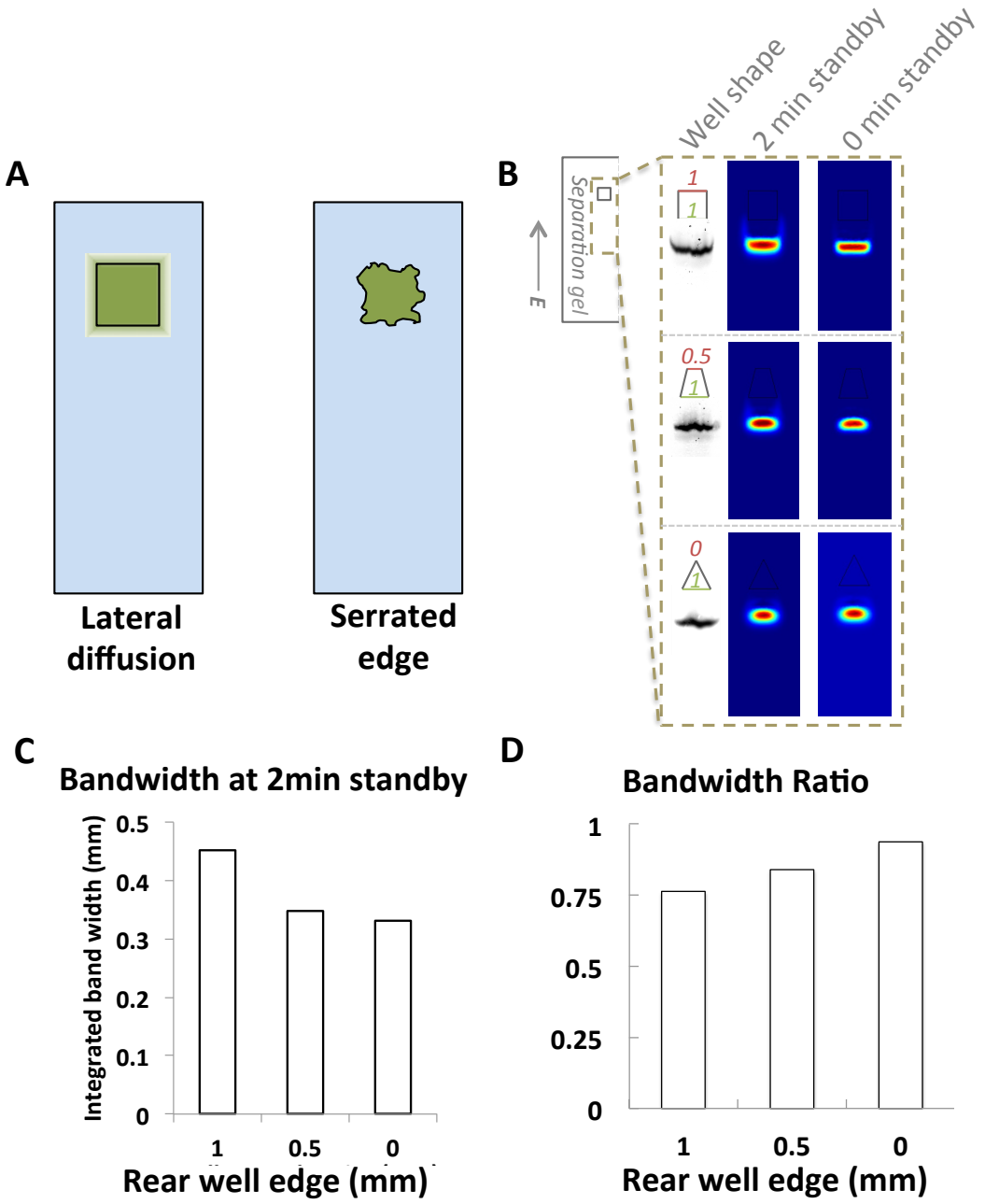

Figure 6.3 Extra injection dispersion introduced by *fs*PAGWB and well shape optimization. (A) Schematics showing two sources for extra injection dispersion. Both lateral diffusion and serrated well edge contribute to the band tailing effects. (B) Comsol® simulation results of lateral diffusion at a standby time of 2 minutes. Three well shapes were evaluated. The upper right diagram plots the integrated bandwidths of 3 well shapes from simulation results. The bottom right diagram compares the bandwidth ratio of integrated bandwidths between 0 minutes and 2 minutes standby time. (C) Integrated bandwidth from simulation results at 2 minutes standby time. (D) Bandwidth ratio from simulation results between 0 and 2 minutes standby time.

To overcome the design defects, we sought to decrease the injection dispersion with well shape optimization. In particular, we reduced the size of the rear edge of the well so that proteins "protruded" into the gel can quickly go back to the well, so as to effectively remove the extra dispersion. Figure 6.3B shows the numerical simulation results of bandwidths with Comsol®. In the simulation, the standard mass transport equation was used (See equation 4 in Chapter 1). Protein concentration was set to 100 nM in the well and 0 nM elsewhere in the gel body as the initial conditions. 50 V/cm was used for electrophoretic separation. For all gel boundaries, no-flux conditions were applied. The bandwidth was calculated by integrating the "intensity value" in the transverse direction. Here, we focused on lateral diffusion effects and tested 3 rear edge sizes of 1, 0.5 and 0 mm (front edge maintained at 1 mm). It is clear from Figure 6.3B that the band "tailing" effect was minimized with reduced well rear edge and we found the integrated bandwidth at 2 minute of "standby time" decreased with rear well edge (Figure 6.3C). Additionally, to evaluate the amount of lateral diffusion counteracted by shape optimization, we compared the band geometry for a "standby time" of 0 and 2 minutes (a typical standby time for *fs*PAGE implementation) for each well shape. We took the bandwidth ratio between 0 minute and 2 minute (Figure 6.3D). We found the value increases with decreased rear edge length and approached 1 for 0 mm, indicating reducing the rear edge helps offset the lateral diffusional effects and lowers the integrated band width, therefore decreasing the injection dispersion.

We next sought to confirm that the separation mechanism of proteins is dictated by the molecular mass difference, as verified through the Fergusen relationship[141]. Figure 6.4 shows the SDS-PAGE separation of a protein ladder of TI* (21 kDa), BSA* (66.5 kDa), β-gal (116 kDa) and FN* (220 kDa). The separation yielded a log-linear relationship between the molecular mass and migration distance over a wide range of 20-220 kDa, which suggests proteins sizing (SDS-PAGE) is the dominant mechanism.

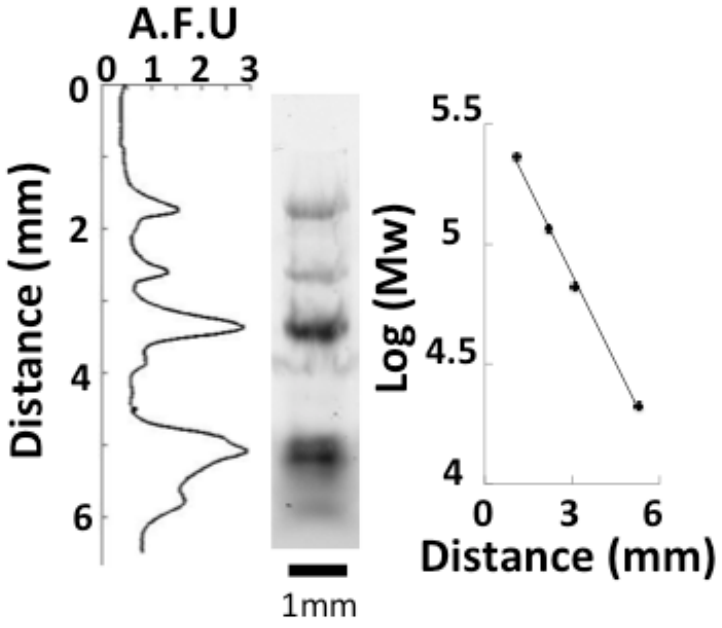

Figure 6.4 SDS-PAGE protein separation with *fs*PAGWB. Log-linear plots of marker protein ladder molecular weight (Mw) versus migration distance. (Protein ladder used were TI*, 21 kDa, BSA*, 66.5 kDa, β-gal, 116 kDa and FN*, 220 kDa).

6.3.2 Stage 2 —— Protein transfer

In the next step, the separated proteins were transferred to the blotting BPMA gel, in a direction perpendicular to the separation axis (see Figure 6.1A). During the transfer step, we leveraged common electrophoretic stacking mechanisms —— ITP and FASS to concentrate the sample to enhance the sensitivity. Prior to transfer, a buffer exchange was performed to replace the tris-glycine run buffer with a more conductive tris-HCl buffer. Then, two pieces of electrode wicks saturated with Tris-Glycine buffer were aligned on two sides of the gel (see Figure 6.1B). Figure 6.5A shows the lateral transfer of a protein ladder (BSA*-FN*). Upon initiation of electrophoresis, a discontinuous electric field distribution was established in the system. According to the Ohm's law, the electrophoretic mobility of each anion follows equation 1.

$$I = E\sigma = E\sum_{i} Fc_i\mu_i \quad (1)$$

In equation 1, I is the current density and σ denotes the total conductivity of each buffer which equals the sum of the conductivity of each component ions. c_i and μ_i are the concentrations and electrophoretic mobilities of each ions. The 50 mM Tris-HCl has a higher conductivity than 1X the Tris-Glycine buffer and consequently the gel body in Tris-HCl experienced lower electric field than the electrode wicks in Tris-Glycine, and therefore the proteins migrated with negligible velocities. These analytes remain quasi-static until hit by the upcoming interface of glycine/Cl^-. For a normal sized protein (<100 kDa), the following electrophoretic mobility relationship holds in separation gel (7-8%T PAG): $\mu_{glycine} < \mu_{protein} < \mu_{Cl}$, and this circumstance an ITP condition is established at the interface that swept the analytes towards the blotting gel. For larger protein (>100 kDa), $\mu_{protein} < \mu_{glycine}$, FASS happened instead of ITP where protein analytes still concentrated yet fell behind the interface. In FASS mode, as soon as the large protein hit the separation-blotting gel interface, they gained mobility (in bloting gel, $\mu_{glycine} < \mu_{protein} < \mu_{Cl}$) and overtook the migrating glycine/Cl^- interface and ITP condition was established (See Figure 6.5B for details). Once all protein concentrated and migrated in ITP mode, the electrophoresis was terminated and the assay proceeded to the next stage —— photocapturing and immunoblotting. For these considerations, the blotting gel was made with lower density than separation gels (typically 4-5%T). For the BSA*-FN* ladder, BSA* (66.5 kDa) migrated with ITP at all times while FN* (220 kDa) started with FASS (see 80 seconds in Figure 6.5A) and transitioned into ITP once in blotting gel (see 110 seconds). Figure 6.6A shows the distribution of protein ladder (FN*-βgal*-BSA*-TI*) after a successful transfer.

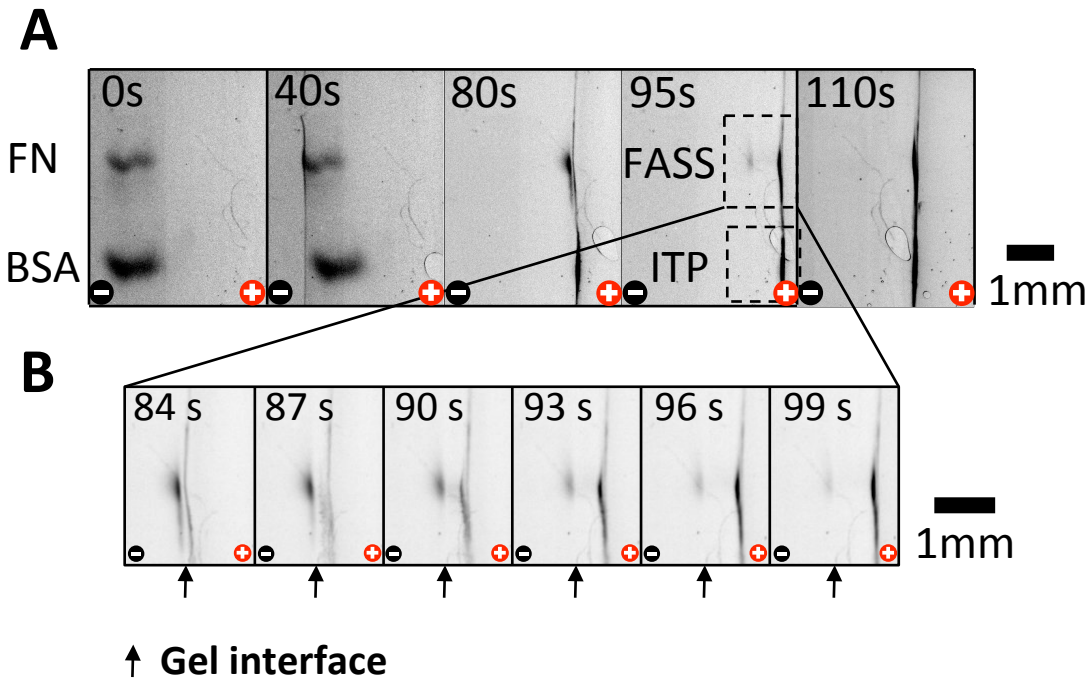

Figure 6.5 Transfer of FN*-BSA* from separation gel to blotting gel. (A) Difference between ITP and FASS mode transfer is shown. For smaller protein BSA (66.5 kDa), ITP dominated the entire transfer process. Larger protein FN* (220 kDa) migrated in FASS mode in separation gel and transitioned into ITP in blotting gel. (B) A zoom-up view of FN* transferring in FASS mode from 84 to 99 seconds. At 84 seconds, FN* migrated in separation gel and fell behind the Cl^-/Glycine interface (the dark line). At 90 seconds, FN* hit the gel interface and quickly gained mobility and overtook the Cl^-/Glycine and got stacked between Cl^- and glycine. ITP resumed at this point. Absolute mobility of FN in blotting gel was difficult to quantify due the quick flush of analytes toward the Cl^-/Glycine interface. Up-arrow indicates the gel interface. The electric-field applied in this step is 50 V/cm.

For these considerations, a complete buffer exchange is critical for a successful ITP/FASS implementation on gel. To perform the buffer exchange, the post-separation gel originally saturated with SDS tris-glycine buffer was immersed in the Tris-HCl. To reduce the protein diffusional loss during this step, we studied and optimized the buffer immersion duration required to complete the ion exchange. Figure 6.6B plots the conductivity (current) change of PAG after a certain period of buffer immersion time. As can be seen from the plot, buffer exchange approximately completed in 1 minute. To illustrate the protein loss after 1 minute of buffer exchange, Figure 6.6C plotted the protein retaining percentage after the buffer immersion. We found smaller proteins displayed less retaining percentage than the large proteins as a result of their higher diffusivities. Specifically, we observed retention of 100% for FN*. In conclusion, 1 minute buffer exchange would fully replace the ions in gel body while retaining >40% for the smallest protein (TI) and ~100% for large protein (FN*) used in measurements. Despite the 40% on the lower end of the ladder range, we consider this

condition sufficient for WB assay as subsequent concentration would enhance the detection sensitivity.

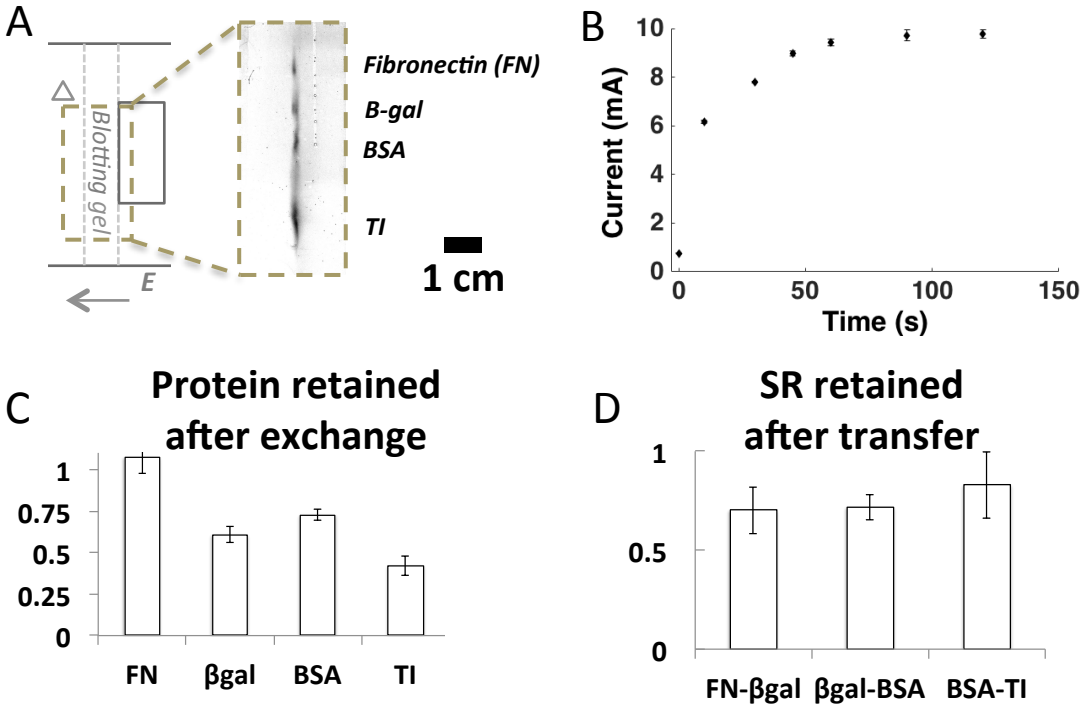

Figure 6.6 Characterization of the protein transfer step. (A) Protein ladder distribution after ITP/FASS transfer. (B) Current monitoring of buffer exchange where electrical current is a proxy for conductivity thus indicating the degree of buffer exchange. Date was averaged from 3 experiments. (C) Diagram showing the amount of protein retained after buffer exchange. (D) Diagram showing separation resolution after transfer.

In addition to the implementation of sample transfer stacking, it is also important to check the separation resolution retaining from that achieved in stage 1, as band broadening during transfer step could reduce the separation performance. To do so we plotted separation resolution (SR) retaining percentage after analytes transfer for all protein pairs in figure 6.6D. We observed retention of 70% of the SR for all pairs. This value informs selection of the separation duration in order to keep all protein pairs distinguishable after transfer/immunoblot.

6.3.3 Stage —— Immunoprobing

UV photocatpure was performed right after transfer according to previously published protocol[40]. After protein immobilization, the *fs*PAGWB device was placed in tris-glycine buffer followed by gentle electrophoretic washing to remove the uncaptured proteins in the signal retained after washing). In *fs*PAGWB, we observed >70% capture efficiencies for all proteins, with the capture efficiency reaching ~100% for FN*.

In final stage of the assay, we introduced immunoprobe to fluorescently visualize the sized and immobilized proteins. To overcome the mass transport limit of diffusional probing in conventional western blot and the single cell western blot assay[40] that typically requires hours of incubation, *fs*PAGWB leveraged the open gel structure advantage and used electrophoretic probing. Two-step antibody probing was performed here. Firstly, the primary antibody solution (0.01 μg/μL) was filled in the antibody well in the blotting BPMA gel shown in figure 6.1, and was electrophoretically injected into the gel and swept over the immobilized protein analytes. As pointed out earlier, the blotting gel was designed with low density to facilitate the probe introduction. Too ensure enough contact and reaction time between antibody and antigen, low electric-field (20V/cm) was used in this step. After 10 minutes probing, the *fs*PAGWB device was immersed in the tris-glycine buffer followed by 10 minutes of electrophoretic washing. A secondary antibody probing with the same electrophoretic condition ensued to read out the previous probing results. The antibody probing results are shown in Figure 6.7 with multiplexed analytes probed in *fs*PAGWB.

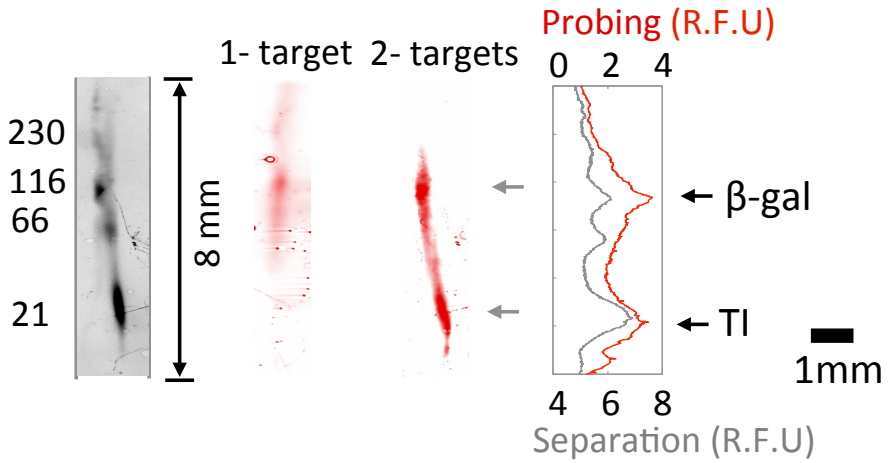

Figure 6.7 Electrophoretic antibody introduction enables fast immunoprobing in *fs*PAGWB. Left, protein ladder distribution after transfer (imaged in 488 channel). 1- and 2-target antibody probing results were compared. For 1- target probing, anti-β-gal primary antibody and Alexa Fluor 555-conjugaged secondary antibody were applied. For 2- target probing, anti-β-gal and anti-TI primary antibody were introduced followed by Alexa Fluor 555-conjugaged secondary antibody. Right, Intensity profile for protein separation (grey) and probing signals (2- targets probing/red) were displayed.

Interestingly, we observed high background signal in the probing step and this is likely due to non-specific antibody adsorption. We hypothesized that the non-specific background was induced by the physical PAG deformation during the ITP transfer step. A possible explanation is that the high electric field gradient at glycine/Cl^- interface caused morphological and physical change to the gel that substantially increased its hydrophobicity, therefore the location of the ionic interface on the gel displayed higher non-specific background after the probing step. A detailed understanding of the gel physical behavior is required to reveal the relationship between PAG ITP and PAG physical property.

6.4 Conclusion

We have demonstrated a rapid, highly sensitive and fully integrated *fs*PAGWB assay that automates the canonical conventional western blot assay and holds great promise for advanced application in wide range of inquiry, from fundamental life science research to clinical diagnostics. The western blot assay here takes up low infrastructure and is made from simple fabrication, while offering fast sizing, enhanced sensitivity with ITP/FASS enabled transferring and exceptionally efficient protein blotting. Compared to slab-gel based and other microfluidic western blot assay, the *fs*PAGWB yields the fastest sample analysis and affords potentially the highest multiplexed format. Table 6.2 summarizes the comparison of a range of specifications of the *fs*PAGWB, µWestern and commercial capillary-based ProteinSimple system[137].

Specifications	***fs*PAGWB**	**µWestern**	**ProteinSimple**
Photo-capture efficiency	>70% for all proteins tested	~70%	N/A
Multiplexity	Up to 96	48	Up to 96
Fabrication time	~30 min	Up to months	N/A
Total run time[1]	35-50 min	60-80 min	3-5 hours
Size range	20~220 kDa	20~150 kDa	12~440 kDa
Sample consumption/unit	~0.01 µg	~0.5 µg	1 µg
Ab Consumption	~10 ng	~1ng	~1 µg
Assay throughput	2 data/min	~0.5 data/min	~0.3-0.5 data/min

Table 6.2 A comparison of system performance of *fs*PAGWB, µWestern and ProteinSimple for WB analysis

Future studies will pursue scale-up of the *fs*PAGWB assay, as well as application to specific questions that will ensure broad relevance. We imagine potential challenges include: reduce non-specific probing signal due to ITP-induced physical hydrogel deformation and efficient buffer patterning on a high-throughput format (96 or 384-plex) gel. Further efforts should aim to resolve these concerns.

Looking forward, the successful integration of disparate western blot steps onto the high-density *fs*PAG format will streamline sample processing presenting an interesting new research topic in quantitative Western blot microarray design. With the unparalleled analytical throughput, the WB microarray could replace the existing protein microarray while adding a crucial step of sizing/separation information to the existing analytical capacity. Further automation with ADE could serve promising relevance for challenging application in system biology, single cell analysis, cancer diagnostics and personal medicine.

Bibliography

(1) Smith, A. J.; Zhang, X.; Leach, A. G.; Houk, K. N. *Journal of medicinal chemistry* **2009**, *52*, 225-233.
(2) Gold, V.; International Union of Pure and Applied Chemistry. *Compendium of chemical terminology : IUPAC recommendations*; Blackwell Scientific Publications: Oxford Oxfordshire ; Boston, 1987, p viii, 456 p.
(3) Lehninger, A. L.; Nelson, D. L.; Cox, M. M. *Lehninger principles of biochemistry*, 6th ed.; W.H. Freeman: New York, 2013.
(4) Bradbury, A.; Plückthun, A. *Nature News* **2015**, *518*, 27-29.
(5) Walker, J. M.; Rapley, R.; Royal Society of Chemistry (Great Britain). *Molecular biology and biotechnology*, 5th ed.; Royal Society of Chemistry: Cambridge, 2009, p xix, 604 p.
(6) Winkler, W.; Nahvi, A.; Breaker, R. R. *Nature* **2002**, *419*, 952-956.
(7) Karns, K.; Vogan, J. M.; Qin, Q.; Hickey, S. F.; Wilson, S. C.; Hammond, M. C.; Herr, A. E. *Journal of the American Chemical Society* **2013**, *135*, 3136-3143.
(8) Blount, K. F.; Breaker, R. R. *Nature biotechnology* **2006**, *24*, 1558-1564.
(9) Ketzer, P.; Kaufmann, J. K.; Engelhardt, S.; Bossow, S.; von Kalle, C.; Hartig, J. S.; Ungerechts, G.; Nettelbeck, D. M. *P Natl Acad Sci USA* **2014**, *111*, E554-E562.
(10) Regulski, E. E.; Breaker, R. R. *Methods in molecular biology* **2008**, *419*, 53-67.
(11) Blount, K.; Puskarz, I.; Penchovsky, R.; Breaker, R. *RNA biology* **2006**, *3*, 77-81.
(12) Mayer, G.; Famulok, M. *Chembiochem : a European journal of chemical biology* **2006**, *7*, 602-604.
(13) Gilbert, S. D.; Rambo, R. P.; Van Tyne, D.; Batey, R. T. *Nature structural & molecular biology* **2008**, *15*, 177-182.
(14) Maizel, J. V. *Trends in biochemical sciences* **2000**, *25*, 590-592.
(15) Hellman, L. M.; Fried, M. G. *Nature protocols* **2007**, *2*, 1849-1861.
(16) Bao, J. J. *Journal of chromatography. B, Biomedical sciences and applications* **1997**, *699*, 463-480.
(17) Michels, D. A.; Tu, A. W.; McElroy, W.; Voehringer, D.; Salas-Solano, O. *Analytical chemistry* **2012**, *84*, 5380-5386.
(18) Chiem, N.; Harrison, D. J. *Analytical chemistry* **1997**, *69*, 373-378.
(19) Altria, K. D. *Methods in molecular biology* **1996**, *52*, 3-13.
(20) Giddings, J. C. *Unified separation science*; Wiley: New York, 1991, p xxiv, 320 p.
(21) Kirby, B.; Cambridge University Press,: New York, 2010, pp 1 online resource (xxiii, 512 p.) ill.
(22) Grunwald, M. E.; Yu, W. P.; Yu, H. H.; Yau, K. W. *The Journal of biological chemistry* **1998**, *273*, 9148-9157.
(23) Park, S. H.; Raines, R. T. *Methods in molecular biology* **2004**, *261*, 155-160.
(24) Perrin, D.; Fremaux, C.; Besson, D.; Sauer, W. H.; Scheer, A. *Journal of biomolecular screening* **2006**, *11*, 996-1004.
(25) Apori, A. A.; Herr, A. E. *Analytical chemistry* **2011**, *83*, 2691-2698.
(26) Weng, X.; Bi, H.; Liu, B.; Kong, J. *Electrophoresis* **2006**, *27*, 3129-3135.
(27) Pan, Y.; Karns, K.; Herr, A. E. *Electrophoresis* **2014**, *35*, 2078-2090.
(28) Reccius, C. H.; Stavis, S. M.; Mannion, J. T.; Walker, L. P.; Craighead, H. G. *Biophysical journal* **2008**, *95*, 273-286.

(29) Hou, C.; Herr, A. E. *Electrophoresis* **2008**, *29*, 3306-3319.
(30) Chiem, N. H.; Harrison, D. J. *Electrophoresis* **1998**, *19*, 3040-3044.
(31) Qiu, C. X.; Harrison, D. J. *Electrophoresis* **2001**, *22*, 3949-3958.
(32) Cheng, S. B.; Skinner, C. D.; Taylor, J.; Attiya, S.; Lee, W. E.; Picelli, G.; Harrison, D. J. *Analytical chemistry* **2001**, *73*, 1472-1479.
(33) Huang, Y.; Shi, M.; Zhao, S.; Liang, H. *Electrophoresis* **2011**, *32*, 3196-3200.
(34) Huang, Y.; Zhao, S.; Shi, M.; Liu, Y. M. *Analytical biochemistry* **2010**, *399*, 72-77.
(35) Zhao, S.; Liu, Y. M. *Methods in molecular biology* **2013**, *919*, 79-85.
(36) Huang, Y.; Zhao, S.; Shi, M.; Liu, J.; Liang, H. *Analytica chimica acta* **2011**, *694*, 162-166.
(37) Schmalzing, D.; Koutny, L. B.; Taylor, T. A.; Nashabeh, W.; Fuchs, M. *Journal of Chromatography B: Biomedical Sciences and Applications* **1997**, *697*, 175-180.
(38) Chuang, Y. J.; Huang, J. W.; Makamba, H.; Tsai, M. L.; Li, C. W.; Chen, S. H. *Electrophoresis* **2006**, *27*, 4158-4165.
(39) Clark, J.; Shevchuk, T.; Swiderski, P. M.; Dabur, R.; Crocitto, L. E.; Buryanov, Y. I.; Smith, S. S. *BioTechniques* **2003**, *35*, 548-554.
(40) Hughes, A. J.; Spelke, D. P.; Xu, Z. C.; Kang, C. C.; Schaffer, D. V.; Herr, A. E. *Nat Methods* **2014**, *11*, 749-U794.
(41) Bromberg, A.; Mathies, R. A. *Electrophoresis* **2004**, *25*, 1895-1900.
(42) Edwards, A. L., Batey, R. T. . *Nature Education* **2010**, *3*, 9.
(43) Hammann, C.; Westhof, E. *Genome biology* **2007**, *8*, 210.
(44) Tucker, B. J.; Breaker, R. R. *Current opinion in structural biology* **2005**, *15*, 342-348.
(45) Henkin, T. M. *Genes & development* **2008**, *22*, 3383-3390.
(46) Heppell, B.; Mulhbacher, J.; Penedo, J. C.; Lafontaine, D. A. *Methods in molecular biology* **2009**, *540*, 25-37.
(47) Wickiser, J. K.; Winkler, W. C.; Breaker, R. R.; Crothers, D. M. *Molecular cell* **2005**, *18*, 49-60.
(48) Sudarsan, N.; Lee, E. R.; Weinberg, Z.; Moy, R. H.; Kim, J. N.; Link, K. H.; Breaker, R. R. *Science* **2008**, *321*, 411-413.
(49) Lee, E. R.; Baker, J. L.; Weinberg, Z.; Sudarsan, N.; Breaker, R. R. *Science* **2010**, *329*, 845-848.
(50) Kellenberger, C. A.; Sales-Lee, J.; Pan, Y.; Gassaway, M. M.; Herr, A. E.; Hammond, M. C. *RNA biology* **2015**, *12*, 1189-1197.
(51) Weinberg, Z.; Barrick, J. E.; Yao, Z.; Roth, A.; Kim, J. N.; Gore, J.; Wang, J. X.; Lee, E. R.; Block, K. F.; Sudarsan, N.; Neph, S.; Tompa, M.; Ruzzo, W. L.; Breaker, R. R. *Nucleic acids research* **2007**, *35*, 4809-4819.
(52) Weinberg, Z.; Breaker, R. R. *BMC bioinformatics* **2011**, *12*, 3.
(53) Weinberg, Z.; Wang, J. X.; Bogue, J.; Yang, J.; Corbino, K.; Moy, R. H.; Breaker, R. R. *Genome biology* **2010**, *11*, R31.
(54) Hickey, S. F.; Hammond, M. C. *Chemistry & biology* **2014**, *21*, 345-356.
(55) Roth, A.; Winkler, W. C.; Regulski, E. E.; Lee, B. W.; Lim, J.; Jona, I.; Barrick, J. E.; Ritwik, A.; Kim, J. N.; Welz, R.; Iwata-Reuyl, D.; Breaker, R. R. *Nature structural & molecular biology* **2007**, *14*, 308-317.
(56) Yan, Y.; Marriott, G. *Curr Opin Chem Biol* **2003**, *7*, 635-640.

(57) Choi, J. W.; Kang, D. K.; Park, H.; deMello, A. J.; Chang, S. I. *Analytical chemistry* **2012**, *84*, 3849-3854.
(58) Srisa-Art, M.; Kang, D. K.; Hong, J.; Park, H.; Leatherbarrow, R. J.; Edel, J. B.; Chang, S. I.; deMello, A. J. *Chembiochem : a European journal of chemical biology* **2009**, *10*, 1605-1611.
(59) Garner, M. M.; Revzin, A. *Nucleic acids research* **1981**, *9*, 3047-3060.
(60) Cann, J. R. *Analytical biochemistry* **1996**, *237*, 1-16.
(61) Woodson, S. A.; Koculi, E. *Methods in enzymology* **2009**, *469*, 189-208.
(62) Kulshina, N.; Baird, N. J.; Ferre-D'Amare, A. R. *Nature structural & molecular biology* **2009**, *16*, 1212-1217.
(63) Stebbins, M. A.; Hoyt, A. M.; Sepaniak, M. J.; Hurlburt, B. K. *Journal of chromatography. B, Biomedical applications* **1996**, *683*, 77-84.
(64) Paige, J. S.; Nguyen-Duc, T.; Song, W.; Jaffrey, S. R. *Science* **2012**, *335*, 1194.
(65) Dixon, N.; Duncan, J. N.; Geerlings, T.; Dunstan, M. S.; McCarthy, J. E.; Leys, D.; Micklefield, J. *Proc Natl Acad Sci U S A* **2010**, *107*, 2830-2835.
(66) Strobel, B.; Klauser, B.; Hartig, J. S.; Lamla, T.; Gantner, F.; Kreuz, S. *Molecular therapy : the journal of the American Society of Gene Therapy* **2015**, *23*, 1582-1591.
(67) Romling, U.; Galperin, M. Y.; Gomelsky, M. *Microbiology and molecular biology reviews : MMBR* **2013**, *77*, 1-52.
(68) Spangler, C.; Bohm, A.; Jenal, U.; Seifert, R.; Kaever, V. *Journal of microbiological methods* **2010**, *81*, 226-231.
(69) Stelitano, V.; Brandt, A.; Fernicola, S.; Franceschini, S.; Giardina, G.; Pica, A.; Rinaldo, S.; Sica, F.; Cutruzzola, F. *Nucleic acids research* **2013**, *41*, e79.
(70) Christen, M.; Kulasekara, H. D.; Christen, B.; Kulasekara, B. R.; Hoffman, L. R.; Miller, S. I. *Science* **2010**, *328*, 1295-1297.
(71) Ho, C. L.; Chong, K. S.; Oppong, J. A.; Chuah, M. L.; Tan, S. M.; Liang, Z. X. *Journal of the American Chemical Society* **2013**, *135*, 566-569.
(72) Kellenberger, C. A.; Wilson, S. C.; Sales-Lee, J.; Hammond, M. C. *Journal of the American Chemical Society* **2013**, *135*, 4906-4909.
(73) Nakayama, S.; Luo, Y.; Zhou, J.; Dayie, T. K.; Sintim, H. O. *Chemical communications* **2012**, *48*, 9059-9061.
(74) Wilson, S. C.; Cohen, D. T.; Wang, X. C.; Hammond, M. C. *Rna* **2014**, *20*, 1153-1160.
(75) Baba, T.; Ara, T.; Hasegawa, M.; Takai, Y.; Okumura, Y.; Baba, M.; Datsenko, K. A.; Tomita, M.; Wanner, B. L.; Mori, H. *Molecular systems biology* **2006**, *2*, 2006 0008.
(76) Weber, H.; Pesavento, C.; Possling, A.; Tischendorf, G.; Hengge, R. *Molecular microbiology* **2006**, *62*, 1014-1034.
(77) Pesavento, C.; Becker, G.; Sommerfeldt, N.; Possling, A.; Tschowri, N.; Mehlis, A.; Hengge, R. *Genes & development* **2008**, *22*, 2434-2446.
(78) Mayer, G.; Raddatz, M. S. L.; Grunwald, J. D.; Famulok, M. *Angew Chem Int Edit* **2007**, *46*, 557-560.
(79) Luo, Y.; Chen, B.; Zhou, J.; Sintim, H. O.; Dayie, T. K. *Molecular bioSystems* **2014**, *10*, 384-390.
(80) Ferrance, J.; Landers, J. P. *Luminescence : the journal of biological and chemical luminescence* **2001**, *16*, 79-88.
(81) Ross, D.; Kralj, J. G. *Analytical chemistry* **2008**, *80*, 9467-9474.

(82) Emrich, C. A.; Tian, H.; Medintz, I. L.; Mathies, R. A. *Analytical chemistry* **2002**, *74*, 5076-5083.
(83) Gaunt, T. R.; Hinks, L. J.; Rassoulian, H.; Day, I. N. M. *Nucleic acids research* **2003**, *31*.
(84) Gutzkow, K. B.; Langleite, T. M.; Meier, S.; Graupner, A.; Collins, A. R.; Brunborg, G. *Mutagenesis* **2013**, *28*, 333-340.
(85) Wood, D. K.; Weingeist, D. M.; Bhatia, S. N.; Engelward, B. P. *P Natl Acad Sci USA* **2010**, *107*, 10008-10013.
(86) Watson, C.; Ge, J.; Cohen, J.; Pyrgiotakis, G.; Engelward, B. P.; Demokritou, P. *ACS nano* **2014**, *8*, 2118-2133.
(87) Duncombe, T. A.; Herr, A. E. *Lab Chip* **2013**, *13*, 2115-2123.
(88) Wilson, S. C.; Cohen, D. T.; Wang, X. C.; Hammond, M. C. *RNA* **2014**.
(89) Duncombe, T. A.; Herr, A. E. *Analytical chemistry* **2012**, *84*, 8740-8747.
(90) Herr, A. E.; Singh, A. K. *Analytical chemistry* **2004**, *76*, 4727-4733.
(91) Hughes, A. J.; Lin, R. K.; Peehl, D. M.; Herr, A. E. *Proc Natl Acad Sci U S A* **2012**, *109*, 5972-5977.
(92) Pan, Y.; Duncombe, T. A.; Kellenberger, C. A.; Hammond, M. C.; Herr, A. E. *Analytical chemistry* **2014**, *86*, 10357-10364.
(93) Stull, D. R. *Ind Eng Chem* **1947**, *39*, 517-540.
(94) Trevoy, D. J. *Ind Eng Chem* **1953**, *45*, 2366-2369.
(95) Pennings, S.; Meersseman, G.; Bradbury, E. M. *Nucleic Acids Res* **1992**, *20*, 6667-6672.
(96) Hu, C. T.; O'Shaughnessy, K. M. *Electrophoresis* **2001**, *22*, 1063-1068.
(97) Smith, K. D.; Lipchock, S. V.; Ames, T. D.; Wang, J.; Breaker, R. R.; Strobel, S. A. *Nature structural & molecular biology* **2009**, *16*, 1218-1223.
(98) Pan, Y.; Karns, K.; Herr, A. E. *Electrophoresis* **2014**.
(99) Duncombe, T. A.; Kang, C. C.; Maity, S.; Ward, T. M.; Pegram, M. D.; Murthy, N.; Herr, A. E. *Adv Mater* **2016**, *28*, 327-334.
(100) Walton, D. E. *Drying Technology* **2004**, *22*, 431-456.
(101) Dunn, D. A.; Feygin, I. *Drug discovery today* **2000**, *5*, 84-91.
(102) Reichman, M.; Harris, A. L. In *Annual Reports in Combinatorial Chemistry and Molecular Diversity*; Springer, 1997, pp 273-286.
(103) Cleveland, P. H.; Koutz, P. J. *Assay Drug Dev Techn* **2005**, *3*, 213-225.
(104) Wood, R. W.; Loomis, A. L. *The London, Edinburgh, and Dublin philosophical magazine and journal of science* **1927**, *4*, 417-436.
(105) Hadimioglu, B.; Stearns, R.; Ellson, R. *Journal of laboratory automation* **2016**, *21*, 4-18.
(106) Sackmann, E. K.; Majlof, L.; Hahn-Windgassen, A.; Eaton, B.; Bandzava, T.; Daulton, J.; Vandenbroucke, A.; Mock, M.; Stearns, R. G.; Hinkson, S. *Journal of laboratory automation* **2015**, 2211068215602191.
(107) Sternberger, L. A.; Hardy, P. H., Jr.; Cuculis, J. J.; Meyer, H. G. *The journal of histochemistry and cytochemistry : official journal of the Histochemistry Society* **1970**, *18*, 315-333.
(108) Jefferis, R. *Trends in pharmacological sciences* **2009**, *30*, 356-362.
(109) Kariolis, M. S.; Kapur, S.; Cochran, J. R. *Current opinion in biotechnology* **2013**, *24*, 1072-1077.
(110) Goding, J. W. *Journal of immunological methods* **1980**, *39*, 285-308.

(111) Birch, J. R.; Racher, A. J. *Advanced drug delivery reviews* **2006**, *58*, 671-685.
(112) Polakiewicz, R. D. *Nature* **2015**, *518*, 483-483.
(113) Bordeaux, J.; Welsh, A. W.; Agarwal, S.; Killiam, E.; Baquero, M. T.; Hanna, J. A.; Anagnostou, V. K.; Rimm, D. L. *BioTechniques* **2010**, *48*, 197.
(114) Friguet, B.; Chaffotte, A. F.; Djavadi-Ohaniance, L.; Goldberg, M. E. *Journal of immunological methods* **1985**, *77*, 305-319.
(115) Schuck, P. *Current opinion in biotechnology* **1997**, *8*, 498-502.
(116) Hardy, F.; Djavadi-Ohaniance, L.; Goldberg, M. E. *Journal of immunological methods* **1997**, *200*, 155-159.
(117) Karlsson, R.; Falt, A. *Journal of immunological methods* **1997**, *200*, 121-133.
(118) Gauglitz, G. *Analytical and bioanalytical chemistry* **2010**, *398*, 2363-2372.
(119) Waldmann-Meyer, H. *The Journal of biological chemistry* **1960**, *235*, 3337-3345.
(120) Goodrich, J. A.; Kugel, J. F. *Binding and kinetics for molecular biologists*; Cold Spring Harbor Laboratory Press: Cold Spring Harbor, N.Y., 2007, p x, 182 p.
(121) Rippel, G.; Corstjens, H.; Billiet, H. A.; Frank, J. *Electrophoresis* **1997**, *18*, 2175-2183.
(122) Bromberg, A.; Mathies, R. A. *Electrophoresis* **2004**, *25*, 1895-1900.
(123) Kang, C.-C.; Lin, J.-M. G.; Xu, Z.; Kumar, S.; Herr, A. E. *Analytical chemistry* **2014**, *86*, 10429-10436.
(124) Hornsby, M.; Paduch, M.; Miersch, S.; Sääf, A.; Matsuguchi, T.; Lee, B.; Wypisniak, K.; Doak, A.; King, D.; Usatyuk, S. *Molecular & Cellular Proteomics* **2015**, *14*, 2833-2847.
(125) Tao, L.; Kennedy, R. T. *Electrophoresis* **1997**, *18*, 112-117.
(126) Ou, J. P.; Wang, Q. G.; Cheung, T. M.; Chan, S. T. H.; Yeung, W. S. B. *J Chromatogr B* **1999**, *727*, 63-71.
(127) Heegaard, N. H. H. *Electrophoresis* **2009**, *30*, S229-S239.
(128) Yin, L.; Wang, W.; Wang, S.; Zhang, F.; Zhang, S.; Tao, N. *Biosensors & bioelectronics* **2015**, *66*, 412-416.
(129) Kapil, M. A.; Pan, Y.; Duncombe, T. A.; Herr, A. E. *Analytical chemistry* **2016**, *88*, 3669-3676.
(130) Iweala, O. I. *Contraception* **2004**, *70*, 141-147.
(131) Kurien, B. T.; Scofield, R. H. *Protein blotting and detection : methods and protocols*; Humana Press: New York, 2009, p xiii, 588 p.
(132) Mahmood, T.; Yang, P. C. *North American journal of medical sciences* **2012**, *4*, 429-434.
(133) Ciaccio, M. F.; Wagner, J. P.; Chuu, C. P.; Lauffenburger, D. A.; Jones, R. B. *Nat Methods* **2010**, *7*, 148-155.
(134) Yeh, H. Y.; Serrano, K. V.; Acosta, A. S.; Buhr, R. J. *Journal of microbiological methods* **2016**, *122*, 27-32.
(135) Markely, L. R.; Cheung, L.; Choi, Y. J.; Ryll, T.; Estes, S.; Prajapati, S.; Turyan, I.; Frenkel, R.; Sosic, Z.; Lambropoulos, J.; Tescione, L.; Ryll, T.; Berman, M. *Biotechnology progress* **2016**, *32*, 235-241.
(136) Kim, D.; Karns, K.; Tia, S. Q.; He, M.; Herr, A. E. *Analytical chemistry* **2012**, *84*, 2533-2540.
(137) Hughes, A. J.; Herr, A. E. *P Natl Acad Sci USA* **2012**, *109*, 21450-21455.
(138) Hughes, A. J.; Lin, R. K. C.; Peehl, D. M.; Herr, A. E. *P Natl Acad Sci USA* **2012**, *109*, 5972-5977.

(139) Ornstein, L. *Annals of the New York Academy of Sciences* **1964**, *121*, 321-349.
(140) Laemmli, U. K. *Nature* **1970**, *227*, 680-685.
(141) Ferguson, K. A. *Metabolism: clinical and experimental* **1964**, *13*, SUPPL:985-1002.

Appendices

Appendix A: Thermal model of the open architecture of *fs*PAG structure

To aid the thermal analysis of the *fs*PAG structure, we established its thermal model here that detailed the heat generation and transfer in *fs*PAGE.
The heat balance in *fs*PAGE is quantitatively described by equation 1:

$$\frac{U^2}{l^2}\sigma H = \dot{q}_C + \dot{q}_E \tag{1}$$

Where U is the applied voltage, l, H are the length and height of *fs*PAG, σ is the conductivity of buffer in gel, $\dot{q}_C$ is the heat loss via convection and $\dot{q}_E$ is the heat loss via evaporation. Further, heat convection is given by equation 2:

$$\dot{q}_C = (T_g - T_a)k_h \tag{2}$$

in which T_g and T_a are the gel and ambient temperatures, and k_h is the heat convection coefficient. In addition, heat loss via evaporation can be approached with Langmuir's evaporation model:

$$\dot{q}_E = \Delta H_{vap}(P_v - P_p)\sqrt{\frac{m}{2\pi k T_g}} \tag{3}$$

in which ΔH_{vap} is the vaporization enthalpy of the liquid, P_v is the vapor pressure of liquid as a function of temperature, P_p is the partial pressure of the vapor in the gas, m is the vapor molecule mass and k is the Boltzmann constant. Next, we approach P_v (in bar) with the Antoine equation and write:

$$P_v = exp\left(A - \frac{B}{C + T_g}\right) \tag{4}$$

For water within 0 °C to 99 °C, A=10.72 Pa, B=3304.82 Pa·K and C=-64.85 K.[93]

It is clear seen from equation 2-4 that both $\dot{q}_C$ and $\dot{q}_E$ monotonically increase with T_g. In addition, Eqn 1 shows increasing H increases both $\dot{q}_C$ and $\dot{q}_E$, therefore increases T_g. This relationship states that a taller gel experience higher temperature.

Further, we establish a relationship between moisture evaporation and *fs*PAG height H. To do so, define the relative *fs*PAG moisture loss L, as the amount of water evaporation as a percentage of the total moisture in the gel. L can be expressed as:

$$L = \frac{\dot{q}_E / \Delta H_{vap}}{V \nu \rho} \tag{7}$$

where V is the *fs*PAG volume, ν is the volume fraction of water in *fs*PAG and ρ is the water density. Substituting eqn 1-4 into 7, L is wrote as:

$$L = \frac{U^2 \sigma}{l^3 w \nu \rho \Delta H_{vap}} \cdot \frac{\dot{q}_E}{\dot{q}_C + \dot{q}_E} \tag{8}$$

With some mathematical derivation, it can be seen that the second fraction on the right hand side increases monotonically with T_g. As T_g increases monotonically with *fs*PAG height H, so does L. To conclude, the theoretical analysis of the thermo properties of *fs*PAGE indicates that *fs*PAG with lower height would undergo less relative moisture evaporation, and therefore better electrophoretic stability.

Appendix B: ANOVA analysis of unit-to-unit variation

The migration variation of 96-plex *fs*PAGE described in Section 3.6 is calculated here. The migration distances in each *fs*PAG are listed in Figure B.1.

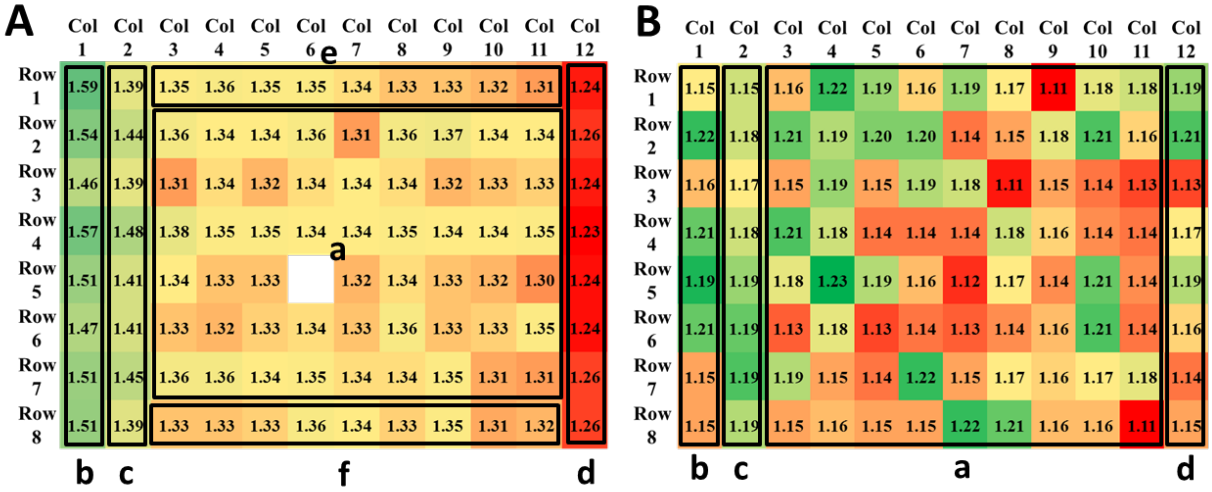

Figure B.1 Matrix of migration distances in 96-plex *fs*PAG shown in Figure 3.6. A and B list the migration distance in mm before and after geometric optimization. The units in the periphery of array are assigned to different group. Group b, c, d, e, f in A and Group b, c, d in B. The central region of the array is assigned to group a. Unit: mm. ([92]Reprinted with permission from Anal. Chem., 2014, 86 (20). High-Throughput Electrophoretic Mobility Shift Assays for Quantitative Analysis of Molecular Binding Reactions)

The ANOVA analysis is performed to test any significance of migration distances between the peripheral groups (b, c, d, e, f in the A and b, c, d in B, Figure B.1) and central array region (a):

It is important to note that the choice of central array group a has to satisfy 2 conditions. (1) There should be no spatial variation in terms of migration distance in group a, that is, columns or rows that have side effects should not be included. (2) Group 2 should contain as many units as possible so as to improve the quality of statistical analysis.

We have found no spatial variation in group a in Figure B.1A (in the same way that we used to seek variation for groups b, c, d, e, f, demonstrated below) and therefore it is chosen to test side effects on the peripheral groups. In Figure B.1B, we extend the region of group a to include both row 1 and 8 as no variation in migration distance is found in them during ANOVA analysis to Figure B.1A.

ANOVA analysis before geometric design optimization (Figure B.1A):

For Col 1 (group b):

The sum of squares (SS) within groups (a+b) SS_w equals the sum of SS in a and SS in b: SS_w= 4.97 mm^2

The total SS of all units in a and b: SS_t= 41.72 mm^2

The SS between groups: SS_b= SS_t-SS_w=36.75 mm^2

Degree of freedom (DOF) within groups: 59.

DOF between groups: 1

Therefore the mean square (MS) within groups: MS_w=0.084 mm^2

MS between groups: MS_b=36.75 mm^2

F_{a-b}= MS_b/ MS_w=437.5≈438

For col 2 (group c):

SS_w=3.63 mm^2, SS_b=7.44 mm^2, DOF_w=59, DOF_b=1, MS_w=0.062 mm^2, MS_b=7.44 mm^2, F_{a-c}=121.

For col 12 (group d):

SS_w=2.65 mm^2, SS_b=9.18 mm^2, DOF_w=59, DOF_b=1, MS_w=0.045 mm^2, MS_b=9.18 mm^2, F_{a-d}=205.

For row 1 (group e):

SS_w=2.88 mm^2, SS_b=0.007 mm^2, DOF_w=60, DOF_b=1, MS_w=0.048 mm^2, MS_b=0.007 mm^2, F_{a-e}=0.14.

For row 8 (group f):

SS_w=2.76 mm^2, SS_b=0.032 mm^2, DOF_w=60, DOF_b=1, MS_w=0.046 mm^2, MS_b=0.032 mm^2, F_{a-f}=0.7.

At a significance level α=0.05, $F_{critical}$~4.00. Therefore, col 1, 2 and 12 (group b, c and d) have significant difference than the central region (group a) in migration distance. Row 1 and 8 (group e and f) have no significant difference than the central region (group a).

ANOVA analysis after geometric design optimization (Figure B.1B):

For Col 1 (group b):

SS_w=10.91 mm^2, SS_b=0.233 mm^2, DOF_w=78, DOF_b=1, MS_w=0.233 mm^2, MS_b=0.14 mm^2, F_{a-b}=1.67.

For Col 2 (group c):

SS_w=10.14 mm^2, SS_b=0.288 mm^2, DOF_w=78, DOF_b=1, MS_w=0.288 mm^2, MS_b=0.13 mm^2, F_{a-c}=2.21.

For Col 12 (group d):

SS_w=10.89 mm^2, SS_b=0.007 mm^2, DOF_w=78, DOF_b=1, MS_w=0.007 mm^2, MS_b=0.14 mm^2, F_{a-d}=0.05.

At a significance level α=0.05, $F_{critical}$~4.00. Therefore, none of the groups have significant difference than the central region group.

Appendix C: Matlab® code for *fs*PAGE separation analysis

We've developed customary Matlab® code for analytes separation on both 1-plex single gel format and 384-plex array format. The 1-plex *fs*PAG code can handle any number of analytes and the 384-plex code particularly solves two analytes separation (used in chapter 4 and 5).

1-plex *fs*PAG code:

The codes reply on an n-peak Gaussian function, which is also included here.

```
% define a n-peak gaussian function. This function will be called by the main function.
%c1 Background noise (for all peaks)
%c2 through cn: peak heights, location and standard deviation (2nd moment)
%                        of all peaks
%n  number of peaks

function F = gaussiann(n,c,xdata)
G=0;
for i=1: floor(n/3)
G=G+c((i-1)*3+2)*exp(-(xdata-c(i*3)).^2/2/(c(i*3+1).^2));
end
F=G+c(1);


% Main function for analyzing the separation of peaks
% The input file should be in image format.

function F=fitngau(n,x)
info = imfinfo(x);   %get information on the width and height of the image
         w = info.Width;
         h = info.Height;
         datam = imread(x);
            for g=1:w                          % to transfer the entire datam into a vector g
               intensity(g)=mean(datam(1:h,g));
            end
        plot(1:w,intensity);          %plot the electropherogram and click to set fitting
parameters.
        disp('please first click on the background value, then peak, two FWMH points for all
peaks');
        hold on;
        [xcoor,ycoor]=ginput(3*n+1);       % click on the graph
        fitpara=zeros(1:n);
        fitpara1=ycoor(1);
        for i=1:floor(n/3)                 % set fitting parameters
           fitpara(i*3-1)=ycoor(i*3-1);
           fitpara(i*3)=xcoor(i*3-1);
           fitpara(i*3+1)=(xcoor(i*3+1)-xcoor(i*3))/2.355;
```

```
        end
            c=lsqcurvefit(@gaussiann, [n,fitpara], 1:w, intensity);     %nonlinear fitting to the
gaussian


peakloc=zeros(1,mod(n,3));peakhei=zeros(1,mod(n,3));peakare=zeros(1,mod(n,3));peaksig=z
eros(1,mod(n,3));
        for i=1:floor(n/3)       %extract the peak value and print the height, location, area and
standard deviation.
        peakloc(i)=c(3*i);
        peakhei(i)=c(3*i-1);
        peakare(i)=c(3*i-1)*c(3*i+1)/0.3989;
        peaksig(i)=c(3*i+1);
        fprintf('the peak height, location, area and standard deviation of no. %f peak
is:\n  %f  %f  %f\n', i,peakloc(i),peakhei(i),peakare(i),peaksig(i));
        end
        fittedx=[1:0.05:w];       %plot the fitted curve on the same graph.
        plot(fittedx,gaussiann(n,c,fittedx),'r-');
        hold off;
 end
```

2-analytes separation analysis on 384-plex *fs*PAGE:

The codes reply on a 2-peak Gaussian function, which is also included here. Note that the parameter order in this 2-peak Gaussian function is slightly different from the n-peak Gaussian function showed above.

```
% define a double gaussian function
%c1 peak height (1st peak)
%c2 migration distance (1st peak)
%c3 standard deviation (2nd moment) (1st peak)
%c4 Background noise (for both peaks)
%c5 peak height (2nd peak)
%c6 migration distance (2nd peak)
%c7 standard deviation (2nd moment) (2nd peak)


function F = gaussian2(c,xdata)
F=c(1)*exp(-(xdata-c(2)).^2/2/(c(3).^2))+c(4)+c(5)*exp(-(xdata-c(6)).^2/2/(c(7).^2));

% The main function for peak fitting in 384-plex fsPAG.
% Input parameters include:
% x: name of the image file.
% y: the background level of in separation
```

```
% interv: the pixel distance between two adjacent wells.
% horio: the distance between the first separation unit and left margin.
% vertu and vertd: the pixel location of the upper and lower boundaries of
%                 first rwo ROI window.

function [dist1,peak1are,peak2are]=multproc384univ(x,y,interv,horio,vertu,vertd)

info = imfinfo(x);   %get information on the width and height of the tif
          w = info.Width;
          h = info.Height;
          datam = imread(x);
          dataunit = ones(vertu-vertd+1, interv-126, 384) ;
for i=1:16
for j=1:24
   dataunittemp=datam((i-1)*interv+vertd:(i-1)*interv+vertu,(j-
1)*interv+horio:j*interv+horio-127);
   dataunit(:,:,(i-1)*24+j)=dataunittemp;
end
end

intensity=ones(384,interv-126);
for k=1:384
   intensity(k,:)=mean(dataunit(:,:,k));        % to average transversely for each data unit
end

plot(1:size(intensity,2),intensity(1,:));       % define the peak width for all peaks
disp('please click on the FWMH points for 1st peak and FWMH points for 2nd peak');
hold on;

[xcoor,ycoor]=ginput(4);       % click on the graph
fitpara7=(xcoor(2)-xcoor(1))/2.355;    % use the clicked value to set up the fitting parameters.
fitpara10=(xcoor(4)-xcoor(3))/2.355;

 hold off;
 c=ones(384,10);

 for i=1:384
   if mod(i,24)==1       % at the start of the each row, click on the two peaks to extract the
peak distance
       disp('start of new row, select peaks');
       plot(1:size(intensity,2),intensity(i,:));
       [kk,km]=ginput(2);
       peakdist1=round(kk(2)-kk(1));
       disp('peak selection done');
   end
```

```
   [zhong1,zhong2]=max(intensity(i,:))        % autoselect the maximum point
   if zhong2<=20
      disp('error in auto selection for max, please select manually');
      plot(1:size(intensity,2),intensity(i,:));
      [z1,z2]=ginput(1);
      zhong1=z2;
      zhong2=z1;
      disp('okay, manual selection done!');
   end
   [yco,xco]=max(intensity(i,zhong2+peakdist1-10:zhong2+peakdist1+10));    % use the peak
distance and the location of maximum peak to locate the other peak
   xco=xco+zhong2+peakdist1-10-1;
   xco=round(xco);yco=round(yco);
   realintensity=intensity(i,(zhong2-20):end);
   q=size(realintensity,2);
   peakdist1=round(xco-zhong2);

   % Fit each each separation unit with the 2peak gaussian distribution
   c=lsqcurvefit(@gaussian2, [zhong1-y 21 fitpara7 y yco-y xco-zhong2+21 fitpara10], 1:1:q,
realintensity);

         peak1loc(i)=c(2);
         peak2loc(i)=c(6);
         peak1hei(i)=c(1);
         peak2hei(i)=c(5);
         peak1are(i)=c(1)*c(3)/0.3989;
         peak2are(i)=c(5)*c(7)/0.3989;
         sr1(i)=(peak2loc(i)-peak1loc(i))/2/(c(3)+c(7));
         dist1(i)=peak2loc(i)-peak1loc(i);
   disp(['Current at:', num2str(i)]);

end
dist1;
peak1are;
peak2are;
end
```

Appendix D: *fs*PAG micro-mold fabrication using Kapton® tape

Micro-molding provides an easy way to fabricate open polyacrylamide gel structure, and it addresses the over-polymerization problem commonly seen with photo-polymerization. Micro-molds were generally manufactured by SU-8 based soft lithography[40], however, this approach is slow and requires clean room equipment and heavy infrastructure. We therefore developed a novel approach for fast and easy micro-mold building. The new method uses laser cutter to create patterns on Kapton® tape and silicon wafer as substrate. This approach is proved to be effective in fabricating meso-scale *fs*PAG structure. The protocol is described here.

Materials: 1 Mil thick Kapton® Tape (Kapton). 8-inch diameter silicon wafer.

Equipment: Full Spectrum laser model HL40-5G-110.

Step 1: Rinse the surface of silicon wafer with methanol, Isopropyl alcohol (IPA) and water 2 times.

Step 2: Carefully attach a layer of Kapton on the surface of the silicon wafer. Note: Use a flat roller to get rid of as much air bubble strapped under Kapton as possible.

Step 3: Place the silicon wafer on the platform in the laser cutter. Tape the wafer to secure its position.

Step 4: Turn on the laser cutter. Import the design file into RetinaEngrave3D. Note: In whatever CAD software, change the linewidth to 0.00025 point, so that the laser track will be recognized as "one line structure" with no width.

Step 5: Set the cutting parameters: Speed=80, Power=0.3, Path=2. Close the lid and start the cutting.

Step 6: After the cut, clean the ashes in the laser track with water rinsed Kimwipe. Note: Carefully hold the silicon wafer in place because a second cut will resume. This ensures second cut will precisely land on the first laser track.

Step 7: After the ash cleaning, perform a second round of cut, followed by ash cleaning. Repeat the "cut-wash" cycle for 3 times. At this point, the Kapton is fully cut through.

Step 8: Take out the silicon wafer. Peal off the Kapton along the laser track. The mold should be ready for use.

If thicker *fs*PAG micro-mold is to be made, multiple layers of Kaptons can be stacked together. However, it is suggested to pattern one layer at a time, that is, to stack multiple micro-mold together instead of cutting through multiple layers. It is difficult to cut through multiple layers at one time.